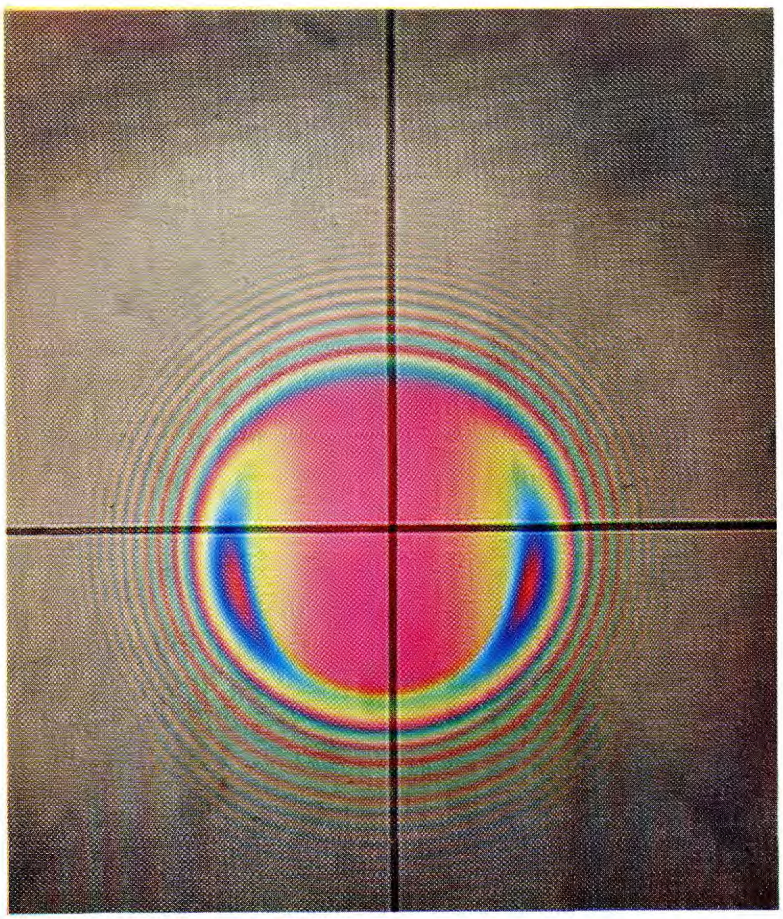


Interference colours at the contact of a lubricated steel ball rolling on a glass plate

# PITTING AND FILM THICKNESS IN ROLLING CONTACT

by

COLIN ARTHUR FOORD

A thesis submitted for the degree of

DOCTOR OF PHILOSOPHY

of the

University of London

and also for the

DIPLOMA OF IMPERIAL COLLEGE

DECEMBER 1967

Applied Mechanics Department

Imperial College

London S.W.7.

## ABSTRACT

The computer solution to a theory of pitting crack propagation which takes into account speed effects and fluid properties is developed, and shows fair agreement with previous experimental work.

The most important section of this work is the development of a technique for measuring the shape and thickness of the three dimensional oil film produced in rolling point contact. The technique uses optical interference to obtain contour maps of the oil film produced when a steel ball rolls against a glass disc which is free to rotate on an air bearing. Excellent fringes are obtained using both monochromatic and white light. Much of the improvement over earlier fringes is due to the use of a partially reflecting chrome layer on the glass disc.

The optical elastohydrodynamic film thickness measurements provide a way of evaluating the relative effectiveness of different lubricant types in producing elastohydrodynamic films. The effectiveness is expresses as a relative pressure viscosity coefficient. Over 40 lubricants including many pure compounds and high performance synthetic lubricants are evaluated. Strong evidence for the non-Newtonian behaviour of polymer blended lubricants, and some evidence for the viscoelastic behaviour of pure compounds is found.

The contour map of the oil film provides an excellent starting point for the theoretical investigation of the elastohydrodynamic problem in point contact. A computer program for calculating the pressure field from the film thickness contour, using Reynolds' equation, is developed. Less success is achieved in the elasticity part of the problem.

Finally, the further possibilities for developing both the experimental and theoretical techniques are discussed.

## ACKNOWLEDGEMENTS

I wish to express my warmest thanks to Dr. A. Cameron (my supervisor) for his good advice and constant willingness to discuss problems. My thanks are also due to Dr. R. L. Johnson of NASA for sending me a selection of 25 exotic lubricants which started the fluid evaluation program, and for introducing my work to the Monsanto Company who arranged for me to take my apparatus to their research centre in St. Louis for three months. I should like to thank the directors of the Monsanto Company and particularly Dr. W. C. Hammann, for arranging this mutually profitable visit, allowing publication of the results obtained during it, and for providing the colour plate. My thanks are also due to Dr. R. Gohar for designing the air bearing, to Dr. H. H. Hopkins for his help with the optics, to A. Dyson and Dr. B. Crossland for supplying samples of oil, the Hoffmann Company for supplying the special balls and finally to Rolls-Royce, Ltd., of Derby for a grant.

CONTENTS


| | | Page No. |
|---|---|---|
| | Abstract | 4 |
| | Acknowledgements | 5 |
| | Contents | 6 |
| | Index to figures | 10 |
| Chapter 1 | Introduction | |
| 1.1 | Introduction | 13 |
| 1.2 | Literature Survey on Pitting | 14 |
| 1.3 | Literature Survey on Film Thickness | 16 |
| 1.4 | General References | 21 |
| 1.5 | Nomenclature | 22 |
| Chapter 2 | Theory of Pitting | |
| 2.1 | Elastohydrodynamic Contacts | 25 |
| 2.2 | Stages of Pitting | 25 |
| 2.3 | Propagation of a Crack | 25 |
| 2.4 | Development of Equations | 26 |
| 2.5 | Solution of Equation | 29 |
| 2.6 | Comparison with Experiment | 31 |
| Chapter 3 | Techniques of Film Thickness Measurement | |
| 3.1 | Introduction | 39 |
| 3.2 | Outline of EHL Theory | 39 |
| 3.3 | Comparison of Experimental Techniques | 40 |
| Chapter 4 | Optical Interference | |
| 4.1 | Introduction | 43 |

CONTENTS (cont.) Page No.


4.2 Conditions for good fringes 43

4.3 Design of Optical System 45

4.4 Achievement of Fringe Contact 47

4.5 Multiple Beam Fringes 48

4.6 Colour Fringes and Calibration 48

4.7 Light Source and Photography 51

4.8 Refractive Index of Oils 52

4.9 An Ideal Light Source 53

Chapter 5 Design of Mechanical Apparatus

5.1 The Successful Apparatus 55

5.2 Earlier Designs 55

5.3 Improvements on the Earlier Design 57

5.4 The Glass Disc 58

5.5 The Loading System 58

5.6 The Drive System and Speed Measurement 59

5.7 Slip Measurement 61

5.8 The Air Bearing 62

Chapter 6 Experimental Measurement

6.1 Method of Evaluating Fluids 64

6.2 Standard Procedure 64

6.3 Tests at Different Loads 67

6.4 Tests Over a Wide Speed Range 68

6.5 Sliding and Friction 68

6.6 Sliding due to Angled Drive 68

6.7 Squeeze Film 69

CONTENTS (Cont.) Page No.

Chapter 7 Experimental Results

7.1 Fluid Comparison 70

7.2 The Effect of Load 70

7.3 The Effect of Wide Speed Range 76

7.4 Sliding and Friction 83

7.5 Film Rupture 84

7.6 Squeeze Film 90

Chapter 8 Interpretation of Fluid Tests

8.1 High Shear Rate High Pressure Viscometry 92

8.2 Comparison of $\alpha_r$ with other estimates of $\alpha$ 93

8.3 Non-Newtonian Behaviour 96

8.4 Estimation of Shear Rate 97

8.5 Viscosity Loss of Fluids Containing Long Chain Molecules 98

8.6 Evidence of Non-Newtonian Behaviour in Pure Fluids 104

8.7 Effect of Fluid Structures on Film Thickness 105

8.8 Possible Effect of Inertia Terms 106

Chapter 9 EHL Theory of Point Contact

9.1 Introduction 107

9.2 Basic Equations 107

9.3 Reynolds' Equation 109

9.4 Finite difference approximation to Reynolds' Equation 111

9.5 Relaxation Solution 115

9.6 The Elasticity Equation 116

9.7 Techniques of Integration 117

9.8 Polar Co-ordinates 121

CONTENTS (Cont.) Page No

Chapter 10 Further Developments

10.1 Evaluation of Lubricants 122

10.2 Design of an Improved Air Bearing 122

10.3 Developments to Theory 125

APPENDICES

1 Solution of the Pressure Distribution Equation 126

2 The Hydrodynamics Program 129

References 138

INDEX TO FIGURES


| Figure | | Page No. |
|---|---|---|
| 1 | Grubin contact with pitting cracks | 27 |
| 2 | Shape of fan crack | 27 |
| 3 | Pressure drops in crack | 30 |
| 4 | Pressure at end of crack Pm vs. A | 32 |
| 5 | Effect of speed on fatigue life | 33 |
| 6 | Effect of transit time on endurance limit | 35 |
| 7 | Effect of viscosity on endurance limit | 37 |
| 8 | Schematic diagram of Crook's capacitance technique for determining film shape | 42 |
| 9 | The optical assembly | 46 |
| 10 | Arrangement of lenses | 46 |
| 11 | Intensities on reflection | 49 |
| 12 | Calibration system | 50 |
| 13 | Calibration check | 54 |
| 14 | The optical elastohydrodynamics rig | 56 |
| 15 | The ball and disc assembly | 56 |
| 16 | Hingley type loader | 57 |
| 17 | Surface finish of balls | 60 |
| 18 | The air bearing | 63 |
| 19 | Colour versus speed for oil No. 5 | 65 |
| 20 | Contours of the elastohydrodynamic contact regions | 71-72 |
| 21 | Oil film profiles at different loads | 73 |
| 22 | Dimensionless film thickness for different fluids | 74 |
| 23 | Dimensionless film thickness at different loads for oil 5 | 77 |
| 24 | Film thickness for a wide range of conditions | 78 |

INDEX TO FIGURES (cont.)


| Figure | | Page No. |
|---|---|---|
| 25 | Rolling contacts lubricated with 5-phenyl-4-ether | 79-80 |
| 26 | Profiles in rolling (cf Fig. 25) | 81 |
| 27 | Sliding contacts lubricated with 5-phenyl-4-ether | 85-86 |
| 28 | Profiles in sliding (cf Fig. 27) | 87 |
| 29 | Friction behaviour of 5-phenyl-4-ether | 88 |
| 30 | Angled drive | 89 |
| 31 | Squeeze film | 89 |
| 32 | Cross section of squeeze film | 89 |
| 33 | Effect of polymethacrylate VI improver | 100 |
| 34 | Effect of thickeners | 102 |
| 35 | Viscosity versus shear rate for a non-Newtonian fluid | 103 |
| 36 | Co-ordinate system | 107 |
| 37 | Computation mesh | 112 |
| 38 | Relaxation molecule | 113 |
| 39 | Geometry of contact zone | 116 |
| 40 | Displacement of a point | 119 |
| 41 | Singularity point | 119 |
| 42 | New air bearing | 124 |
| 43 | Hydrostatic loader | 124 |
| 44 | Solution domain of the crack equation | 126 |
| 45 | Hydrodynamics program listing | 131-134 |
| 46 | Input film shape | 135 |
| 47 | Computed pressure | 136 |
| 48 | Shape and pressure profiles | 139 |

INDEX TO FIGURES (cont.)


| Tables | | Page No. |
|---|---|---|
| 1 | Fluid properties and test results | 75 |
| 2 | Pressure viscosity coefficients $\alpha_e$ estimated by Fresco's method | 95 |
| 3 | High shear viscosity loss of polymer blended fluids | 99 |

# CHAPTER 1 INTRODUCTION

## 1.1 Introduction

The life of highly loaded rolling contact devices such as rolling bearings and gears is often limited, not by the gradual wear of components, but by comparitively sudden collapse of part of the surface. Small pieces of material fall away leaving pits which make the bearing or gears noisy. This leads to further pitting and final break up of the surface.

A common form of failure in the high speed lightly loaded rolling bearings of aircraft gas turbines is skidding of the rolling element, the resultant high sliding velocity causes a temperature rise and scuffing.

In both these cases the thickness and shape of the oil film and the properties of the fluid in the film are likely to be important. The thickness is also of importance in cases where considerable sliding and wear may occur.

A theory of pitting which takes account of fluid properties and may explain earlier experimental results is developed in Chapter 2. More experimental evidence is needed for the theory to be fully assessed, but pitting is a fatigue process and for tests to be valuable they must be run at realistic stresses and speeds which means that pitting times of weeks or even months are involved. The necessary mass-production of test results is therefore more suited to industrial than University research.

In subsequent chapters methods of obtaining a more fundamental look at what happens to the metal and the fluid in the contact are discussed and developed. The first step in any such investigation is to measure the shape and thickness of the oil film in the rolling contact. The formation of these films, and previous techniques of measuring them are discussed in Chapter 3. The technique of measurement used in this thesis is optical interference. The method of achieving good interference fringes and the

design of the optical part of the apparatus are discussed in Chapter 4. To observe good interference fringes they must be stationary, so great care has to be taken to keep the mechanical part of the apparatus free from vibration. The mechanical part of the apparatus, which uses an air bearing, is described in Chapter 5.

The ways of using the apparatus, that has been developed, are described in Chapter 6 and the general results presented and discussed in Chapter 7. The detailed interpretation of tests results on over 40 fluids is a complex subject to which Chapter 8 is devoted. The interference rings are a contour map of the contact region and provide an excellent starting point for the full elastohydrodynamic solution of point contact. An attempt at the full computer solution is begun in Chapter 9 and some progress made. Chapter 10 deals with further developments to the optical elastohydrodynamic technique.

## 1.2 Literature Survey on Pitting

The literature on pitting can be divided into two main groups. One group covers experiments designed to elucidate the mechanism of pitting. The other group which is much larger reports studies of the effect of various parameters such as bearing materials, lubricants etc. on pitting life and stress. It is the first group of papers which is of most interest in the present survey.

In his PhD Thesis (1) Hingley gives an excellent literature survey of both groups of papers. The authors of the I.Mech.E.London publication "Fatigue in Rolling Contact" (1964) also refer to most of the important papers so only those of particular importance are refered to here.

In 1935 Way (2) confirmed that pitting is a form of fatigue failure, and showed that it only occurs when a lubricant is present. He also found that pitting was inhibited by a high viscosity lubricant, and put forward the theory that pits are caused by oil being forced into surface cracks by the high pressure in the contact zone. In 1961 Dawson (3)

repeated the experiments carefully, using a disc machine and found similar results.

A point of particular interest if the theory of Way is to be accepted is whether pitting originates from surface or subsurface cracks. Niemann (4) Cameron (5), Scott (6), and Dawson (3) have reported cracks initiating at the surface, but their observations are not conclusive. It may be that cracks first occur below the surface at the depth of the maximum shear stress and propogate to the surface. Beeching and Nicholls (7) carried out a theoretical analysis of the subsurface stress distribution and concluded that the case hardened layer should extend below the depth of maximum shear stress. The thickness of case they predicted agrees with practice, but it may be that yielding of the core causes stress changes in the surface. In the authors closure Beeching (7) refers to Way (no reference given) having found subsurface cracks which would lead to pits in parts of a pitted roller where no surface damage was present. Way (2) however refers to subsurface cracks found by Ullricht (8) and concludes that they would not lead to the characteristic pitting failure.

In the communications of (7) Cameron suggested that the extra stresses imposed by deformation of the surface roughnesses will occur nearer the surface and may be responsible for surface cracking. Dawson (9) in 1961 concluded from his experiments that asperity contact is a necessary condition for pitting. The achievement of their elastohydrodynamic solution in line contact enabled Dowson, Higginson and Whitaker (10) to predict the stress distributions in lubricated contacts. A particularly interesting point is that under high speed low load conditions the plane of maximum shear stress is near the surface; but as they point out in (11) , at high loads and low speeds the distribution is almost Hertzian and pitting still occurs.

Crook (12) and later Hamilton (13) showed experimentally that cumulative plastic shearing can take place in the subsurface layers.

Merwin and Johnson (14) and Johnson and Jefferis (15) investigate this shearing theoretically and showed the possibility of shakedown to a situation in which the residual stresses enable subsequent stress cycles to be entirely elastic.

Lubricant properties have also received extensive study. Most workers find that bulk viscosity plays an important role. Moore and Lewis (16) and Martin and Cameron (17) found no relation between pressure-viscosity coefficient and life, but other workers including Cordriano, Cochrane and Wolfe (18), Carter (19) and Scott whose latest paper is (20) think that pressure-viscosity may be important.

The affect of speed on pitting has received comparitively little attention, but Dawson (9) has found that pitting life increases with oil film thickness and therefore with speed and viscosity. Hashimoto (21) using a gear machine and Hingley (1) with his point contact device have also observed an increase in pitting life with increased speed.

1.3 Literature Survey on Film Thickness

Many of the references on pitting suggest that film thickness, and parameters such as speed and viscosity which affect film thickness, are important factors in the pitting failure of rolling elements. In their book (11) Dowson and Higginson give an excellent introduction and bibliography up to 1964 so only recent papers, and earlier ones of the most permanent interest, will be discussed here.

Theoretical solutions, which assumed either constant viscosity or rigid surfaces, failed to predict sugnificant oil films. Grubin (22) in 1949 was the first to allow for both pressure dependant viscosity and elastic distortion. His approximate solution predicted film thicknesses which were orders of magnitude higher than those of previous solutions. An excellent account of his work is given by Cameron (72). The next major theoretical step was the accurate computer solution of the elastohydrodynamic

problem for line contacts under isothermal conditions by Dowson and Higginson (23) in 1959. Since this time many papers which extend the theory in various ways have been published.

Dowson and Higginson extended the range of solutions and showed the now famous outlet pressure spike (24). They also published a formula which gives the minimum film thickness in a rolling bearing (25), and together with Whitaker they studied the effect of compressibility (26) and the subsurface stress system (10). In 1964 they applied their theory to involute gear lubrication (27). Dowson and Whitaker (28) published a paper on the types of isothermal roller lubrication and discussed the methods of EHL solution; This has been followed by their paper on the solution of sliding contacts (29) in which the isothermal assumption no longer holds.

Other theoretical studies of note are those of G.D.Archard, Gair and Hirst (30) who in 1961 achieved numerical solutions which did not require operator intervention during the computing cycle. Their results were limited to relatively high low speed conditions in which the parallel portion of the film allows the inlet and outlet regions to be treated separately. Cheng and Sternlicht (31) achieved the full solution for sliding contacts allowing for heat conduction to solids and found that the pressure spike persisted under these conditions. Cheng and Orcutt(32) compared theoretical solutions with experimental results, in particular they were able to accelerate convergence by assuming the position of the outlet pressure spike.

The two most notable solutions in point contact are those of Gohar and Cameron (33) who applied Reynolds equation in polars to the Grubin shape, and Archard and Cowking (34) who used the Grubin shape and line contact theory with a side leakage factor. If carried out with a computer Gohar and Cameron's method might well be better, but the use of hand relaxation limited them to a coarse mesh and a small contact zone.

The first convincing experimental measurements are those of Crook (35)

using various capacitance techniques and a disc machine. The techniques were inter-disc capacitance which requires a knowledge of the oil dielectric constant at high pressure, and a pad technique in which capacitance pads are used to measure the oil flow through the contact and thus the thickness. He extended this work (36) by systematically studying the reduction between film thickness viscosity and speed, and in (37) and (38) he went on to discuss theoretical and experimental work on friction and temperature. Crook (39) used an elegant technique to measure the shape of the EHL gap. This is refered to in Chapter 3 of this thesis. (40) is a useful review paper. Dyson, Naylor and Wilson (41) and (42) have refined the inter-disc capacitance technique and produced impressive results that agree closely with theory for a number of fluids, the only deviations being in the case of fluids known to be non Newtonian.

The most common alternative to capacitance methods is X-ray transmission, this technique was published by Sibley and Orcutt (43) and has been used since (44). Measurements show fair agreement with theory.

Measurements of oil film thickness in sliding point contact have been made by Archard and Kirk using their crossed cylinders machine. They have investigated a wide range of speeds, loads and Young's modulii (45,46) and have tested a few different fluids (47). The first use of optical interference to measure film thickness was reported by Kirk (48) and Archard and Kirk (46), but they used perspex cylinders which prevented the study of typical EHL conditions and resulted in poor fringes. Gohar and Cameron (49) and later (33) rolled a steel ball against a stationary plate of high refractive index glass and obtained fair fringes under EHL conditions, they investigated a number of very thick fluids at various speeds and found some interesting results. In 1966 they presented a paper (50) in which they loaded their ball against a diamond which enabled them to run at

high stresses. They also investigated the blend at the edges of rollers. The first optical measurements in rolling point contact, use an improved optical technique, and are the subject of this thesis and of (51).

Measured film shapes have been used to predict pressure distributions within the contact. Cheng and Orcutt (32) use Crook's variable capacitance glass disc technique, and Kannel, Bell and Allen (44) use X-ray transmission. The X-ray technique has a serious and insurmountable disadvantage, in that the results are a shadow graph and will therefore represent the profile at the edge of the contact which is unlike that which pertains over 95% of the width. Direct pressure measurements have been made by Niemann and Gartner (52) who have a hole in the contact zone which communicates with a pressure transducer, and by Kannel (53) and later Kannel, Walowit, Bell and Allen (54) who use a manganim strip that changes in resistance as it passes through the contact. In both these methods the transducer is too large and its pressure range restricted but the manganim strip shows great promise and has a faster response. Temperatures have been measured using a similar technique but with a platinum (32) or titanium strip (54).

Any work on elastohydrodynamic film thickness requires a knowledge of the physical properties of the lubricant. Such properties as viscosity and density at atmospheric pressure are easily measured, but the change of these properties as pressure increases usually has to be estimated from previous work. In 1953 the American Society of Mechanical Engineers published a report on viscosities and densities at high pressures and temperatures (55). Chu and Cameron published two useful papers (56,57) which fitted empirical laws to the ASME results. Roelands (58) fitted a complex equation to pressure and temperature viscosity results and derived a prediction method for petroleum fractions. Fresco (59) measured the pressure viscosities of a wide range of modern lubricants and achieved

a method for predicting pressure-viscosity coefficients based on the temperature-viscosity behaviour. Galvin, Naylor and Wilson (60) measured high pressure properties including dielectric constant at different temperatures.

A number of workers have found that film thicknesses measured with certain fluids, particularly silicones and polymer thickened oils give a much thinner film than theory and comparison with other fluids would suggest. This effect was found by Archard and Kirk (47) and outstandingly demonstrated by Dyson, Naylor and Wilson (42). It is due to non-Newtonian behaviour in which the fluid undergoes an elastic component of deformation in addition to its viscous component. Dyson et al (42) predict the behaviour of fluid in continuous shear from the measurements of Barlow and Lamb (61) in oscillatory shear, and develop an approximate theory of film thickness which gives fair agreement with their measurements.

The full relation between the stress and strain tensors is very complex as shown by Oldroyd (62) and for practical solutions a simplified model must be assumed. Milne (63) and Burton (64) have used the simplest Maxwell model which as shown by Tanner (65,66) is inadequate. Due to its simplicity the straightforward Maxwell model has been used since (32), but Dyson (67) in a comprehensive paper shows the importance of using better models of viscoelastic behaviour. He also derives a relation between the properties of fluids in continuous shear, which are required but not easily measureable, and those in oscillatory shear which have been measured by Barlow and Lamb (61).

The fact that polymer thickness or VI improvers lose much of their effect at fairly modest shears is discussed by Philipoff (68). Horowitz and Steidler (69) calculated the performance of journal bearings lubricated with such fluids and recently Hamilton and Robertson (70) have investigated

the elastohydrodynamic lubrication of rollers. The present author (51) suspects on experimental grounds, and Chow and Saibel (71) on theoretical grounds that viscoelastic effects may be significant in straight lubricants.

1.4 General References

Some very good books on lubrication have been published recently, those which the author found most useful are "Elasto-hydrodynamic Lubrication" by Dowson and Higginson (11) which is an excellent text on EHL work up to 1964 and "Principles of Lubrication" by A. Cameron (72) which is a clear and comprehensive book covering a wide range of topics. "Theory and Research in Lubrication" by Hersey is less valuable in content but has by far the largest bibliography of any book. "Physical Chemistry of Lubrication Oils" by Bondi (73), although published in 1951 and now out of print is a very valuable text on this subject.

A few lubrication references which are mentioned in the text of this thesis but not included in the surveys and a number of references on other disciplines, are included at the end of the numerical list.

## 1.5 Nomenclature

The principal symbols are:

$a$ = Slope of log film thickness vs log speed line, (index of speed parameter), and also the Hertz contact radius

$b$ = Index of load parameter

$c$ = Index of materials parameter, or compressibility

$E_1$ & $E_2$ = Young's modulus of bodies 1 and 2

$E'$ = Reduced Young's modulus defined as: $\frac{1}{E'} = \frac{1}{2}\left(\frac{1-\sigma_1^2}{E_1} + \frac{1-\sigma_2^2}{E_2}\right)$

$h$ = Film thickness at any point, or crack thickness

$h_o$ = Film thickness at centre of contact, or crack thickness at tip

$I$ = Intensity of light, or finite difference co-ordinate in X or R direction

$J$ = Finite difference co-ordinate in Y or $\Theta$ direction

$K$ = Finite difference co-ordinate in time direction

$L$ = Length of line contact, or length of pitting crack

$n$ = Refractive index

$p$ = Pressure

$p_o$ = Maximum Hertz pressure

$p_m$ = Maximum pressure at tip of crack

$q$ = Oil flow in crack

$r$ = Polar co-ordinate

$R$ = Reduced radius* defined as $\frac{1}{R} = \frac{1}{R_1} + \frac{1}{R_2}$, or polar co-ordinate

$s$ = Displacement

$S$ = Temporary viscosity loss of a non-Newtonian fluid

$t$ = Time

$u_1$ & $u_2$ = Surface speeds of bodies 1 and 2

* Written as R' in Chapter 9 to avoid confusion

$U$ = Rolling speed = $(u_1 + u_2)$

$w$ = Elastic deformation in z direction

$W$ = Total load

$x$ = Co-ordinate in rolling direction

$y$ = Co-ordinate normal to rolling direction

$z$ = Co-ordinate in thickness direction

$x', y', r', \theta'$ = Co-ordinates of pressure field

$\alpha$ = Pressure-viscosity coefficient in $\mu = \mu_o e^{\alpha p}$

$\alpha_e$ = Pressure-viscosity coefficient estimated by Fresco's method (59)

$\alpha_r$ = Relative pressure-viscosity coefficient determined in these tests

$\gamma$ = Displacement

$\Gamma$ = Shear rate

$\lambda$ = Wavelength of monochromatic light

$\theta$ = Angle or polar co-ordinate

$\mu$ = Viscosity

$\mu_e$ = Effective viscosity of a non-Newtonian fluid

$\mu_o$ = Viscosity of fluid at atmospheric pressure and test temperature

$\rho$ = Density of oil

$\sigma$ = Poisson's ratio

$\tau$ = Shear stress or Transit time

$\psi$ = Temporary loss of viscosity improvement in a polymer-blended lubricant

$\omega$ = Over-relaxation parameter

Dimensionless Parameters:

$A$ = Pitting parameter $\frac{1}{12}\left(\frac{\tau}{\mu c}\right)\left(H_o\right)^2$

$B$ = $(c - \alpha)p_o$, or relaxation coefficient

$C$ = Compressibility $(cp_o)$, or relaxation coefficient for Reynold's equation

$D$ = Pressure viscosity parameter $(\alpha p_o)$, or relaxation coefficient for Reynold's equation

$E$ = Young's modulus, or relaxation coefficient for Reynold's equation

$G$ = Displacement $\frac{\gamma}{a}$

$H$ = Film thickness $\frac{h}{a}$ or crack thickness $\frac{h}{L}$

$P$ = Pressure $\frac{p}{p_o}$

$P_m$ = $\frac{p_m}{p_o}$

$p^*$ = Reduced pressure $p^* = e^{-\alpha p}$

$R$ = Polar co-ordinate $\frac{r}{a}$ or $\frac{r}{L}$, or reduced radius

$T$ = Time $\frac{t}{\tau}$

$X, Y, X'$ and $Y'$ = Co-ordinates $\frac{x}{a}$, $\frac{y}{a}$, $\frac{x'}{a}$, $\frac{y'}{a}$

$(h/R)$ = Film thickness parameter

$(H_o/R)_4$ = $(h_o/R)$ at $(U\mu_o/E'R) = 4 \times 10^{-11}$

$(U\mu_o/E'R)$ = Speed parameter

$(W/E'R^2)$ = Point contact load parameter

$(\alpha E')$ = Materials parameter

# CHAPTER 2 THEORY OF PITTING

## 2.1 Elastohydrodynamic Contacts

The high pressure developed in a highly loaded contact causes the surfaces to deform and the viscosity of the oil to increase sufficiently for an oil film to be formed. The formation and thickness of these oil films is discussed in greater detail in Chapter 9.

For the purpose of the pitting theory it is assumed that surface deformations and pressures are those of the Hertzian dry contact case, but with an oil film present between the surfaces as shown in Fig. 1. This is the Grubin (22) assumption. $\tau$ is the time taken for an element of surface to pass through the Hertzian zone, and is known as the transit time.

## 2.2 Stages of Pitting

Pitting only occurs in the presence of a lubricant (2,3) and in three stages. The first stage is the initiation of a crack which is presumed to be a fatigue process caused by the cyclic variation of the orthogonal shear stress, the second stage is the propagation of this crack and finally the crack is of such an extent that a piece of metal falls away leaving a pit.

## 2.3 Propagation of a Crack

If the propagation of the crack is caused merely by the stress system within the material, pitting would occur in the absence of lubricant, but this does not occur, so the fluid must play some part in propagation. In 1935 Way suggested that a crack which is filled with oil (presumably by capillary action) and suitably orientated will be extended by the compressive load and rolling action.

The orientation of the crack in the lower member in Fig. 1, is such that its mouth leads into the contact and is held open by the oil pressure.

As the crack passes through the contact oil is forced down the crack, thus extending it. If the crack is orientated as the one in the upper member in Fig. 1 the oil tends to be rolled out and no extension occurs.

Hingley (1) suggested that the oil which is compressible must flow down the crack in order to transmit a pressure to the end of the crack where the extension takes place. This flow of a viscous fluid must be caused by a pressure drop in the crack. There is presumably a critical pressure near the end of the crack which is required for the crack to propagate, hence the near Hertzian pressure at the mouth of the crack must be equal to this propagation pressure plus the pressure drop.

Hingley (1) developed a simplified equation for the pressure attenuation in the isoviscous case which showed the importance of the parameter $(\tau/\mu c)$ and could be solved graphically for a restricted range of conditions. He also did some experimental work to investigate the effect of this parameter.

## 2.4 Development of Equations

Observations of pitting cracks as for example in (5) show that they radiate out in a fan from their origin. The following analysis is to find the pressure drop, due to the flow of fluid down such a crack; the crack being assumed to have rigid walls. This is an important factor.

Consider a fan of constant angle $\theta$ and of height $h = h(r)$, Fig. 2.

### Force Equilibrium

Assuming all the flow is radial the equilibrium equation is

$$\frac{\partial \tau}{\partial z} = \frac{\partial p}{\partial r}$$

which using the Newtonian viscosity law can be integrated to give the radial flow

$$q_r = -\frac{h^3 r\theta}{12\mu} \frac{\partial p}{\partial r}$$

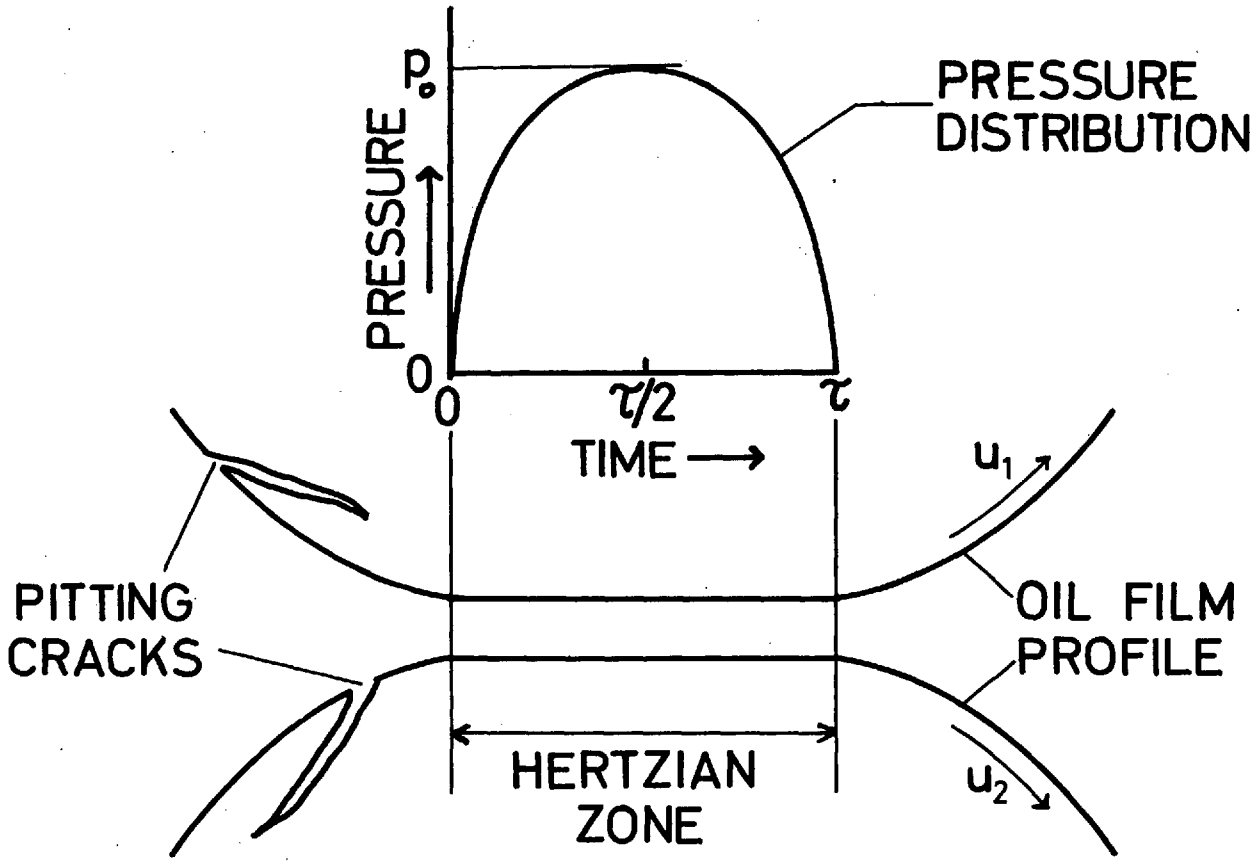



Fig. 1 Grubin contact with pitting cracks

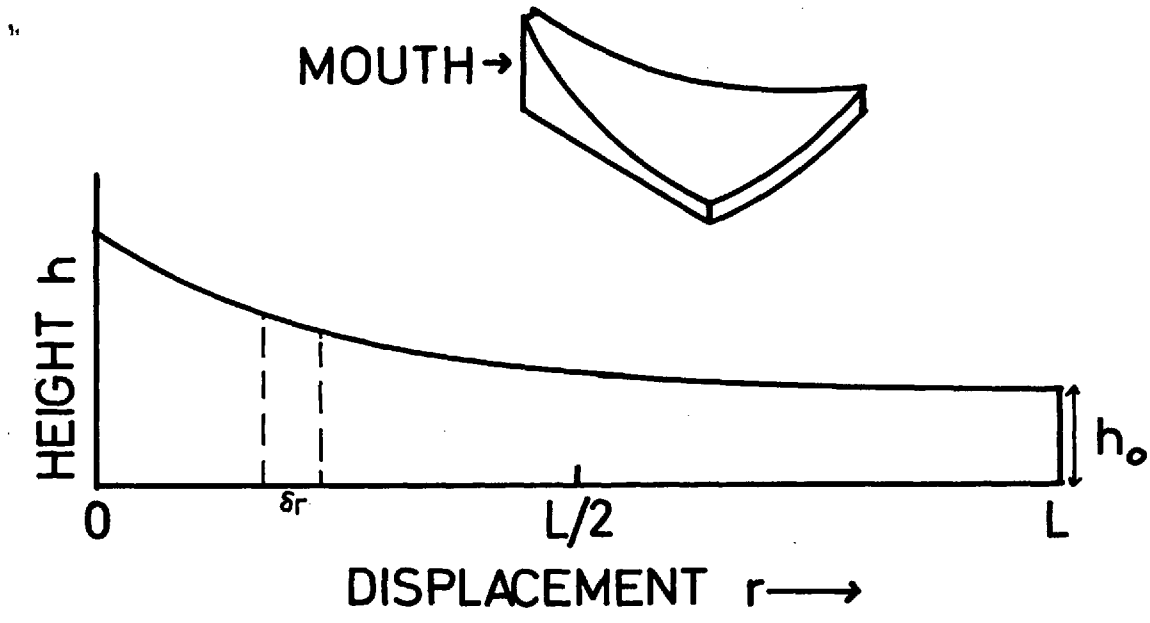



Fig. 2 Shape of fan crack

Continuity of Mass Flow

Consider a control volume of length $\delta r$ which extends across a typical section of the crack and contains a mass $m_c$ at an instant. For mass continuity

$$\left[\begin{array}{c}\text{rate of}\\ \text{decrease of } m_c\end{array}\right] = \left[\begin{array}{c}\text{net outflow from}\\ \text{control volume}\end{array}\right]$$

$$\therefore -\frac{\partial}{\partial t}(m_c) = \frac{\partial}{\partial r}(\rho q_r)\,\delta r$$

$$\therefore \frac{\partial}{\partial t}\left(\rho h r\theta\ \delta r\right) = \frac{\partial}{\partial r}\left(\frac{\rho h^3 r\theta}{12\mu}\ \frac{\partial p}{\partial r}\right)\delta r$$

which on differentation gives

$$\frac{\partial p}{\partial t} = \frac{h^2}{12\mu}\left\{\frac{\partial^2 p}{\partial r^2} + (c - \alpha)\left(\frac{\partial p}{\partial r}\right)^2 + \left(\frac{1}{r} + \frac{3}{h}\frac{\partial h}{\partial r}\right)\frac{\partial p}{\partial r}\right\} \quad \ldots\ldots\ldots\ldots 1$$

where $c = \frac{1}{\rho}\frac{\partial \rho}{\partial p}$, the compressibility

and $\alpha = \frac{1}{\mu}\frac{\partial \mu}{\partial p}$, the pressure viscosity coefficient in $\mu = \mu_o e^{\alpha p}$

Equation 1 can be simplified if

$$\frac{1}{r} + \frac{3}{h}\frac{dh}{dr} = 0$$

i.e. $rh^3$ = constant.

This is a realistic crack shape, comparing well with that found by Cameron (5).

The pressure distribution under the contact at any instant is assumed to be Hertzian, which is a good approximation for high loads, hence the

pressure-time relation at the mouth of the crack as the ball rolls over it is:

$$\frac{p_1}{p_o} = 1 - \left( 2\frac{t}{\tau} - 1 \right)^2 \qquad \text{.....2}$$

where $p_1$ = the mouth pressure

$p_o$ = the peak Hertz pressure

and $\tau$ = the transit time.

The transit time is the time taken for the Hertzian flat to cross the contact (Fig.1). This is a speed parameter which depends on linear velocity through the contact as distinct from the rate of repetition of pressure cycles. It should also be noted that transit time increases with load.

Using $p_o$ and $\tau$, the quantities in equation (1) can be made dimensionless as follows:

$$P = \frac{p}{p_o}, \quad T = \frac{t}{\tau}, \quad R = \frac{r}{L}, \quad H = \frac{h}{L},$$

and the equation written

$$\frac{\partial P}{\partial T} = AR^{-\frac{2}{3}} \exp(-DP)\left\{ \frac{\partial^2 P}{\partial R^2} + B\left( \frac{\partial P}{\partial R} \right)^2 \right\} \qquad \text{.....3}$$

where $A = \frac{1}{12}\left(\frac{\tau}{\mu c}\right)(H_o)^2$

$D = \alpha p_o$ and $B = (c - \alpha)\, p_o$

also $C = cp_o$ $\therefore$ $C = B + D$.

## 2.5 Solution of Equation

The equation is a non-linear second order parabolic differential equation, and must be solved by numerical techniques using a computer, (Appendix. 1). The parameter A cannot be determined because $H_o$ the crack

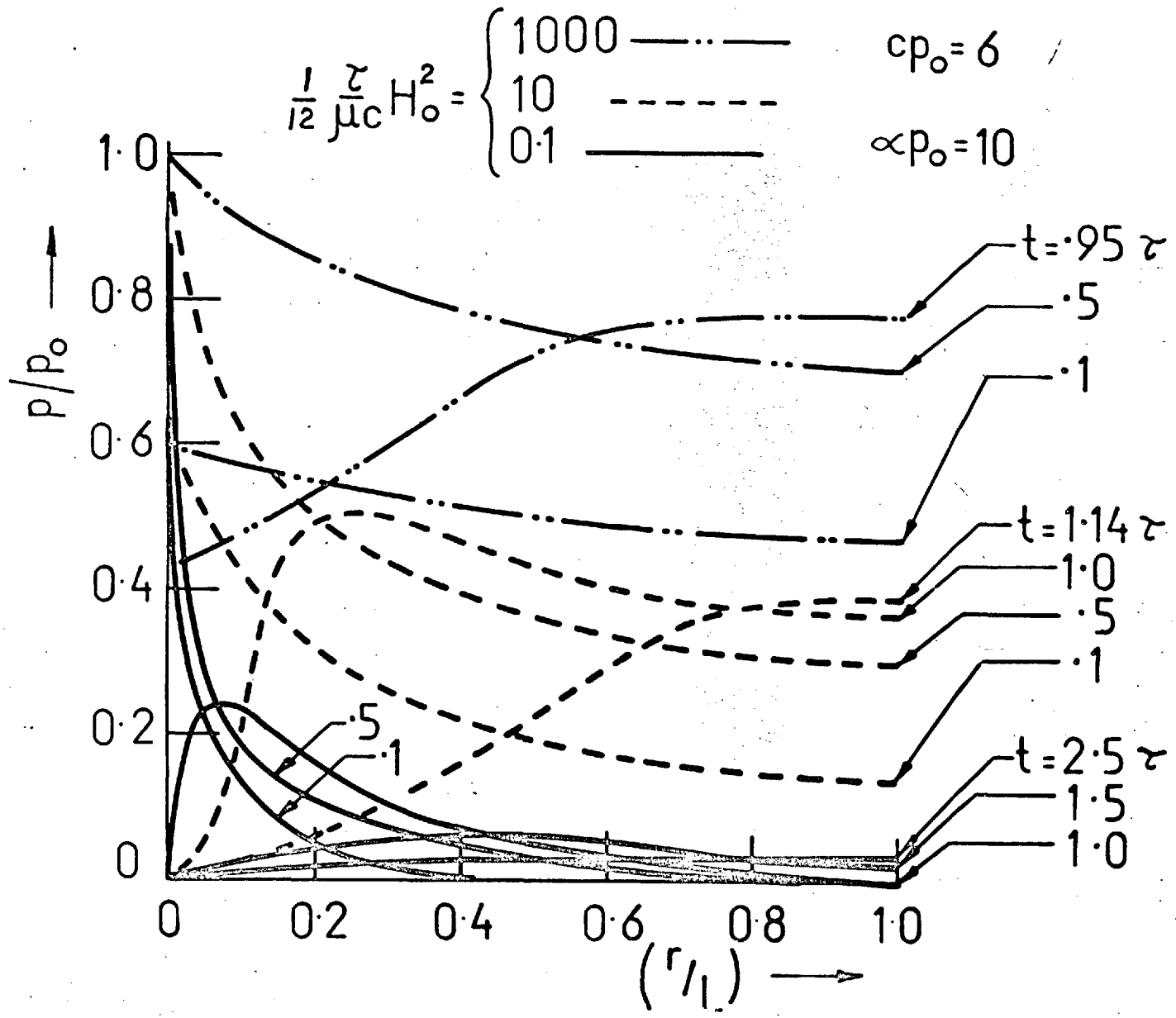



Fig 3 Pressure drops in crack

geometry parameter is not known. Solutions have been obtained however, for a wide range of values of A so that the qualitative behaviour can be studied. Pressure distributions along the crack at different transit times and for different values of A are shown in Fig. 3. It can be seen that at high values of A the pressure is propagated much more quickly as well as higher values of the pressure at the end of the crack being reached.

Although not necessarily the condition imposing the most severe stress distribution at the end of the crack, the maximum pressure reached $P_m$ is indicative of the general pressure distribution in each case, so this pressure is plotted against A for various values of $cp_o$ and $\alpha p_o$, Fig. 4. It is possible to work back from the experimental results and estimate a value for $H_o$. Results for a wide range of the parameters A, D and C are shown in Fig. 4.

2.6 Comparison with Experiment

It can be seen from Fig. 4 that for low transit times (ie. high linear speeds through the contact and low loads) and high viscosities, $P_m$ is decreased and in consequence the pitting life is increased. The viscosity effect is well known in practice and was investigated by Martin and Cameron (17); the speed effect is often obscured because in most applications increased speeds result in increased running temperatures (ie. reduced viscosities) and increased loads, but Hingley's tests Fig. 5, in which increasing the rolling radius increases the linear speed while keeping the cycling rate constant, demonstrate the effect convincingly. $P_m$ also decreases with increasing compressibility, this is as one would expect because with a more compressible liquid more flow can take place before pressure builds up. To our knowledge, however, no satisfactory testing has been carried out to investigate the effect of compressibility,

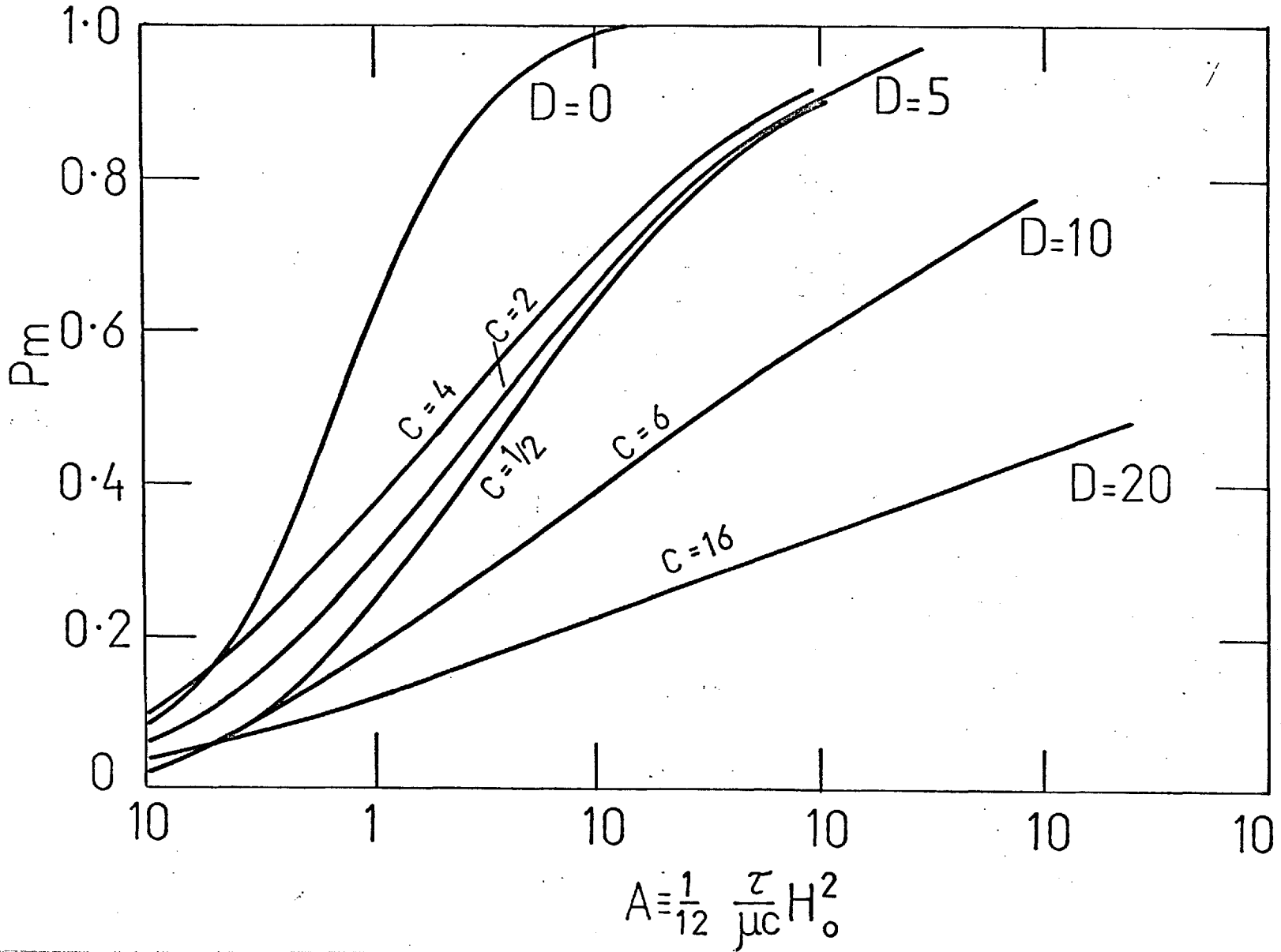



Fig 4 Pressure at end of crack Pm vs. A

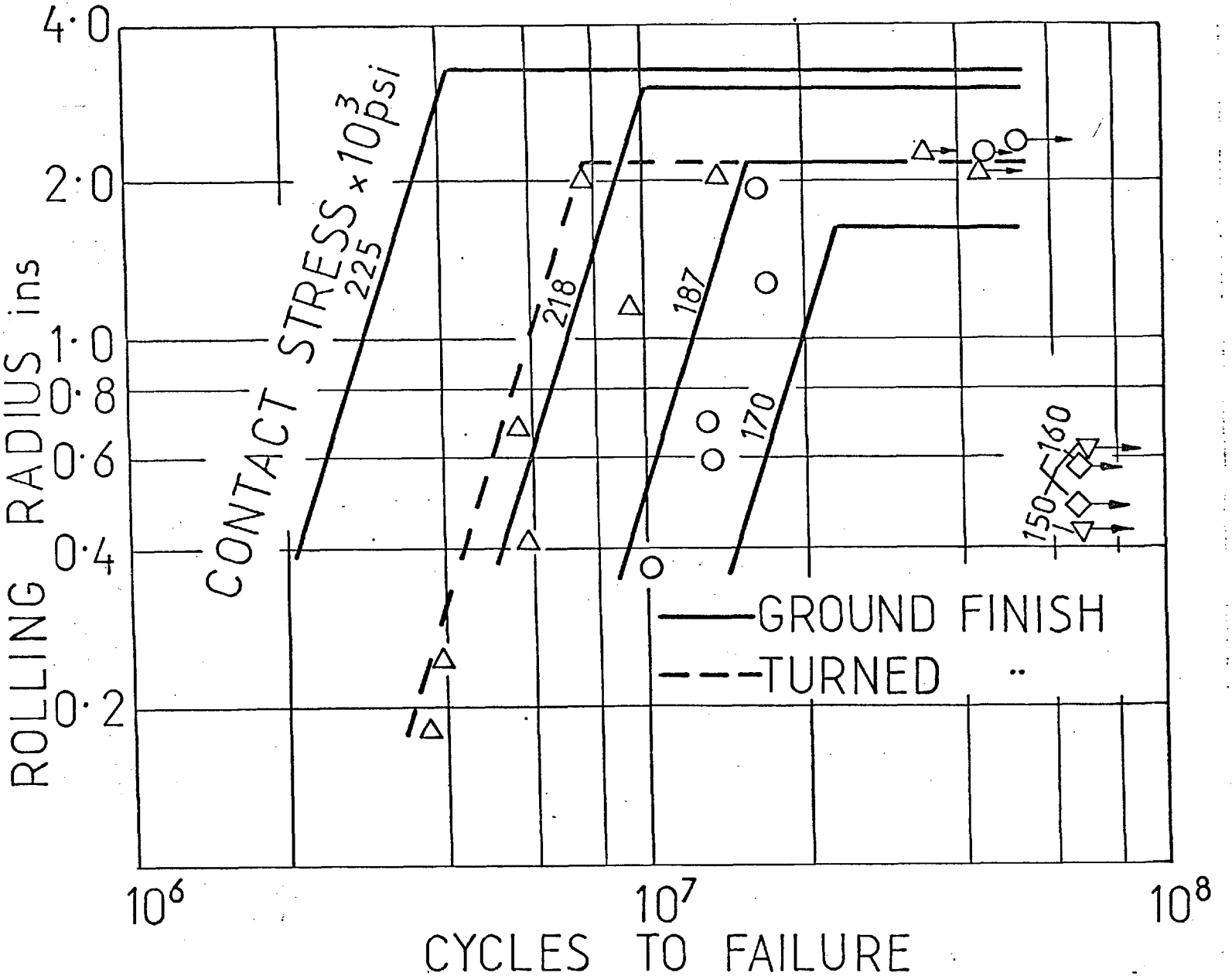



Fig 5 Effect of speed on fatigue life

This is as one would expect because with a more compressible liquid more flow can take place before pressure builds up. To our knowledge, however, no satisfactory testing has been carried out to investigate the effect of compressibility, which is not surprising as the compressibility of most fluids is of the same order.

The pressure viscosity effect also needs experimental investigation. The theoretical result is as would be expected, a higher value of $\alpha p_o$ produces a higher effective viscosity in the crack and therefore a lower pressure. Existing tests have been carried out at values of 'A' too large for pressure attenuation to take place.

The effect of compressibility, as it occurs in the term $(c - \alpha)p_o$, can be explained as follows; if the liquid were either incompressible ($c = 0$) or infinitely viscous, no flow could take place and consequently pressure could not be reduced by the proposed method. In fact values of $c/\alpha$ are found below which no suitable solution can be obtained for the pressure distribution equation; this minimum value of $c/\alpha$ is 0.6 in the D = 20 case, whereas typical values for c and $\alpha$ give $c/\alpha = 0.1$. The analysis assumes a rigid crack but when pressure of the order 100,000 p.s.i. are applied, the crack must expand, which has the same effect as an increase in compressibility. Cases have been worked out for various values of $cp_o$ and as can be seen from Fig.4 the effect of this parameter is relatively small.

Fig. 6 shows that in the experiments of Hingley no decrease in pitting stress occurs with transit times greater than 25 microseconds. This suggests that at this value the full pressure just reaches the end of the crack, and provides a means of estimating $(h_o/L)$ as follows:

$$\text{for Diesel fuel} \quad \alpha = 0.6 \times 10^{-4} \quad (\text{p.s.i.})^{-1}$$

from Wooster's relation (56)

$$\alpha = \text{centipoise}$$

$$c = 4 \times 10^{-6} \quad (\text{p.s.i.})^{-1}$$

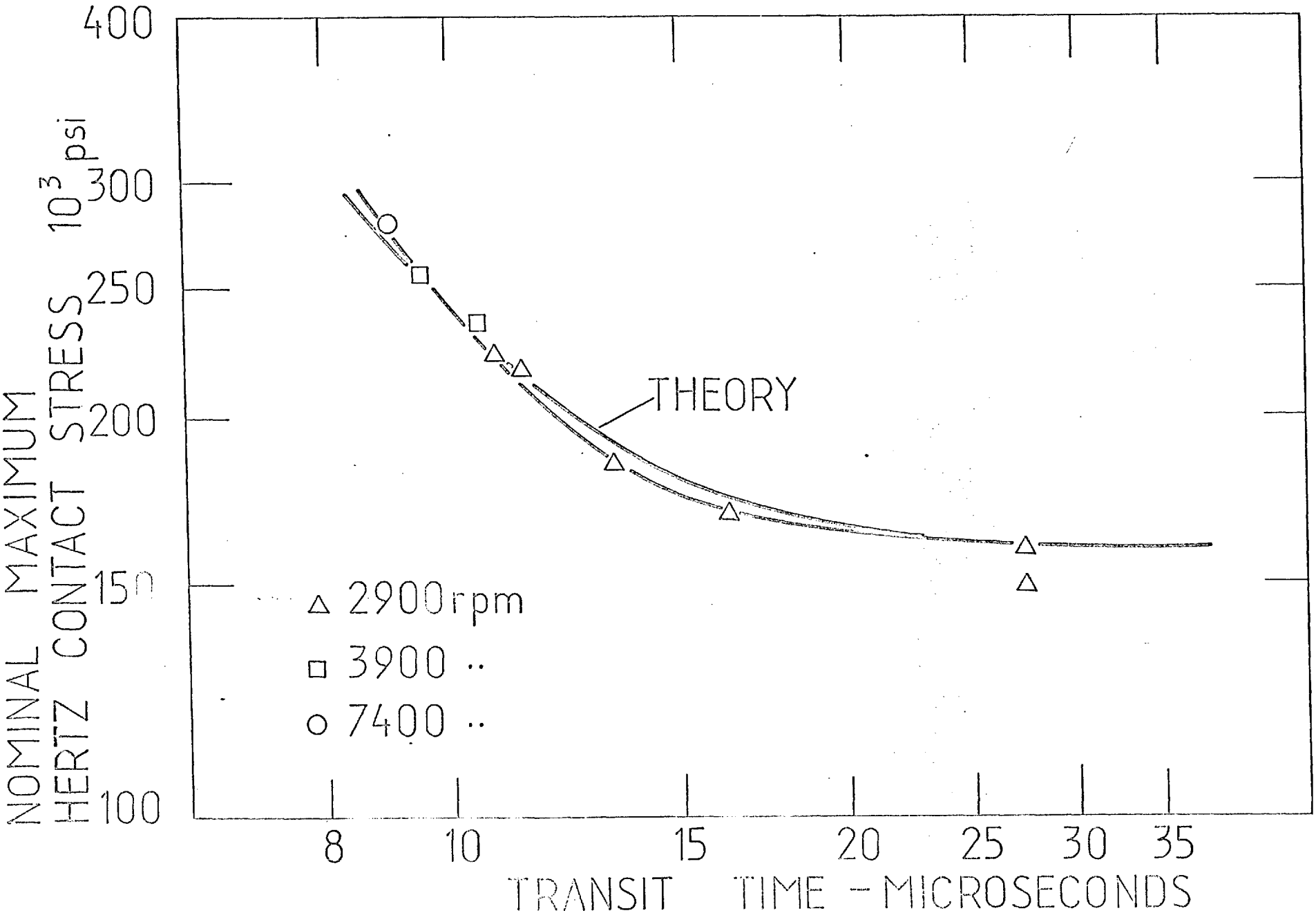



Fig 6 Effect of transit time on endurance limit

from the tests

minimum pitting stress, $p_o$ = 160,000 (p.s.i.)

limiting transit time $\tau$ = $25 \times 10^{-6}$ sec

$$\therefore \quad D = \alpha p_o = 6 \times 1.6 = 10$$

From Fig. 4 the curve for D = 10 shows that the full pressure will reach the end of the crack at $A = 10^4$.

$$A = \frac{1}{12}\left(\frac{\tau}{\mu c}\right)\left(\frac{h_o}{L}\right)^2$$

$$\therefore \quad \frac{h_o}{L} = 0.1$$

This implies a stubby crack as plotted in Fig.2.

The theory cannot be used to predict the quantitative behaviour, but it is possible to see how well it fits the experimental data. The theoretical curve in Fig. 6 was obtained as follows. At $\tau$ = 25 microseconds the pressure at the end of the crack is assumed to equal the maximum Hertz pressure of 160,000 p.s.i. (Fig. 6); from the theory $P_m = 1.0$ (i.e. no attenuation), D = 10 and from Fig.4, $D = 10^4$. At, say, $\tau$ = 12.5 microseconds 'A' will be $5 \times 10^3$, D is not known but can be put equal to the $\alpha p_o$ experimental which is 12 and $p_m$ can be interpolated from Fig. 4. The value of $p_m$ found in this way is .81, and as the pressure at the end of the crack is still the propagation pressure 160,000 p.s.i.

$$p_o = \frac{160,000}{p_m} = 197,000 \text{ p.s.i.}$$

The theoretical curve in Fig. 7 is evaluated in a similar way, the compressibility was assumed to be the same for all oils but the pressure viscosity coefficient was evaluated for each oil. In this case $H_o$ was found to be $2.5 \times 10^{-2}$.

In (17) the effect of oil viscosity was investigated with line contact using the same steels. At the lowest viscosity the limiting stress is

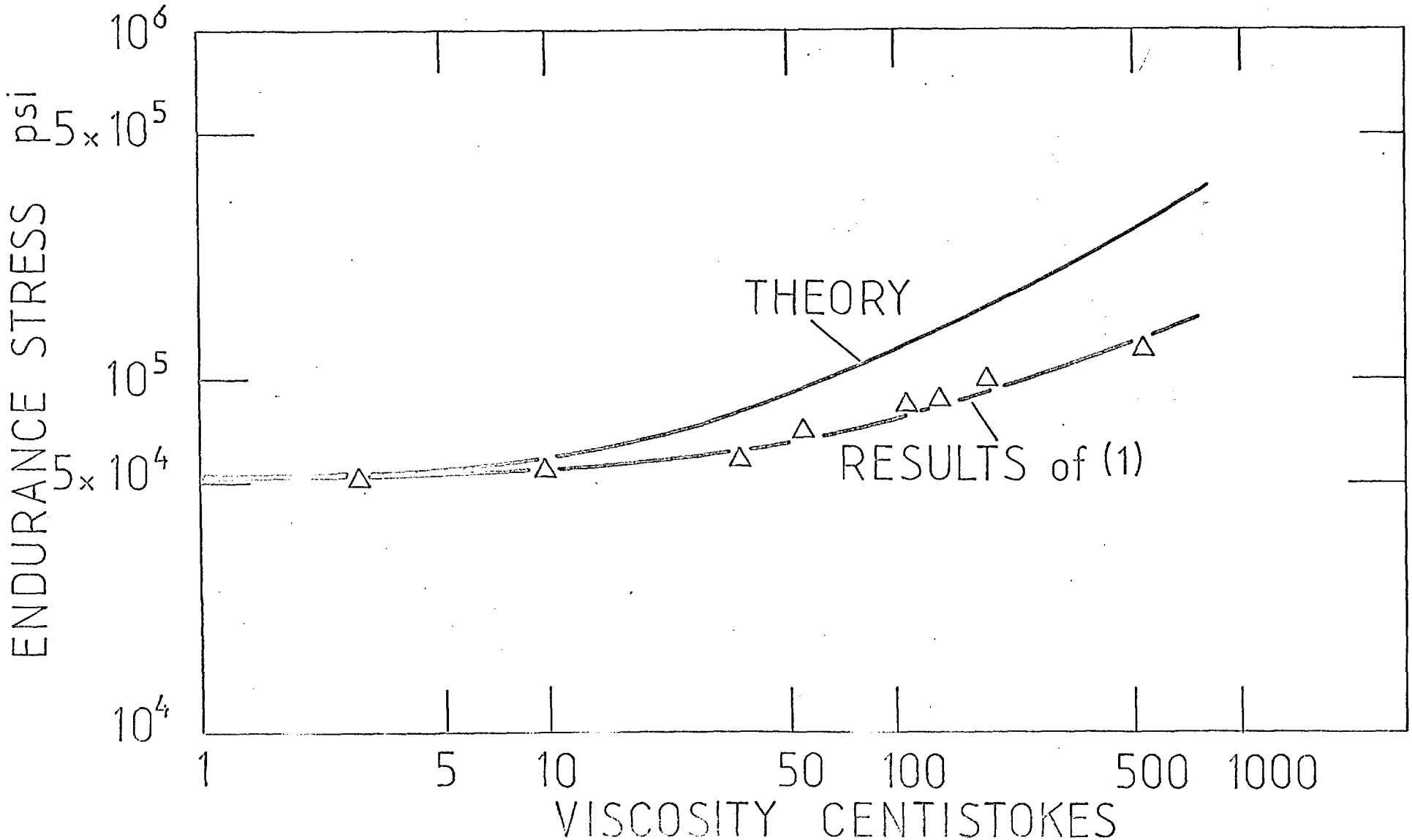



Fig 7 Effect of viscosity on endurance limit

52,000 p.s.i. (Fig 7) whereas in these tests using the same low viscosity fluid the limiting stress at the longest transit time was 160,000 p.s.i., some three times larger. The grooving of the track in the point contact case makes the actual maximum stress near 100,000 p.s.i. but even this is twice as big as the line contact case. A point contact therefore allows a far larger nominal maximum Hertzian stress to be carried than does a line. Niemann (75) has also reported this interesting finding. No explanation can be offered to account for it at present but it is thought that the oil film may distribute the load more effectively in point contact than in line contact. The rest of this thesis is devoted to work on measuring the shape of the oil film and the effect of various parameters on this shape. The measurement of shape is a first step in determining the pressure and stress distributions.

# CHAPTER 3 TECHNIQUES OF FILM THICKNESS MEASUREMENT

## 3.1 Introduction

An oil film between rolling contacts which is thick compared with the surface asperities would limit the wear due to asperity contact and might also reduce the severity of the stress distribution by spreading the load over a greater area. For these reasons a great deal of theoretical and experimental effort has been directed to predicting and measuring such films.

In 1916 Martin solved Reynolds' hydrodynamic equation for the case of rigid cylinders and an isoviscous fluid, and predicted a minimum oil film thickness of about 1 micro inch. Since this is less than the surface roughness, it was concluded that the only functions of the lubricant are to wash away the wear debris, cool the surfaces and perhaps form a chemically bonded film to prevent welding of the asperities. Subsequent workers considered elastic cylinders and fluids with pressure dependent viscosity in separate solutions, but were still unable to predect significant films. Experimental workers noticed, however, that grinding marks remained on gears after long runs in service, indicating that there must be a lubricant film. It was not until 1949, when Grubin (22) propounded his masterful simplification, that a solution was obtained involving both elasticity and pressure dependent viscosity. His work showed that films can exist which are very much thicker than had been previously thought possible, and it laid the foundation of elastohydrodynamic lubrication (EHL) theory. The first convincing measurements of such films were reported in 1958 by Crook (35) who used capacitance techniques.

## 3.2 Outline of EHL Theory

Elastohydrodynamic theory for point contacts involves the simultaneous

solution of Reynolds equation for hydrodynamics,

$$\frac{\partial}{\partial x}\left(\frac{h^3}{\mu}\frac{\partial p}{\partial x}\right) + \frac{\partial}{\partial y}\left(\frac{h^3}{\mu}\frac{\partial p}{\partial y}\right) = 6U\left(\frac{\partial h}{\partial x}\right)$$

a pressure viscosity relation such as

$$\mu = \mu_o e^{\alpha p} .$$

and the point contact elasticity equation

$$H(x,y) = \frac{x^2 + y^2}{2R} + \frac{2}{\pi E'} \iint_F \frac{p(x',y')}{\left[(x - x')^2 + (y - y')^2\right]^{\frac{1}{2}}} dx'dy' + \gamma$$

where the field of integration F covers an area round the contact and $\gamma$ represents the distance between undeformed parts of the bodies.

A complete solution of these equations has yet to be achieved but dimensional analysis can be used to organise the variables and give the result:

$$\left(\frac{h}{R}\right)_{x,y} = K\left(\frac{U\mu_o}{E'R}\right)^a \left(\frac{W}{E'R^2}\right)^b (\alpha E')^c$$

$$\begin{pmatrix}\text{Dimensionless}\\ \text{Thickness}\end{pmatrix} = K\begin{pmatrix}\text{Speed}\\ \text{Parameter}\end{pmatrix}^a \begin{pmatrix}\text{Load}\\ \text{Parameter}\end{pmatrix}^b \begin{pmatrix}\text{Materials}\\ \text{Parameter}\end{pmatrix}^c$$

where K is function of (x,y) only. These groups are analogous to those used by Dowson and Higginson (11) in their line contact theory, except that they use the speed parameter $\left(\frac{\bar{u}\mu_o}{E'R}\right)$ which is half the size of the one used here. Their values in line contact are

$$a = 0.7, \quad b = -0.13, \quad c = 0.6$$

An attempt at solving the theory is reported in Chapter 9.

## 3.3 Comparison of Experimental Techniques

In this thesis film thicknesses are measured by optical interference techniques. In addition to simplicity, these techniques have the great advantage of enabling the contour of the whole region to be mapped. As one

of the elements must be transparent, there is a limitation in the loads which may be applied, but this has been found to be less serious than originally expected. When glass, a much weaker material than ball-bearing steel, is used the contact pressures which can be achieved are lower. However, the glass-on-steel combination has an elasticity parameter E' about a half that of steel-on-steel, and therefore, equivalent deformation occurs at half the stress. The apparatus has run at nominal Hertzian stresses up to 100,000 p.s.i. which would be equivalent to 200,000 p.s.i. in a bearing, assuming the lubricant continues to obey the same pressure viscosity law. This assumption is supported by the failure to find discontinuities with increasing pressure by Gohar and Cameron (50), who tested a heavy petroleum oil at actual pressures up to 220,000 p.s.i. in a rig which used diamond as the transparent element. The slight chance that pure compounds might show some discontinuities still remains, but as the pressure is on for such a short time it is probable that the compounds stay liquid at pressures above the static freezing pressure in the same way that they can be momentarily super cooled.

A variety of other techniques have been used previously with various degrees of success. Electrical resistance has been of doubtful value, but voltage discharge, although of limited accuracy, is valuable as the only technique that can be used for contact between mating gears or cams and tappets (76). The two techniques which have been used most successfully for accurate measurements to date are X-ray transmission (43) and capacitance (41). In the former technique, a highly collimated beam of X-rays is fired through the conjunction between two rolling discs and the transmitted radiation received on a Geiger counter. The thickness is related to the number of radiation counts by a static calibration. In the latter technique, the capacitance between two rolling discs is measured and the film thickness

calculated from it. The main disadvantage, apart from expense, of the X-ray technique is that profile measurements are a shadow graph, and will be governed by the side closure of the contact and not by the profile which pertains over 95% of the disc width. The side closure of a point contact can be over 50% (Fig. 21) and may be even greater in some cases of line contact. The objection to inter-disc capacitance methods is that the capacitance measured in proportional to the integral $\frac{1}{\text{Thickness}}$ over the contact region, hence the film shape must be determined from EHL theory before its thickness can be found. Most workers assume a Grubin shape (as in Fig. 1) which is reasonable for line contacts, but can be very inaccurate for point contacts where deviations from the Grubin shape affect a much greater part of the contact (Fig. 21).

Crook (35) has used a capacitance pad technique to measure oil flows through the contact and therefore predict thickness. He has also used a very ingenious technique (39) in which a steel disc rolls against a glass disc with a thin chrome area deposited on its edge (Fig. 8); as the chrome strip enters the contact the capacitance is increased and the charging current measured on an oscilloscope.

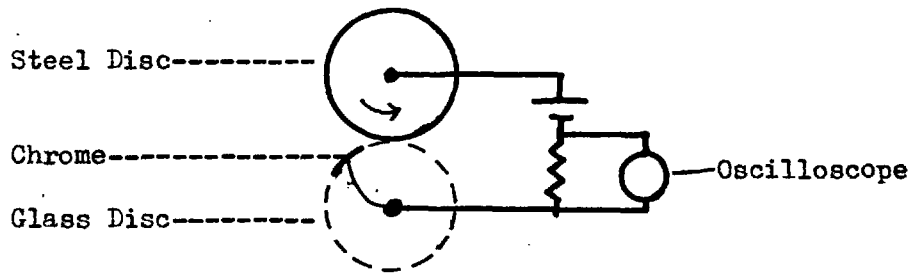



Fig. 8. Schematic Diagram of Crook's Capacitance Technique for Determining Film Shape.

This technique shows the film shape but as with all the preceeding techniques, would be difficult to apply to point contacts.

Archard and Kirk (45) have used capacitance to measure point contact film thickness in their crossed cylinders machine. This machine is excellent for studying wear, but operates at a slide roll ratio of about 100% which, except for cams and tappets, is not a typical operating condition for a rolling contact.

# CHAPTER 4 OPTICAL INTERFERENCE

## 4.1 Introduction

The theory of the formation of interference fringes is well known and is dealt with in a number of elementary texts, Tolansky (77) is particularly clear. If a beam of light is split into two parts which recombine after each has travelled a different distance, the intensity of the recombined beam depends on the difference in distance travelled. The intensity changes from a maximum to a minimum or vise-versa when their path difference is changed by $\lambda/2$ where $\lambda$ is the wavelength of monochromatic light in the medium concerned. If white light which is a continuous spectrum of wavelengths is used, the colour of the recombined beam depends on the path difference, because each wavelength or colour reaches its maximum intensity at a different path difference.

The method used for film thickness measurement is based on the classical technique of Newton's rings. These rings are formed if a large focal length lens is placed on a flat glass plate, and can be observed with the naked eye. Part of the incident light is reflected by the lower surface of the lens and part travels through the air gap and is reflected by the glass plate. The fringes obtained in this way are very poor for a number of reasons.

## 4.2 Conditions for good fringes

### 1) Coherence and Collimation

Interference at a point in space, is most simply explained as the addition of two sine waves in such a way that their amplitudes either reinforce or cancel. As the intensity at the point must be constant the phase difference between the two waves must not vary with time. The only way to ensure this, is for the two waves to come from the same point on the source. The type of source is also important.

In an ordinary light source, such as a tungsten filament or gas discharge lamp, the individual atoms radiate regular wave trains for short periods only. This means that the light is composed of short wave trains which are emitted at random times. The average time for which an individual atom radiates continuously is known as the coherence time $T_{coh}$ and the length of wave train emitted in this time as the coherence length $L_{coh}$, $L_{coh}$ and $T_{coh}$ measure the temporal coherence of the light source, that is how well disturbances at the same point but different times correlate. $L_{coh}$ determines the maximum distance over which interference can be observed, and varies from a few thousand angstroms for a tungsten light to about 8 centimetres for sodium light and several metres for lasers. The spatial coherence is the degree of correlation between wave trains emitted at the same time but from different elements of the source.

Using the full coherence theory it is possible to design an optimum illuminating system for any interference set up. Dr. H. H. Hopkins of Imperial College kindly designed the illuminating system used in this work. The main principles of the design are that all the light illuminating a point in the interference plane should come by the same route from a single point in the source, and that adjacent rays should be parallel. It is only possible to achieve light in which all rays are parallel if an infinitessimal aperture is placed at the focal length of a perfect lens. With a finite aperture the resulting beam diverges but adjacent rays are effectively parallel. This is known as collimated light. The rays should not come to a focus at any time before reaching the interference plane, which rules out the use of concave mirrors behind or condensing lenses in front of the lamp.

2) Fringe visibility

The fringe visibility is governed by the intensity distribution within the fringe pattern. If the collimation and coherence are adequate

the intensity distribution due to two interfering waves is:

$$I = I_1 + I_2 + 2\sqrt{I_1 I_2} \cos\left(\frac{2\pi}{\lambda} p\right)$$

where $I_1$ and $I_2$ are the individual intensities of the two beams, $\lambda$ the wavelength, and $p$ the path difference.

$$\therefore \; I_{\substack{max \\ min}} = I_1 + I_2 \pm 2\sqrt{I_1 I_2}$$

The visibility V is given by

$$V = \frac{Imax - Imin}{Imax + Imin}$$

$$= \frac{2\sqrt{\frac{I_2}{I_1}}}{1 + \frac{I_2}{I_1}}$$

Hence for 100% visibility the intensities $I_2$ and $I_1$ should be equal. The achievement of this intensity ratio is dealt with in the next section.

4.3 Design of Optical System

In section 4.1 it was said that Newton's rings can be obtained by placing a curved lens on a flat mirror. In this work a flat plate of glass is placed on a curved mirror; the mirror being a highly polished 1" diameter steel ball Fig. 9. In addition there is oil instead of air in the gap. The area of interest is so small that it must be observed with a microscope. 50 times magnification using X5 objective with X10 eyepiece has been used so far, but greater magnification may be necessary in future.

To achieve good collimation it is best to put the collimator under the objective as it is very difficult to collimate light through the objective lens. A X5 objective has a working distance of about 1" which is adequate. In particular, commercial side illuminators are usually designed

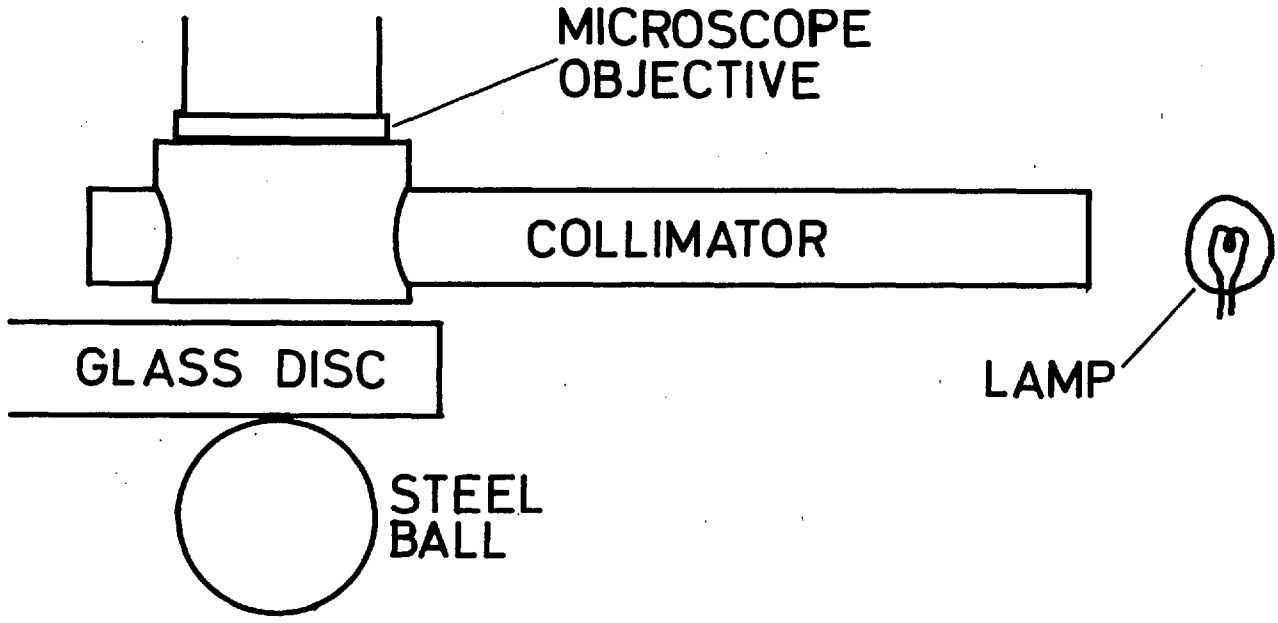



Fig. 9 The optical assembly

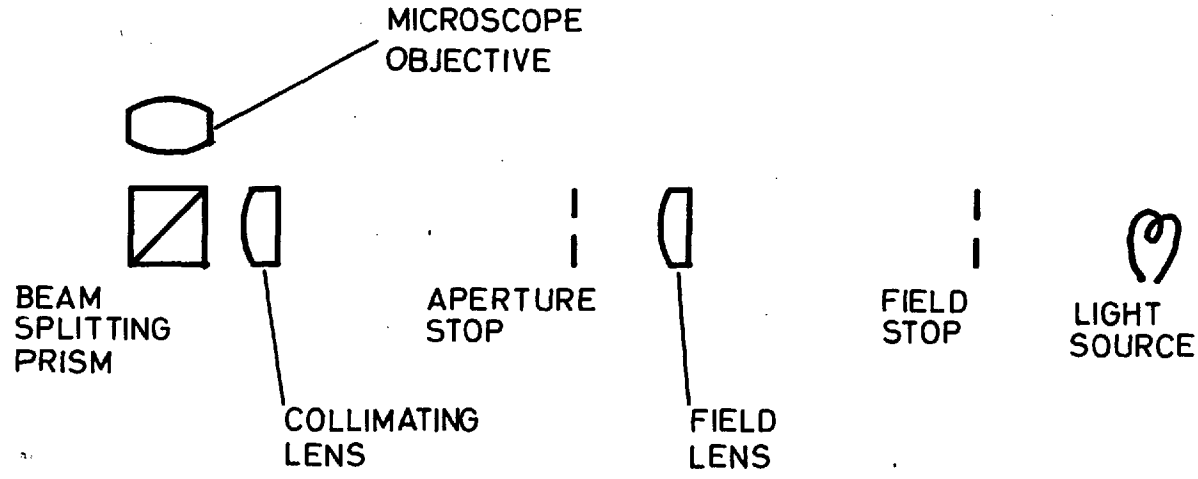



Fig. 10 Arrangement of lenses

to upset collimation, as in most microscopy Newton's rings have to be avoided, not created.

The collimator was made in the laboratory from some pieces of brass and is shown in Fig. 9. The arrangement of lenses is shown in Fig 10. The aperture stop is positioned to be in focus at infinity. A larger stop lets through more light at the expense of poorer collimation. The field stop is in focus at the image plane of the microscope, its size controls the area of source used and area illuminated. By limiting the area of source used the effects of spacial incoherence are minimised.

4.4 Achievement of Fringe Contact

As discussed in section 4.2 the fringe contrast (visibility) depends on achieving interfering beams of equal intensity. In the classical Newton's rings experiment, using a flint glass lens and plate with air fringes, both the glass-air, and the air-glass interfaces reflect 5% of the incident light, so perfect visibility results although the overall illumination will be low as only 10% of the light is used.

The reflectivity at an interface is

$$r = \left( \frac{n_1 - n_2}{n_1 + n_2} \right)^2 .$$

where $n_1$ and $n_2$ are the refractive indices of the two media. As oil and glass have similar refractive indices no reflection will occur with oil present. To overcome this problem Gohar and Cameron (33) used a special high refractive index glass ($n = 1.94$) this gives a glass/oil reflectivity of 1.3% (assuming $n_{oil} = 1.54$ for high pressure oil). The reflectivity of the steel ball is about 60%, which means that the visibility calculated as in section 4.2 is 29%. This is one reason for the poor fringe quality they achieved. The other reason is poor collimation due to the use of an above lens metallurgical side illuminator.

To achieve the necessary reflectivity from the glass oil interface a thin layer of chromium is deposited on to the glass by thermal evaporation. Chromium is chosen because of its good resistance to abrasion and corrosion compared with silver or aluminium; it also provides a surface which is of a similar chemical nature to ball bearing steel. The chromium was deposited to give a reflectivity of approximately 20%, such a film also absorbs a considerable amount of light (say 20%). The intensities resulting from such a system are shown in Fig. 11.

4.5 Multiple Beam Fringes

The preceding discussion assumes that all the reflected beams after the first two are negligible, which is so for low reflectivities. In the case in Fig. 11 the third beam (shown as a broken line) has an intensity 12% of the second. The effect of this is to make the outside of dark fringes lighter. Tolansky (77) has developed the theory of these multiple beam fringes and using reflectivities of 90% or more obtains Newton's rings in which the black rings are reduced to fine black lines. These lines can be as narrow as one fiftieth of a fringe order (i.e. 1/50 of the distance between adjacent black fringes). If it were possible to use this system for oil film measurement the thickness at a point on a line would be determined to within less than 40 Å. Unfortunately the absorptions of the reflecting films must be kept very small. It might be possible to obtain the required values by using a silvered disc and a silver plated ball, but the silver plating would probably flow plastically under the stresses involved and would certainly be much more easily abraded than the chromium. Even if multiple beam fringes could be obtained, there still remains the problem that the separation of black fringes will be about 2000 Å which is a coarse unit of measurement.

4.6 Colour Fringes and Calibration

If the system is illuminated with white light, coloured fringes result.

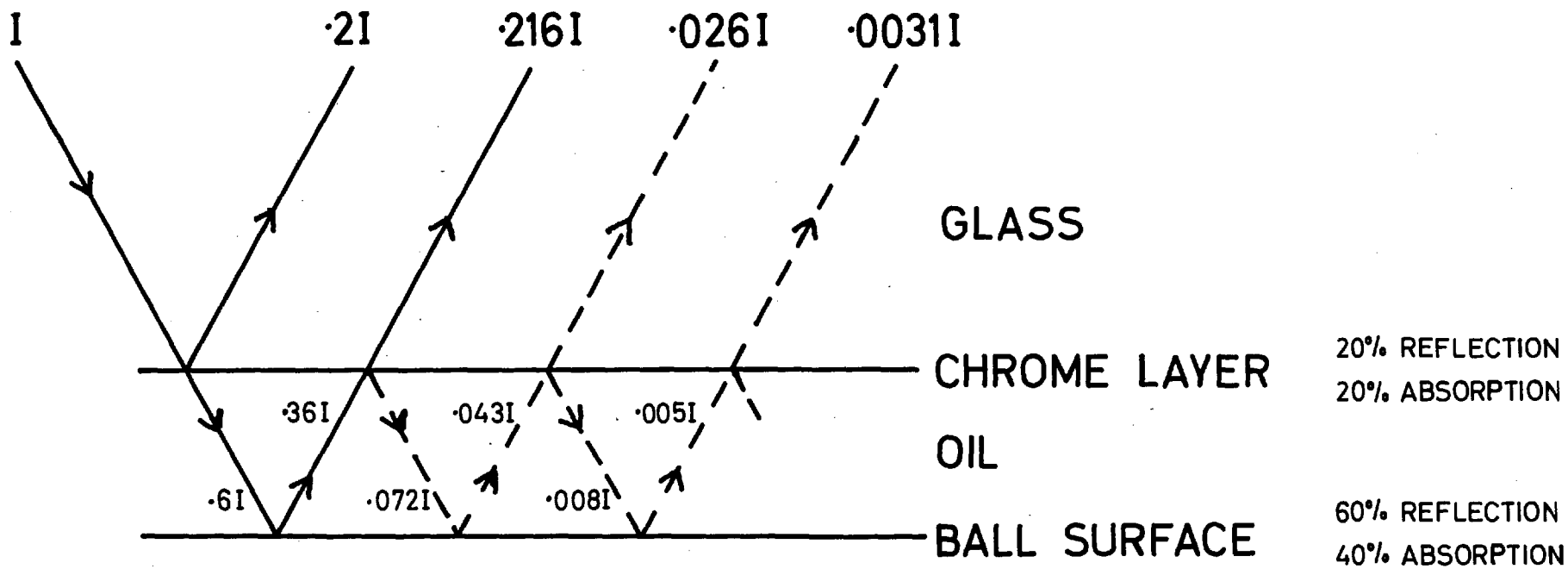



Fig. 11 Intensities on reflection

The colours depend on the path difference, and provide much finer detail than black and white and also have the advantage that the thickness at a point is given by a recognisable colour whereas a black fringe of $\lambda/2$ path difference is identical to one of 5 $\lambda/2$. The disadvantage of colour is the limited thickness which can be measured. As the colours are formed by mixtures of wavelengths in various proportions it is impossible to predict the path difference causing each colour, so the system must be calibrated experimentally.

The colour fringes must be calibrated by observing a system of known geometry with the same light source and optics as will be used for testing. The obvious system to observe in this work is the undeformed ball in contact with the glass, but unfortunately the fringes are so close together that all the dark colours merge to form black and the light ones to form white. This problem could be overcome by using a much larger ball if one could be obtained, but for this work the spherical surface of a lens was thickly plated with chromium so as to simulate the surface of 12.64 centimetres radius ball. The lens is raised until it just touches the glass plate Fig. 12, the thickness h in the centre is thus zero and at a radius r, $h = \frac{r^2}{2R}$ where R is the radius of the lens. A set of coloured ring is formed as in Fig. 20E. The radius r, at which each colour is most intense is measured using a filar eyepiece and h calculated for each colour. In these tests the chromed lens and glass are carefully cleaned so that the medium between them is air of

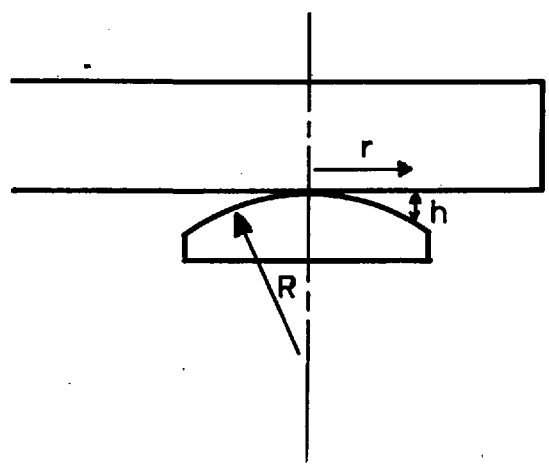



Fig. 12 Calibration system

refractive index 1.0. When an oil of refractive index n, is between the surfaces the wavelengths of the light, and thus the thickness 'h' for each colour is reduced such that:

$$h_{actual} = \frac{h_{observed}}{n}$$

For most oils $n \approx 1.5$.

A full colour calibration chart is not included because of human differences in definition of colours and because fluids differ in refractive index. However some of the strongest colours in the photograph in Fig. 20 are approximately

| | | |
|---|---|---|
| 1st orange | (in lobes of blue photographs) | $1.9 \times 10^{-5}$ cm |
| 2nd blue | (centre of blue photographs) | $2.5 \times 10^{-5}$ cm |
| 2nd purple | (centre of purple photographs) | $3.85 \times 10^{-5}$ cm |

The author's calibration for some colours using a tungsten lamp of colour temperature 3,200 K is shown on the vertical axis of Fig. 19, but these are equivalent air thicknesses and specific to the particular light and chromed disc used.

4.7 Light Source and Photography

An important factor in colour photography is that the spectral response of the film must suit the spectral composition of the light source, if accurate colours are to be achieved. Spectral compositions in photography are denoted in terms of the colour temperature, which is the temperature at which a black body would have to radiate to produce a specified composition. Kodak High Speed Ektachrome B film is balanced for artificial light with a colour temperature of 3,200 K (i.e. photoflood lights). A suitable source can be achieved by adjusting the voltage of a low voltage compact source tungsten lamp according to manufacturers data.

The determination of exposure is also critical and must be done by trial

and error, this process can be cheapened and speeded up by using a black and white film of similar speed to determine the approximate exposure, before finding the exact one with the colour film. Another pitfall in colour photography, known technically as reciprocity failure, is that the "half the intensity - double the time" rule breaks down in cases below a certain intensity and the exposure time has to be longer than expected. A more serious corollary is that the slides are given a cyan (blue-green) cast. Most of the slides were taken with an exposure time of $\frac{1}{2}$ second at which the effect is slight as can be seen in Fig. 20. The exposure time could be reduced by fitting a larger aperture in the collimator, but this would make the microscope picture too bright for normal viewing as well as reducing the collimation. A 50 watt 12 volt quartz iodine bulb has recently been used successfully and allows the exposure time to be reduced to 1/5 second without loss of collimation.

The black and white photographs Fig. 25 were taken using mercury green light and a special high speed film which is sensitive in the green range.

4.8 Refractive Index of Oils

The refractive indices of the oils used were measured using an Abbé refractometer, and are easily corrected for the change in pressure provided that the density change is known. The refractive indices of most petroleum oils are in the range 1.45 — 1.55 but for fluorocarbons the index is 1.3 and for some ethers is 1.68. At 66,000 p.s.i. they increase by up to 10%, the calculation is given in section 6.2.

The use of the relation

$$h_{actual} = \frac{h_{observed}}{n}$$

has been questioned (79) because the refractive index 'n' for an oil is a function of wavelength (78). The refractive index at the blue end of the spectrum is likely to be higher than that at the red end, consequently in

any experimental test the "blue" points would have to be divided by a higher value of 'n' than the "red" points. This means that "blue" points will tend to lie above the true experimental line and "red" points below. In the testing of over 40 fluids no evidence of this systematic scatter has occured, indicating that the error must be small. As a further check, a test has been carried out in which the author's existing air calibration is used to plot the shape of the chromed lens using white light, when the gap is filled with a 5 phenyl-4-ether fluid. The shape plotted in this way shows excellent agreement with that obtained by illuminating the same system with monochromatic light, Fig. 13. Nothing but the light sources are touched in any way between the tests. As the fluid used is one of those most likely to exhibit a marked refractive index dispersion (79), this test provides very strong evidence that the refractive index dispersion is insignificant in affect. The small thickness at which the 1st black fringe occurs in Fig. 13 is due to the phase changes on reflection.

4.9 An Ideal Light Source

The coarseness of monochromatic fringes as a unit of measurement, and the limited maximum thickness of white light fringes, emphasize the need for a source which gives, say four widely spaced but very intense spectral lines, so that in effect four superimposed sets of monochromatic fringes are obtained. Existing sources which approach this such as low pressure mercury or various mixed gas discharge lamps are not sufficiently intense for good photographs to be obtained under conditions of good collimation and high magnification.

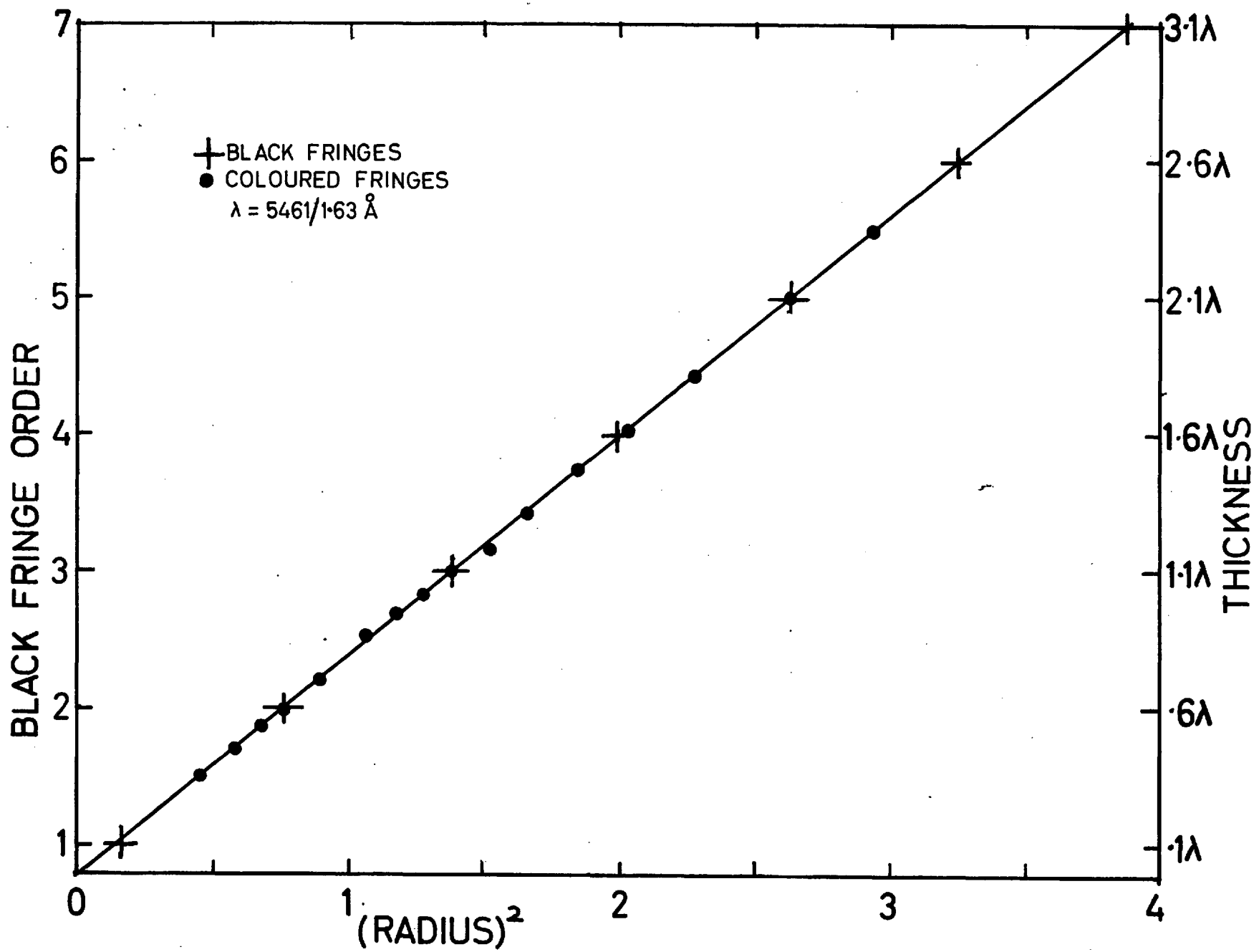



Fig. 13 Callibration check

# CHAPTER 5 DESIGN OF MECHANICAL APPARATUS

## 5.1 The Successful Apparatus

The apparatus used for most of the testing is shown in Figs. 14,15. A specially coated glass plate is mounted on an air bearing and driven by a super finished 1" steel ball which is mounted in a PTFE cup*. The ball is loaded against the lower surface of the disc by an air cylinder, and rotated by a variable speed electric motor. Oil is drip fed on to the ball and drawn into the contact, where an elastohydrodynamic film is generated and its thickness measured by optical interference as described in Chapter 4.

## 5.2 Earlier Designs

Gohar and Cameron (33,50) loaded a lubricated rotating ball against a stationary plate of high refractive index glass or a diamond surface, and obtained interference patterns from which the film shape in sliding point contacts could be determined. The reasons for their low fringe visibility are discussed in section 4.4.

In his PhD thesis Gohar (80) reports the design of an air bearing rig to investigate the film thickness in rolling point contact. This rig was the starting point of the authors investigation into film thickness. A 6" diameter $\frac{1}{4}$" thick disc of high refractive index (1.94) glass was mounted on an air bearing and drove a freely mounted 1" steel ball through the oil film. The fringe visibility was lower than with the sliding rig of (33,50) and the fringes were erratic, which made oil film measurement nearly impossible. The poor results stem principally from the use of the high refractive index glass, which as well as being very expensive and difficult to obtain in large pieces suffers from mechanical and chemical instabilities due to its high lead content. The glass plate warps causing

* Glacier DU

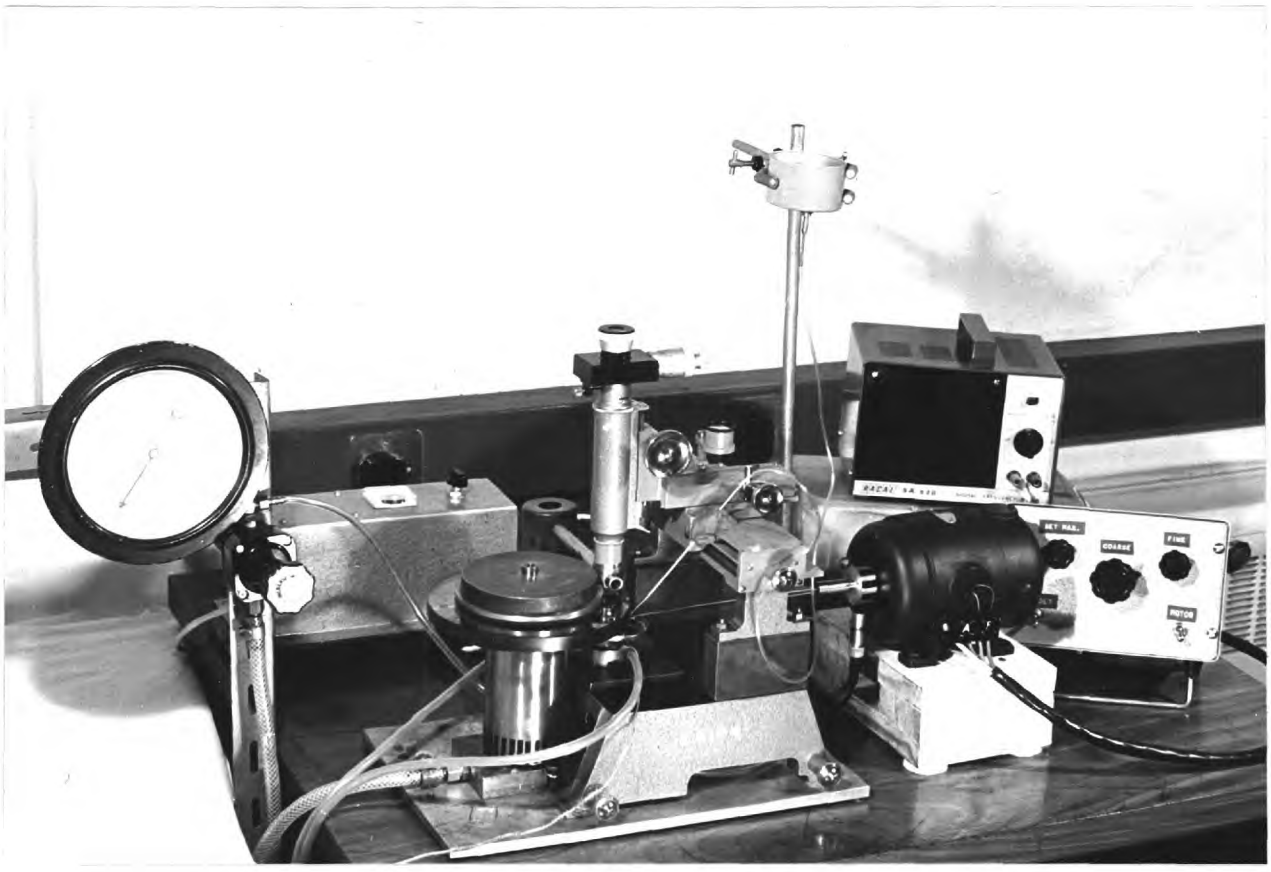


Fig. 14 The optical elastohydrodynamics rig

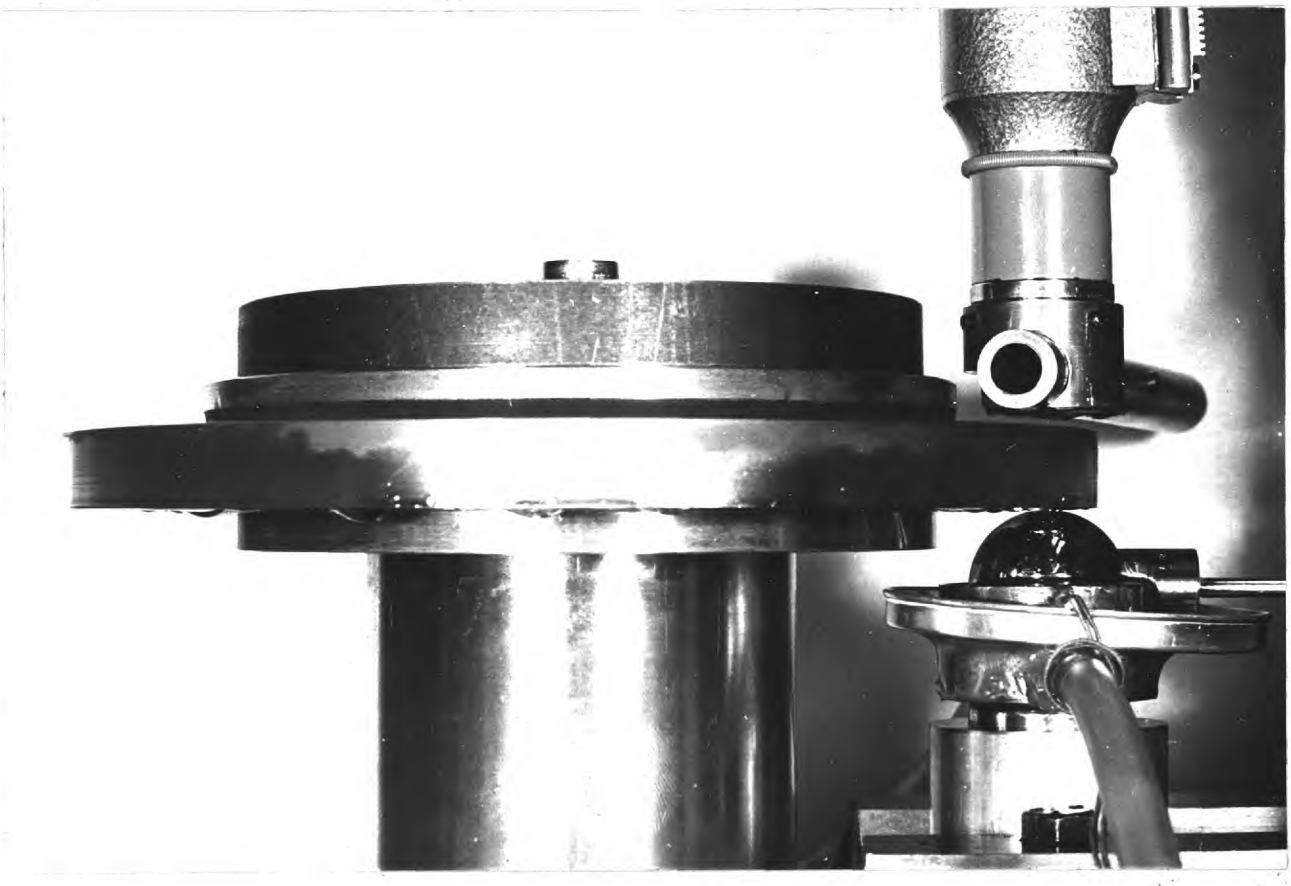


Fig. 15 The ball and disc assembly

the fringes to move as the disc rotates. The tarnish which is formed on the surface by the action of air on the lead in the glass, acts as a thin interference film either augmenting or reducing the reflection as its thickness changes. In sliding the tarnish is rubbed off, but on the rolling rig the tarnish film remains and varies in thickness round the circumference thus confusing the results. The sulphur in the air, which forms lead sulphide, is the main culprit, but sulphur compounds in the oil may also contribute. When high lead glasses are used commercially they are bloomed immediately after polishing to prevent tarnish forming.

The ball loading system proposed by Gohar Fig. 16 is similar to that used by Hingley in his pitting experiments (1), but with air behind the ball instead of oil. This system has low friction, but when oil is applied to the contact, a hydrodynamic film tends to form in the clearance gap

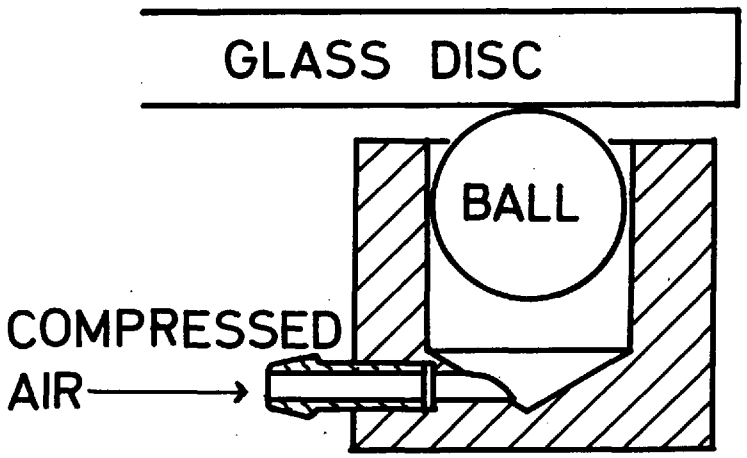



Fig. 16
Hingley type loader

between the ball and cylinder. From time to time this film is blown away by the air pressure, and causes the ball to jump. This trouble was lessened by reducing the clearance, but could not be eliminated.

5.3 Improvements on the Earlier Design

The principal improvements on the earlier design are that a specially coated plate glass disc and correctly designed collimator are used, and that the ball is mounted in a PTFE cup and drives the disc. In addition many detail improvements have been made.

## 5.4 The Glass Disc

The disadvantages of the high refractive index glass are overcome by using a disc of $\frac{1}{2}$" thick plate glass coated with 20% reflectivity chromium film. The disc is specially selected, from a sheet of float glass, to be flat within one or two wavelengths of light. Float glass is of the crown type and has excellent mechanical and optical properties. The top surface of the disc is bloomed with $MgF_2$ to reduce spurious reflections. Such a disc is about one fifth of the cost of the high refractive index disc. More than twenty five fluids have been tested on one track of the disc. Some sliding tests in which the disc is stationary have been carried out without much damage to the chromium.

## 5.5 The Loading System

The ball is located in a PTFE cup which is mounted on a 1 inch piston which rides freely in a cylinder. The cylinder is fed with compressed air thus loading the ball. The reasons for choosing this system are that the load is very easily controlled by a pressure regulator, and that the system has low friction and inertia which enables the ball to follow any unevenness in the disc. The piston is hollow to keep its weight down. The centre line of the ball is about .010" behind the centre line of the piston, so that when the ball rotates the cup will "caster" behind the piston and take up a stable position.

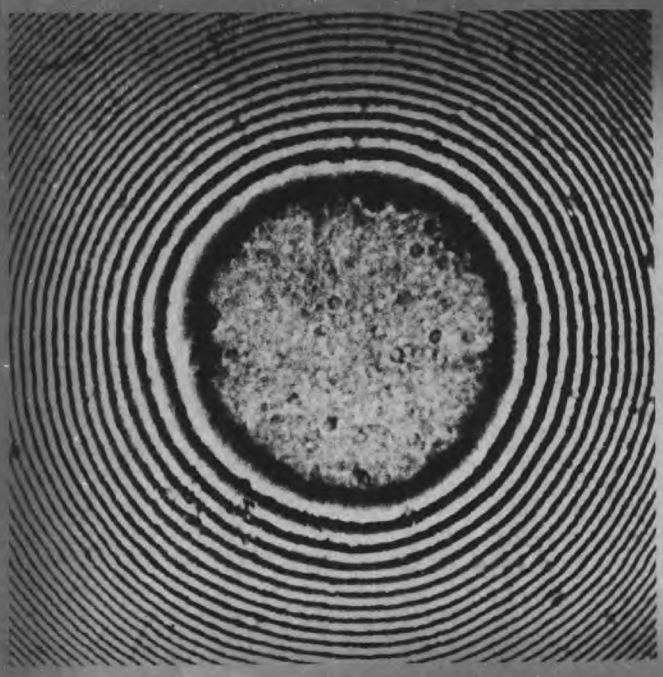
To reduce frictional heating and remove the danger of embedded debris scoring the ball, much of the lining of the cup is scraped away leaving 4 pads to support the ball. Most of the heat generated by friction in the PTFE cup is carried away by water from a thermostatted bath which is circulated below the cup. A fine chromel-alumel thermo couple is attached to the cup and projects into the oil film ahead of the contact. This method of temperature measurement is robust and was found to be adequately sensitive.

The main disadvantage of this loading system is that heat is generated by shearing of the oil film in the cup. Other systems have been considered

but so far the balance of advantage lies with the present one. In particular, any system which involves air in contact with the ball presents problems of the oil being sprayed everywhere and wasted and also necessitates control of the air temperature. Hydrostatic systems require an oil feed circuit and therefore use far more oil than the 5 mls used by the present system, they are also difficult to clean between tests. The only other class of system is one in which a ball is mounted on, or made integral with, a shaft, and this shaft mounted in suitable bearings. Such a system overcomes the disadvantages of the others but would be extremely difficult and expensive to produce to the required standard of accuracy and ball surface finish, especially as the ball has to be replaced fairly frequently. A ball has been used for routine testing of as many as 25 fluids; but with very thin fluids, high loads or sliding tests the life may be only 2 or 3 test runs. Nine balls have been used for the work covered by this thesis. The present balls have a surface finish better than 1 micro-inch CLA and are round to within 4 micro-inches, which means that the run-out will be of this order when they are rotated in the present mounting system. Fig. 17 shows Talysurf traces for standard and super-finished balls (this super ball is from an earlier batch and is 10 micro-inches 0.0.R). Stationary Newton's rings for each ball are also shown.

## 5.6 The Drive System and Speed Measurement

The ball is driven by a variable speed electric motor, through a flexible coupling and a drive shaft which is cemented on to the ball with an expoxy resin. The flexible coupling prevents the shaft applying any load to the ball, accomodates misalignment and delays the onset of shaft whirling. A very effective coupling was found to be a short length of plastic tubing at the motor end of the drive shaft. At very low speed "stick-slip" occurs in the cup due to the torsional flexibility of this






STANDARD






SUPER

FIG 17 SURFACE FINISH OF BALLS

coupling. Under these conditions a Hooke's joint is used.

Owing to the great range of fluid viscosities a very wide speed range from 1 to 6000 rpm is required. This is achieved by using a variable speed motor which will run satisfactorily between 100 and 6000 rpm and either a direct drive or a 10:1 or 100:1 reduction gear. Originally a 1/15 HP at 4,500 rpm universal series motor with a proprietary speed control which uses a single thyristor to provide half wave rectified pulsed DC was used, the regulation was rather high but at constant load the speed was reasonably stable.

To achieve the best control, a thyristor control must be built to suit the particular motor, this has been done using an AEI TR2-A module which contains most of the elements of a thyristor control but requires some auxiliary circuitry which depends on the type of motor and intended use. The system has been made with a fine and a coarse speed control and maximum speed setting. Regulation of the order of 1% between no load and full load is anticipated when the system has been perfected.

The speed of the motor is measured by using either a magnetic or photoelectric pick up and an electronic impulse counter. Provided that care is taken to screen the wires and earth the motor and rig to minimise interference, speed can be very conveniently measured to within 1% over the entire range.

## 5.7 Slip Measurement

Because the friction of the air bearing is very low, the ball and disc are expected to be in almost pure rolling. The amount of slip actually occuring can be measured by counting on two digital counters, impulses generated by the ball rotation and by the disc rotation. The two counters are started simultaneously by throwing a double pole switch, and operated for a long enough time to give a count accuracy of 1 in 10,000. The track

radius to the centre of the contact is measured to within .002 inches (less than 0.1%) using a travelling microscope. The overall accuracy is therefore 0.1%. Measurements were made using a thin, a medium and a thick fluid (7,60 and 900 centipoises viscosity) over speed ranges that covered the test conditions. The slip defined as $(u_1 - u_2) / (u_1 + u_2)$ was found to vary between .1% at low speed and .7% at high speed. As the slip is so small only the ball speed is measured in subsequent tests.

5.8 The Air Bearing

The air bearing was designed by Dr. R. Gohar whom the author would like to thank and was made in the Mechanical Engineering Department workshops. The design Fig. 18 is based on that of an N.E.L. surface table (81) and uses six .020" diameter jets in each journal ring and one for thrust. Each jet is set in a .125" diameter .005" deep pocket. The bearing is fed with air between 60 and 80 p.s.i. and operates with a low air consumption which enables it to be run from an air bottle if shop air is not available. The run down time of the bearing is 20 minutes from 1000 rpm.

The load that can be applied by the ball is limited by this air bearing which was designed before the full capabilities of the glass contact were realised. The reaction to the ball load is provided by the weight of the bearing rotor plus the weights which can be attached to it, the practical limit for testing is 10 lbs which gives a maximum Hertz stress of 83,000 $lb/in^2$ but tests have been carried out at 15 lbs which gives 96,000 $lb/in^2$.

The design of an improved air bearing is discussed in Chapter 10.

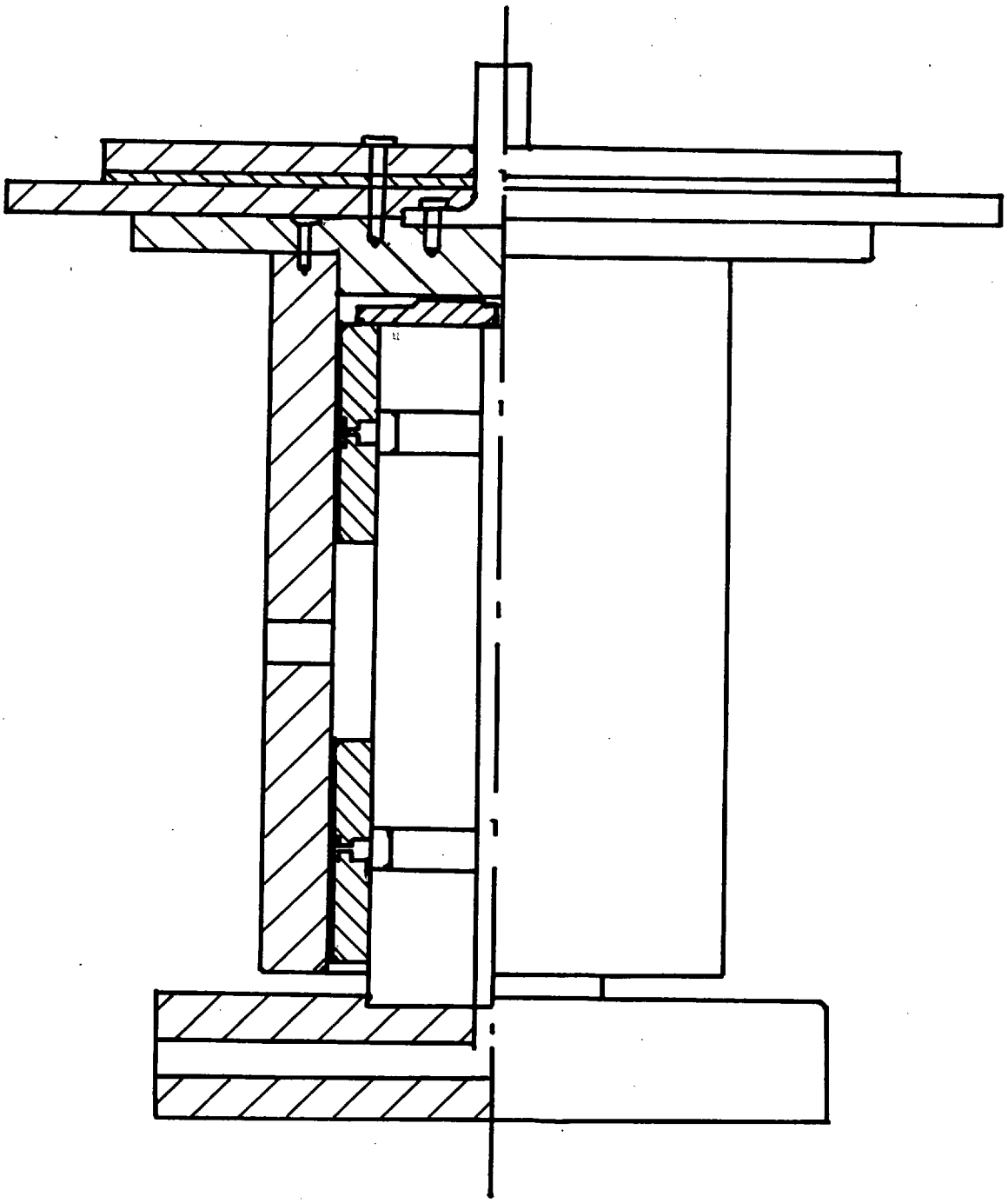


Fig. 18 The air bearing

# CHAPTER 6 EXPERIMENTAL MEASUREMENT

## 6.1 Method of Evaluating Fluids

Having developed a fairly quick and accurate technique and apparatus for oil film measurement it is necessary to consider the most valuable way of using it. Many synthetic lubricants are now being developed whose chemical structures and physical properties are very different to those of conventional petroleum oils. It is therefore of value to test these fluids in an apparatus which simulates many of the conditions in real bearings. Most of the testing consisted of running a large number of fluids at the same load and temperature in order to determine the effect of fluid properties and speed on the thickness and shape of the oil film. A complete test can be carried out on 5 ml of fluid or less which means that expensive lubricants and fluids prepared in test-tube quantities can be evaluated.

The film thickness is strongly affected by lubricant viscosity and, therefore, temperature. If the ball is run at a constant speed, the fringe colours remain the same until the temperature measured by the thermocouple increases by about 1/2 degree F. At low speeds the ball can be run indefinitely without any temperature rise, but at higher speeds readings must be taken quickly, since ultimately the temperature rises too rapidly for valid readings to be taken. The low scatter obtainable is shown by the points in Figs. 19 and 22. The temperature rise limits the speed range which can be investigated.

## 6.2 Standard Procedure

Most of the tests are run at a load of 5 lb, a convenient figure giving maximum Hertz stress of 66,600 p.s.i, and at a temperature of 77 F. The standard procedure is to gradually increase the ball speed and note the speed at which each calibrated colour is clearest over the central area of the contact. The tests are stopped either when the limit of clear

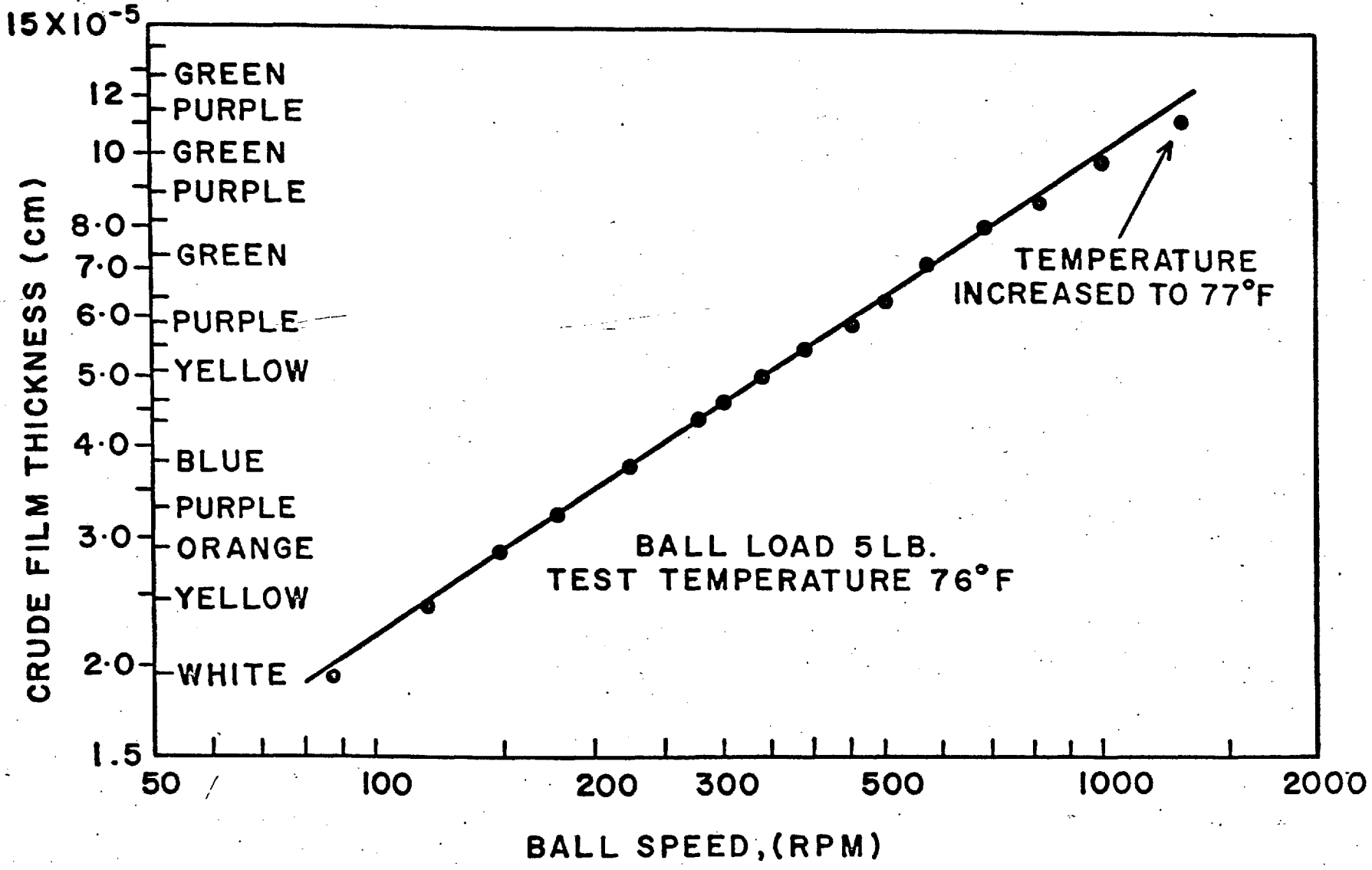



Fig.19. Color versus Speed for Oil No. 5.

fringes is exceeded (at about $10^{-4}$ cm) or when the temperature of the oil starts to rise rapidly and increases by more than 1 degree F. The speeds are plotted on log-log paper with the colours marked on one axis and the best straight line is drawn, Fig. 19. Any points which do not fall on the line are redetermined. The conversion to dimensionless co-ordinates is usually carried out by processing the line from Fig. 19, but in order to show the scatter, individual points are plotted in Fig. 22.

To calculate the film thickness from the relation, $h_{actual} = \frac{h_{observed}}{n}$, it is necessary to know the refractive index of the oil in the contact at the pressure of 66,600 p.s.i. The Lorenz-Lorenz equation can be used to relate the refractive index and density of a substance as follows:

$$n_p = \left(\frac{1 + 2A}{1 - A}\right)^{\frac{1}{2}}, \qquad \text{where } A = \frac{\rho_p}{\rho_o}\left(\frac{n_o^2 - 1}{n_o^2 + 2}\right)$$

and $n_o$ and $\rho_o$, $n_p$ and $\rho_p$ are the refractive indices and densities at atmospheric pressure, and the test pressure p, respectively. $\frac{\rho_p}{\rho_o}$ is obtained from Hartung's empirical formula for hydrocarbons, (57),

$$\frac{\rho_p}{\rho_o} = 1 + \left(\frac{42.8 \times 10^{-6}}{(\nu_{100})^{0.0385}}\right) p^{0.75}, \qquad \text{where } \nu_{100}$$

is the viscosity in cS at 100 F. When it is available, bulk modulus data can be used and was for most of the non-hydrocarbons tested.

A simple computer program is used to evaluate this refractive index change and to evaluate the thickness $\left(\frac{h_o}{R}\right)$ and speed-viscosity $\left(\frac{U\mu_o}{E'R}\right)$ parameters. For the latter two calculations the factors which remain constant in all tests are:

$E_1$ = 11 x $10^6$ lb/in$^2$ for glass*

$\sigma_1$ = 0.25 for glass*

* Data supplied by manufacturer.

$E_2$ = $30 \times 10^6$ lb/in$^2$ for steel

$\sigma_2$ = 0.3 for steel

$E'$ = $17.4 \times 10^6$ lb/in$^2$ = $12 \times 10^{11}$ dynes/cm$^2$

$R$ = 0.5 in = 1.27 cm

$a$ = $3.50 \times 10^{-3} W^{\frac{1}{3}}$ in

and $p_{max}$ = $3.90 \times 10^4 W^{\frac{1}{3}}$ lb/in$^2$

also $\frac{U}{R} = \frac{u_1 + u_2}{R} = 4\pi \frac{\text{RPM of Ball}}{60}$

and $\frac{U\mu_o}{E'R}$ = $1.745 \times 10^{-15} \mu_o$ (Ball RPM)

where $\mu_o$ is in centipoises cP.

For the fluid comparison tests, Fig. 22 and Table 1:

$W$ = 5 lb

$a$ = $5.98 \times 10^{-3}$ in

$p_{max}$ = 66,600 lb/in$^2$

$\frac{W}{E'R^2}$ = $1.15 \times 10^{-6}$

Photographs of the contours are taken using a microscope camera with an artificial light, high-speed film (Kodak High Speed Ektachrome B) which is balanced for the same colour temperature as the source lamp. As far as possible, two photographs are taken on each fluid, one when the central area is the strong second-order blue (thickness about $2.5 \times 10^{-5}$cm), the other at the second-order purple (thickness about $3.8 \times 10^{-5}$cm). A selection of the blue centre ones is shown in Fig. 20, A,D,G,J.

6.3 Tests at Different Loads

In addition to the standard fluid evaluation tests the effect of load is studied using a polyisobutylene oil (oil 5) and a 5 ring polyphenyl

ether (oil 31). Tests are run over a wide speed range at each load, and the fringes photographed (Fig. 20, H,K,F,I,L and Fig. 25).

6.4 Tests Over a Wide Speed Range

The use of a viscous oil (oil 31) enables the apparatus to be run at much higher dimensionless speeds before temperature rise becomes a problem. The thicker films generated, mean that monochromatic fringes (mercury green in this case) must be used.

The black and white photographs (Fig. 25) are taken on Kodak R60 panchromatic film which is recommended by the manufacturers for this work. The author would prefer however to sacrifice a little film speed in order to get higher contrast and finer grain. A reflex camera and microscope adaptor were used for these photographs.

6.5 Sliding and Friction

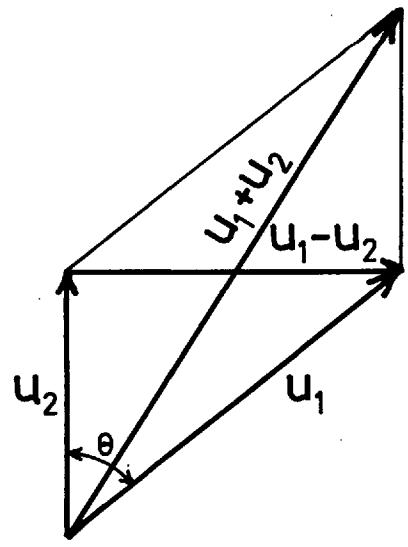
Tests in which the slide roll ratio $(u_1 - u_2) / (u_1 + u_2)$ is 1 are carried out by rotating the ball against a stationary disc. The friction is determined by measuring the torque required to prevent the rotation of the air bearing.

6.6 Sliding due to Angled Drive

If the axis of ratation of the ball is moved through an angle $\theta$ the rolling velocity becomes $u_1\sqrt{1 + 3\cos\theta}$ and a sliding velocity of $u_1 \sin\theta$ is introduced. The rolling velocity is the vector sum, and the sliding velocity the vector difference, of the surface velocities of the ball and disc as shown in the vector diagram; $u_1$ is the surface velocity of the ball, and $u_2$, the velocity of the disc, is equal to $u_1\cos\theta$.

A test was run using oil No. 31 as lubricant with an angle $\theta$ of 18° which gives a slide roll ratio of 0.16.

Cameron (88) also used an angled drive to produce sliding.




Vector diagram for the angled drive

## 6.7 Squeeze Film

Some effects of elastohydrodynamic squeeze film lubrication can be observed if the ball is loaded suddenly against the disc. The sudden loading is achieved by holding down the loading piston against a predetermined air pressure and suddenly releasing it, so that the ball rises and strikes the disc. No systematic study has been made, but some observations are reported in the next chapter.

# CHAPTER 7 EXPERIMENTAL RESULTS

## 7.1 Fluid Comparison

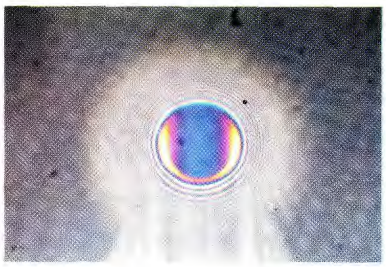
The coloured photographs in Fig. 20 and cross sections Fig. 21 show the contours produced by a number of fluids run under various conditions of speed and load. In particular Fig. 20 A,D,G,J, shows the effect of fluid structure at constant load and film thickness. To obtain these conditions, the rolling speed is adjusted to give the same central colour (2nd blue which is a thickness of approximately $2.5 \times 10^{-5}$cm). The same effect is found at other speeds and a similar set of transparencies in which the centres are 2nd purple (approximately $3.8 \times 10^{-5}$cm) has been obtained, in this case the lobes are all 1st orange (approximately $1.9 \times 10^{-5}$cm). The only areas in which there are slight differences are in the inlet region and in the cavitation zone at the outlet. The cavitation zone, though interesting, is not relevant in the present discussion, as its pressures are low and its influence on film shape negligible. The finding of slight variation in the inlet zone supports the arguments of Dowson (11) and others that the inlet zone is all-important, because once the fluid is in the centre it cannot escape, and therefore its properties at this point do not effect the thickness and contour of the contact region. The comparison between different fluids is made by noting the speed at which each colour occurs in the centre of the contact. Using this information dimensionless thickness versus speed parameter graphs are drawn for all fluids (see section 6.2). Fig. 22 shows four typical lines, those for the other fluids are specified in Table 1 by giving the slope "a" and $\left(\frac{h_o}{R}\right)_4$ which is the value of $\frac{h_o}{R}$ at $\frac{U\mu_o}{E'R} = 4 \times 10^{-11}$. The interpretation of these results is discussed in Chapter 8.

## 7.2 The Effect of Load

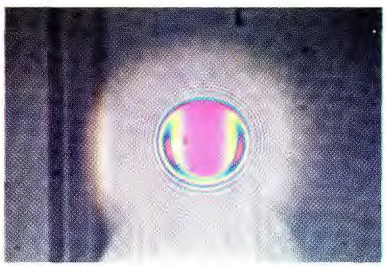
The effect of load is shown by Fig. 20 H,K,F,I,L, these contours

Fig. 20 Contours of the Elastohydrodynamic Contact Regions (magnified 37 times)

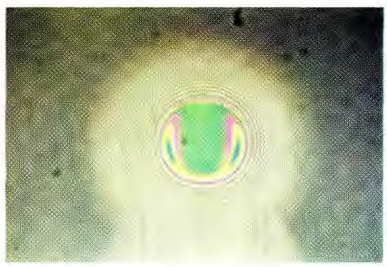
| Plate | Fluid | $\mu_0$ cP | Load lb | Speed R.P.M. |
|---|---|---|---|---|
| **Speed series** | | | | |
| A | 5-phenyl-4-ether | 2000 | 5 | 4 |
| B | " | 2000 | 5 | 7.5 |
| C | " | 2000 | 5 | 10 |
| **Fluid Comparison series** | | | | |
| A | 5-phenyl-4-ether | 2000 | 5 | 4 |
| D | 10 Bitetramethyloctyl + 8% Acryloid | 265 | 5 | 199 |
| G | 7 Bitetramethyloctyl | 40 | 5 | 390 |
| J | 17 Perhydrophenanthrene | 7.6 | 5 | 4000 |
| E | Calibration rings using a chromed lens of 12.6 cm radius of curvature. | | | |
| **Load series** | | | | |
| H | 5 Polyisobutylene oil | 59 | $\frac{1}{2}$ | 425 |
| K | " " | 59 | 1 | 425 |
| F | " " | 59 | 2.5 | 425 |
| I | " " | 59 | 5 | 425 |
| L | " " | 59 | 10 | 425 |



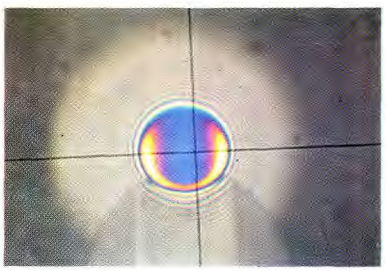
A



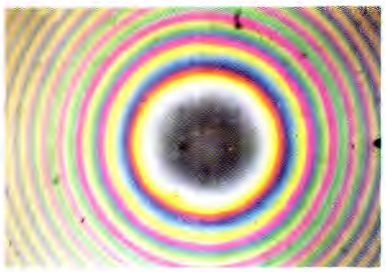
B



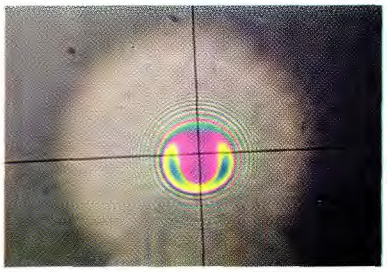
C



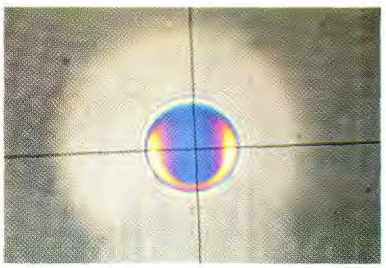
D



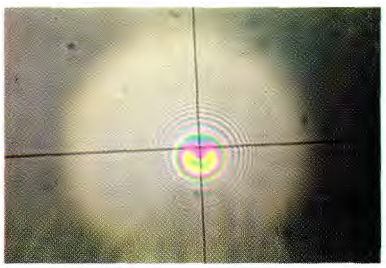
E



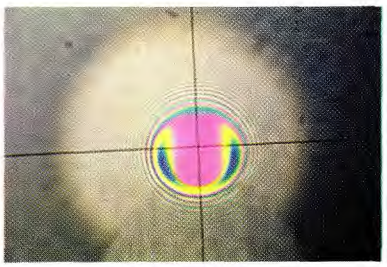
F



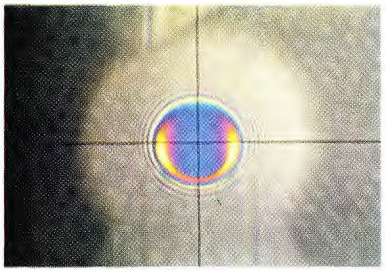
G



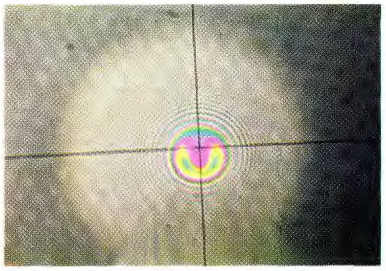
H



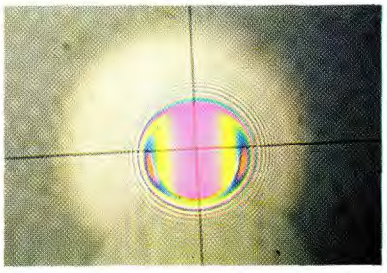
I



J



K



L

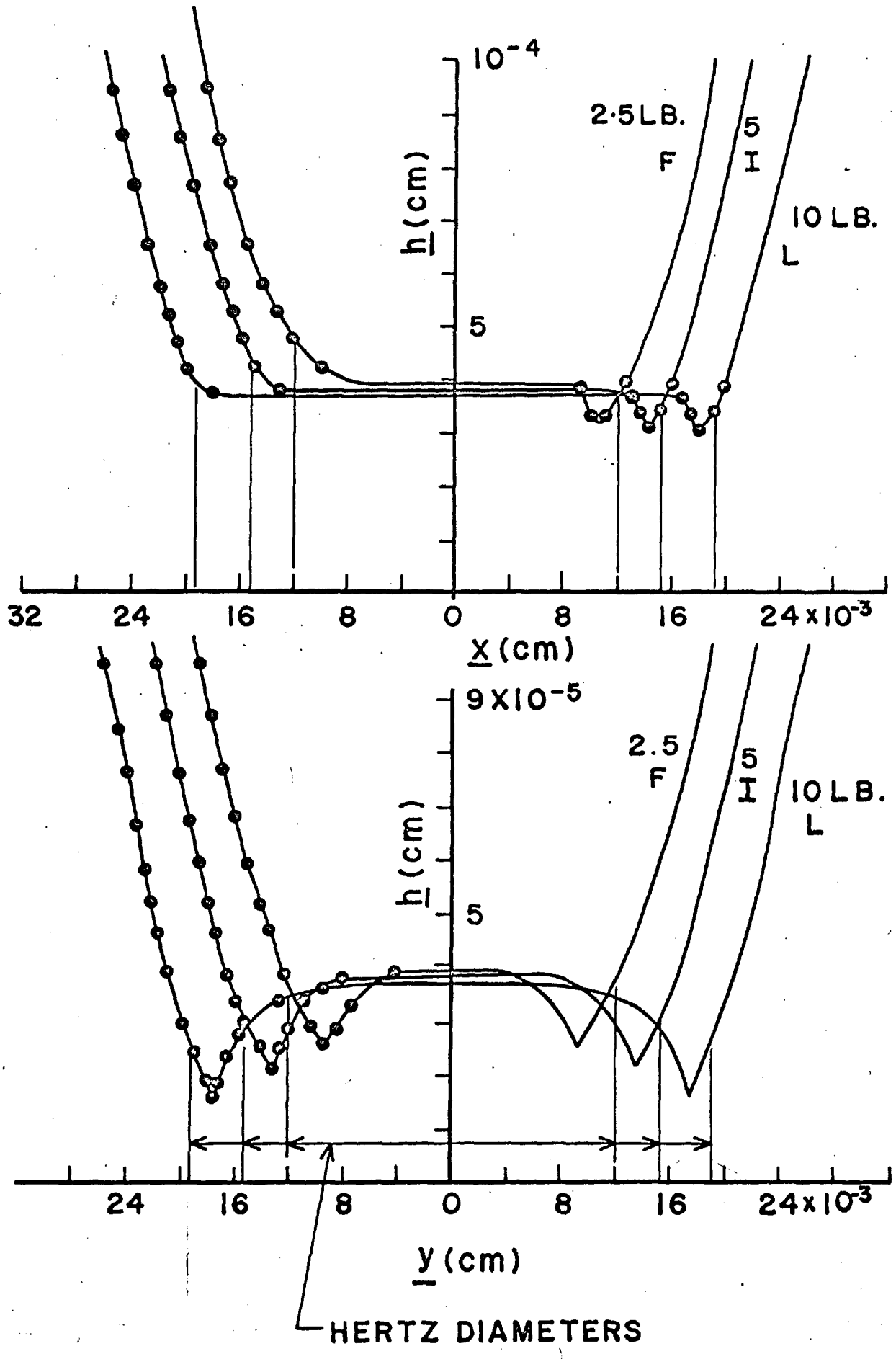



Fig.21. Oil Film Profiles at Different Loads.

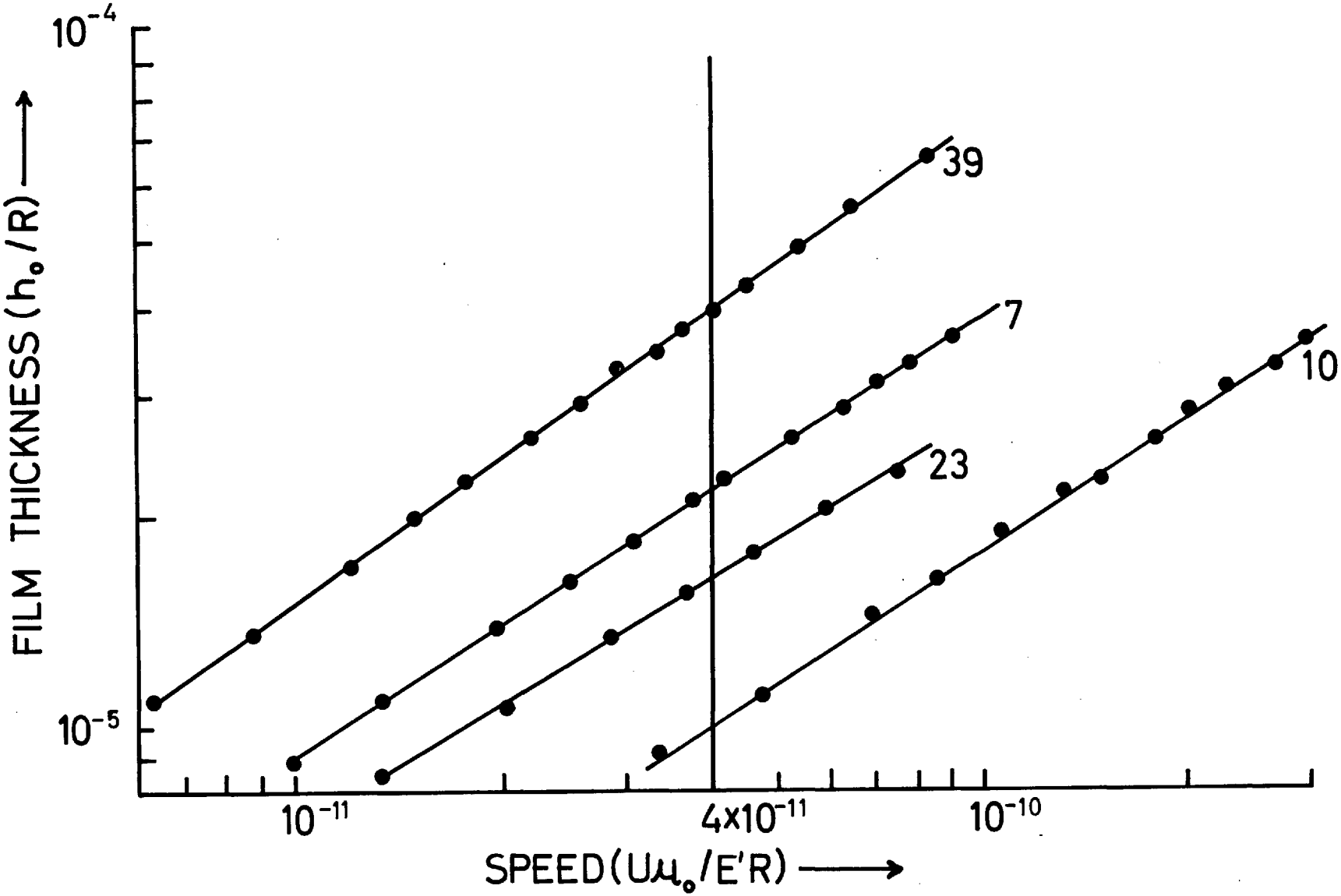



Fig. 22 Dimensionless film thickness for different fluids

Table 1

Fluid Properties and Test Results

| No. | Fluid description | Viscosity at t $\mu_o$ (cP) | Test temp. t (F) | ASTM Slope | Density at 77 F gm/ml | Refractive index at 77 F $n_o$ | $\frac{h_o}{R}_4$ | Slope a | $\alpha_r$ $(psi)^{-1}$ | Shear rate $(sec)^{-1}$ |
|---|---|---|---|---|---|---|---|---|---|---|
| | **Paraffinic Oils** | | | | | | | | | |
| 1 | A synthetic paraffin | 878 * | 74 | 0.53 | 0.840 | 1.48 | 1.65 x $10^{-5}$ | 0.70 | 0.92 x $10^{-4}$ | 0.25 x $10^{6}$ |
| 2 | Oil 1 + a high molecular weight reactive additive | 878 * | 74 | 0.53 | 0.840 | 1.48 | 1.65 | 0.70 | 0.92 | 0.25 |
| 3 | Squalene | 15.1 | 71.5 | 0.65 | 0.885 | 1.494 | 1.44 | 0.57 | 0.73 | 15. |
| 4 | Squalane | 30.2 | 71.5 | 0.73 | 0.808 | 1.450 | 1.71 | 0.58 | 0.98 | 5. |
| 5 | Polyisobutylene oil | 58.9 | 76 | 0.80 | 0.824 | 1.458 | 2.48 | 0.66 | 1.83 | 2. |
| 6 | Oil 5 + 5% Polymethacrylate | 82.4 | 76 | 0.73 | 0.829 | 1.460 | 2.16 | 0.65 | 1.46 | 2. |
| 7 | Bitetramethyloctyl[a] | 40.4 | 75 | 0.82 | 0.814 | 1.455 | 2.14 | 0.62 | 1.43 | 3.5 |
| 8 | Oil 7 + 1% Polymethacrylate | 51.7 | 75 | - | 0.814 | 1.455 | 1.89 | 0.62 | 1.15 | 3.5 |
| 9 | Oil 7 + 3% Polymethacrylate | 87.2 | 75 | - | 0.814 | 1.455 | 1.50 | 0.62 | 0.79 | 2.5 |
| 10 | Oil 7 + 8% Polymethacrylate | 264.6 | 75 | - | 0.82 | 1.456 | 0.97 | 0.62 | 0.39 | 1.5 |
| 11 | High VI petroleum oil | 342 | 77 | 0.68 | 0.887 | 1.493 | 2.20 | 0.63 | 1.48 | .5 |
| | **Naphthenic Oils** | | | | | | | | | |
| 12 | A highly refined naphthenic mineral oil | 160 | 74.5 | 0.72 | 0.889 | 1.48 | 2.19 | 0.69 | 1.48 | 1 |
| 13 | Oil 12 + 2.25% Heavy resin | 175 | 74 | 0.72 | 0.89 | 1.48 | 2.17 | 0.69 | 1.47 | 0.9 |
| 14 | Oil 12 + 5.5% Heavy resin | 204 | 74 | 0.72 | 0.89 | 1.48 | 2.13 | 0.69 | 1.41 | 0.8 |
| 15 | Oil 12 + 8.75% Heavy resin | 268 | 74 | 0.72 | 0.89 | 1.48 | 1.92 | 0.70 | 1.22 | 0.7 |
| 16 | Oil 12 + 14% Medium resin | 270 | 74 | 0.725 | 0.89 | 1.48 | 1.95 | 0.70 | 1.24 | 0.7 |
| 17 | Oil 12 + 14.7% Heavy resin | 351 | 74 | 0.71 | 0.89 | 1.48 | 1.97 | 0.70 | 1.25 | 0.5 |
| 18 | Isopropylbicyclohexyl | 8.46 | 77 | 0.89 | 0.881 | 1.48 | 1.77 | 0.56 | 1.04 | 20. |
| 19 | Hydrogenated polyphenyls | 76.2 | 77 | 1.00 | 0.938 | 1.5036 | 2.77 | 0.66 | 2.18 | 1.5 |
| 20 | Oil 13 + 1% Polymethacrylate | 119 | 77 | 0.88 | 0.942 | 1.5032 | 2.19 | 0.66 | 1.47 | 1 |
| 21 | Oil 13 + 3% Polymethacrylate | 229 | 77 | 0.74 | 0.943 | 1.5030 | 1.52 | 0.64 | 0.81 | 1 |
| 22 | Oil 13 + 8% Polymethacrylate | 631 | 77 | 0.58 | 0.944 | 1.5012 | 1.04 | 0.61 | 0.48 | 0.5 |
| 23 | Perhydrophenanthrene | 7.64 | 72 | 0.76 | 0.943 | 1.530 | 1.59 | 0.58 | 0.88 | 25 |
| 24 | Perhydrofluoranthene | 20.8 | 72 | 0.79 | 0.990 | 1.524 | 1.82 | 0.57 | 1.09 | 10 |
| | **Aromatic Oils** | | | | | | | | | |
| 25 | Low VI petroleum oil | 470 | 77 | 0.87 | 0.942 | 1.524 | 3.01 | 0.69 | 2.50 | 0.25 |
| 26 | Isopropylbiphenyl | 6.94 | 77 | 0.95 | 0.982 | 1.582 | 1.38 | 0.55 | 0.64 | 40 |
| 27 | Polyphenyl eutectic | 52.2 | 77 | 1.18 | 1.069 | 1.640 | 2.81 | 0.62 | 2.22 | 2.5 |
| | **Ethers** | | | | | | | | | |
| 28 | 1,3-Dicyclohexyloxycyclohexane | 74.4 | 77 | 0.85 | 0.982 | 1.486 | 2.44 | 0.64 | 1.78 | 2 |
| 29 | m-Diphenoxybenzene | 24.7 | 77 | 0.85 | 1.14 | 1.607 | 1.71 | 0.57 | 0.98 | 7.5 |
| 30 | 4-Phenyl-3-ether | 202 | 76 | 0.87 | 1.174 | 1.62 | 2.50 | 0.66 | 1.85 | 0.5 |
| 31 | 5-Phenyl-4-ether | 1950 | 77 | 0.90 | 1.19 | 1.63 | 4.02 | 0.66 | 4.00 | 0.09 |
| 32 | C-Ether MCS-277[b] | 26 | 74.5 | 0.76 | 1.194 | 1.68 | 1.61 | 0.62 | 0.88 | 9. |
| 33 | Oil 32 + 3% 6-Phenyl-5-ether | 28.6 | 74.5 | - | 1.194 | 1.68 | 1.66 | 0.63 | 0.94 | 8 |
| 34 | Oil 32 + 5% 6-Phenyl-5-ether | 30.5 | 74.5 | - | 1.194 | 1.68 | 1.72 | 0.64 | 0.97 | 7 |
| 35 | Oil 32 + 10% 6-Phenyl-5-ether | 35.3 | 74.5 | - | 1.195 | 1.68 | 1.80 | 0.64 | 1.05 | 6 |
| 36 | C-Ether MCS-293[b] | 62.3* | 74 | 0.82 | 1.198 | 1.68 | 2.0 | 0.68 | 1.25 | 3 |
| | **Esters** | | | | | | | | | |
| 37 | Pentaerythritol tetravalerate | 27.1 | 77 | 0.75 | 1.015 | 1.447 | 1.44 | 0.57 | 0.73 | 7.5 |
| 38 | Oil 27 + 5% Polymethacrylate | 75.6 | 77 | 0.45 | 1.016 | 1.449 | 0.92 | 0.61 | 0.35 | 4.5 |
| | **Fluorocarbons** | | | | | | | | | |
| 39 | PR-143AB[c] | 226 * | 76 | 0.66 | 1.88 | 1.30 | 3.90 | 0.70 | 3.70 | 0.4 |
| 40 | PR-143AC[c] | 1175 * | 74 | 0.58 | 1.89 | 1.30 | 2.62 | 0.70 | 1.99 | 0.1 |
| | **Silicones** | | | | | | | | | |
| 41 | Chlorophenylmethyl silicone | 76.4* | 74 | 0.37 | 1.04 | 1.425 | 1.50 | 0.67 | 0.78 | 3 |
| 42 | Trifluoropropylhalophenyl silicone | 160 * | 75.5 | 0.28 | 1.07 | 1.416 | 1.29 | 0.64 | 0.61 | 1.5 |
| 43 | Trifluoropropylmethyl silicone | 125 * | 75 | 0.53 | 1.21 | 1.378 | 1.91 | 0.67 | 1.18 | 1.5 |
| 44 | Alkylated silicone | 79.4* | 74.5 | 0.40 | 0.911 | 1.438 | 1.38 | 0.67 | 0.64 | 3.5 |
| | **Vegetable Oils** | | | | | | | | | |
| 45 | Castor Oil | 720 | 77 | 0.72 | 0.955 | 1.482 | 1.83 | 0.62 | 1.09 | 0.25 |
| 46 | Rape Oil | 69.3 | 77 | - | 0.912 | 1.476 | 1.57 | 0.59 | 0.87 | 3.5 |

* These viscosities were obtained by extrapolation from measurements at other temperatures, the rest were measured on the test sample at the test temperature

[a] See Reference (91)

[b] See Reference (92)

[c] See Reference (93)

are for the same oil at the same speed with loads of 0.5, 1, 2.5, 5 and 10 lb loads. Profiles corresponding to some of these are plotted in Fig.21. The increasing load causes hardly any decrease in the thickness of the main central part of the film but increases the contact area greatly. This result is in accord with the conjectures of Grubin (22) and the one-dimensional theory of Dowson and Higginson (11). The large reduction of the thickness in the side lobes of the film with increasing load is of interest because it may account for the fact that X-ray measurements give a greater reduction of film thickness with load $\frac{h}{R} \propto W^{-0.36}$ (43) than theory or capacitance measurements $\frac{h}{R} \propto W^{-0.13}$.

The dimensionless plots Fig. 23 which correspond to the conditions in Fig. 20 H,K,F,I,L also show the small effect of load on central film thickness as do the top two curves in Fig. 24 which show the central film thickness of a 5-phenyl-4-ether lubricated contact over a wide speed range at 5 and 10 lb loads.

The black and white photographs Fig. 25 and cross sections Fig. 26 show the shapes corresponding to certain points on Fig. 24. A point of interest is that the film thickness at the back of the contact, which under high speed conditions is the minimum, is nearly independant of load. These photographs also show, as do the coloured ones, that the minimum film thickness moves from the back of the contact to the side lobes as load is increased at constant speed, although at the highest speed (giving 30th black fringe) it was not possible to increase the load sufficiently for this to happen, within the limits of the apparatus.

7.3 The Effect of a Wide Speed Range

The results of the tests over a wide speed range (3 decades) are shown in Fig. 24. The curves for rolling with the polyphenyl ether which is a very thick fluid of nearly 2000 cp viscosity, begin to deviate from

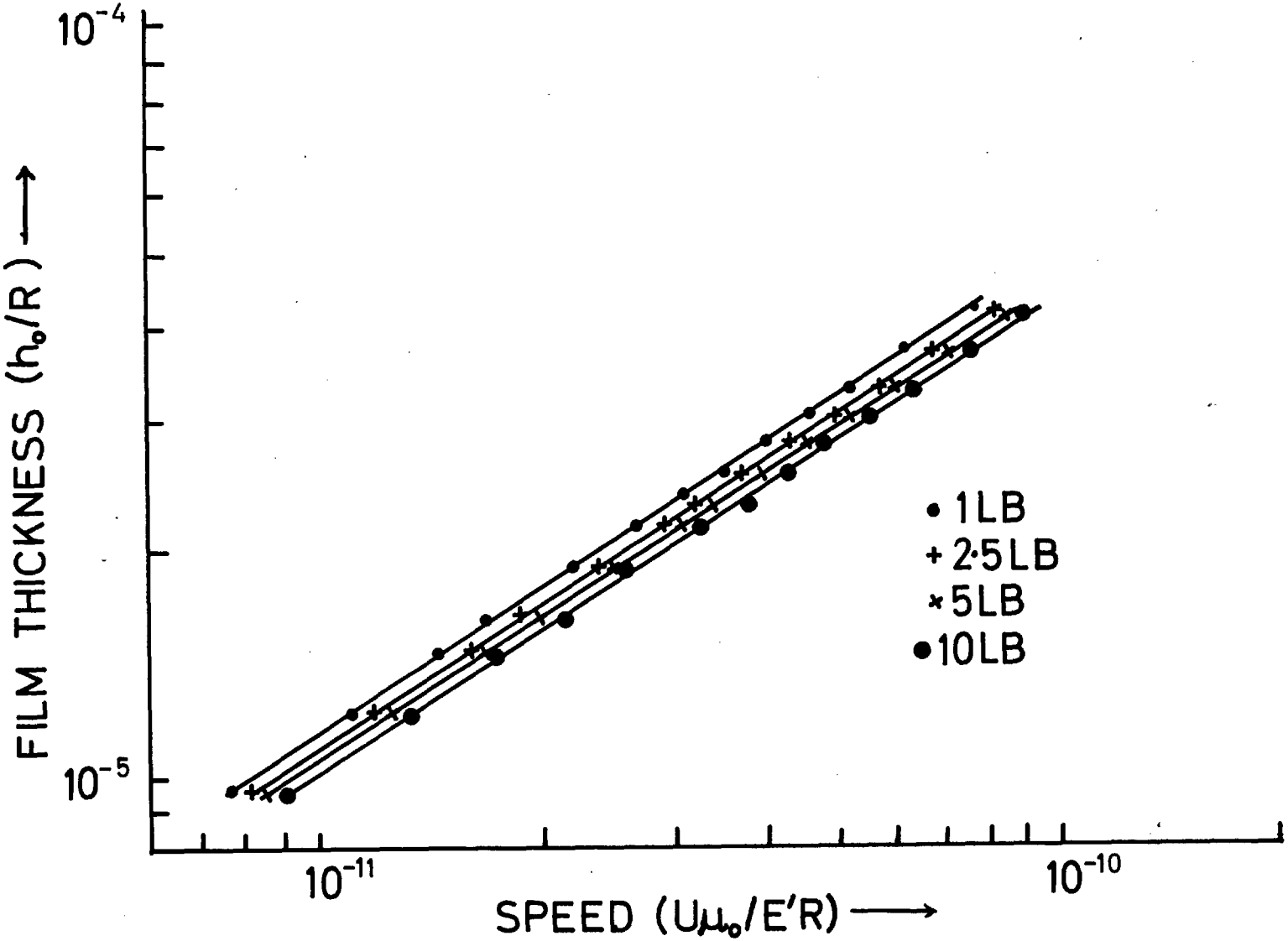



Fig. 23 Dimensionless film thickness at different loads for oil 5

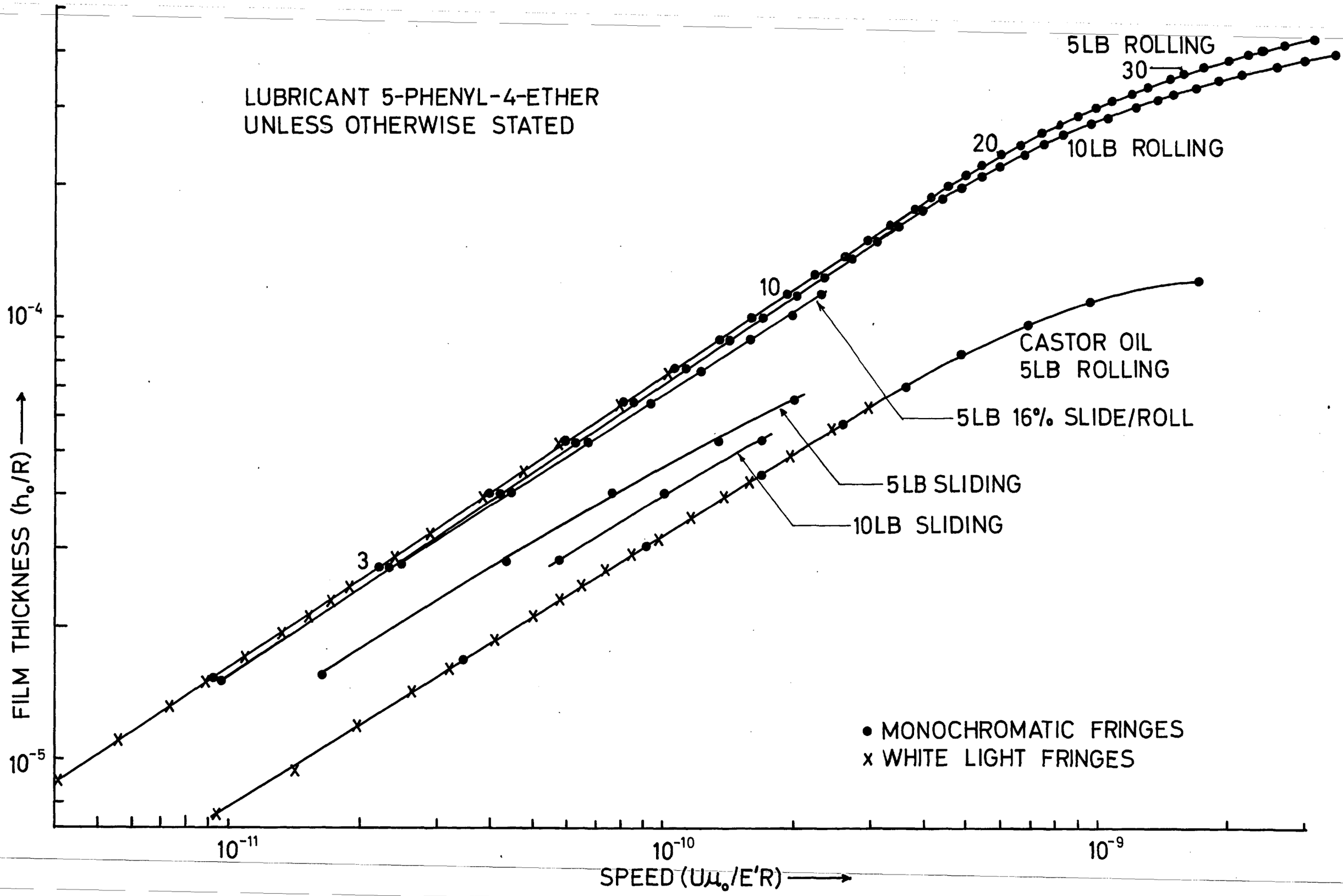
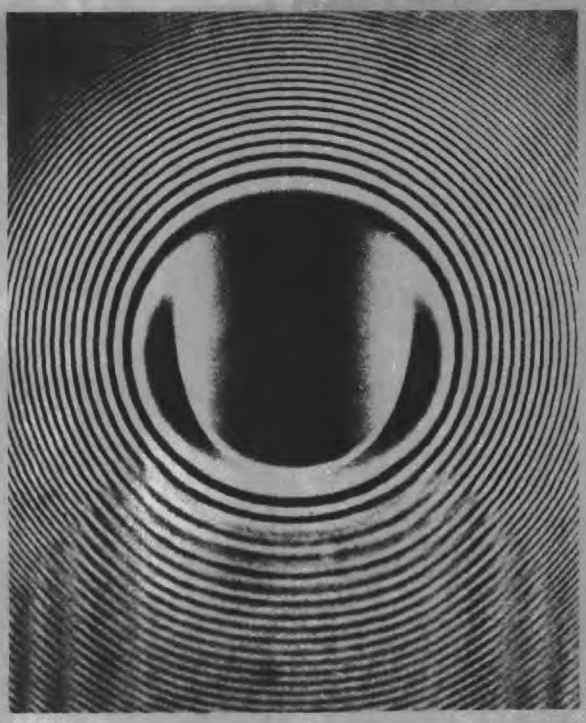
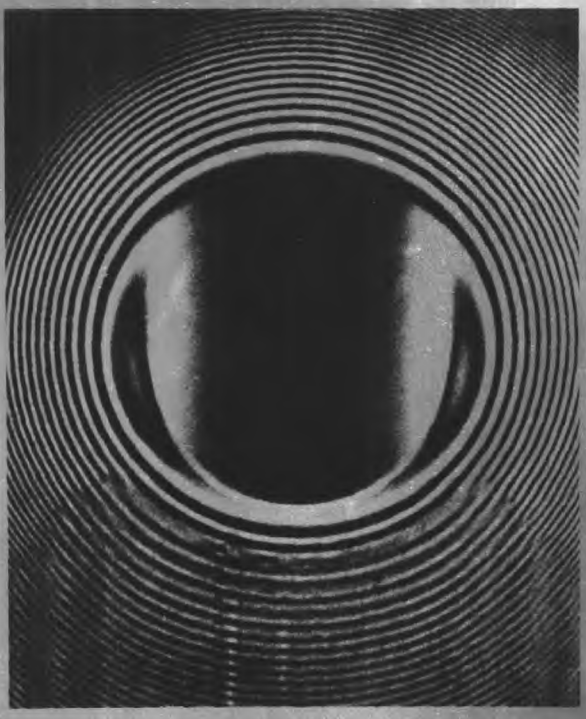



FIG 24 FILM THICKNESS FOR A WIDE RANGE OF CONDITIONS



a) 5LB 3$^{RD}$ BLACK



b) 10LB 3$^{RD}$ BLACK

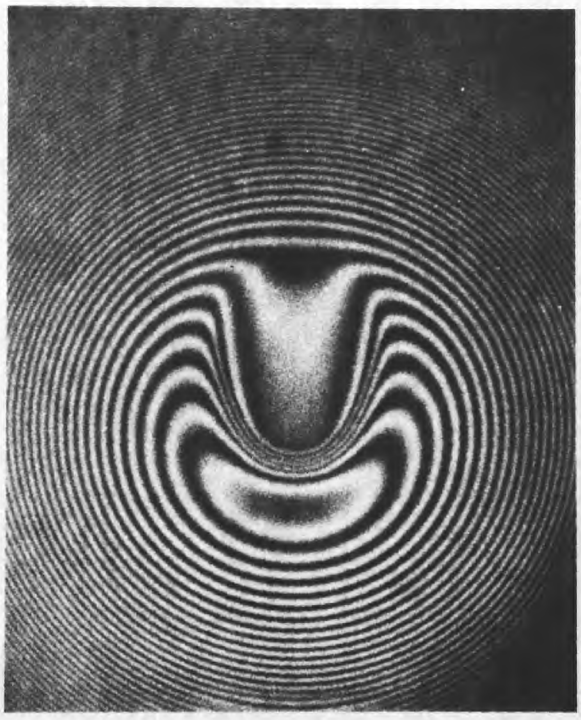


c) 5LB 10$^{TH}$ BLACK



d) 10LB 10$^{TH}$ BLACK

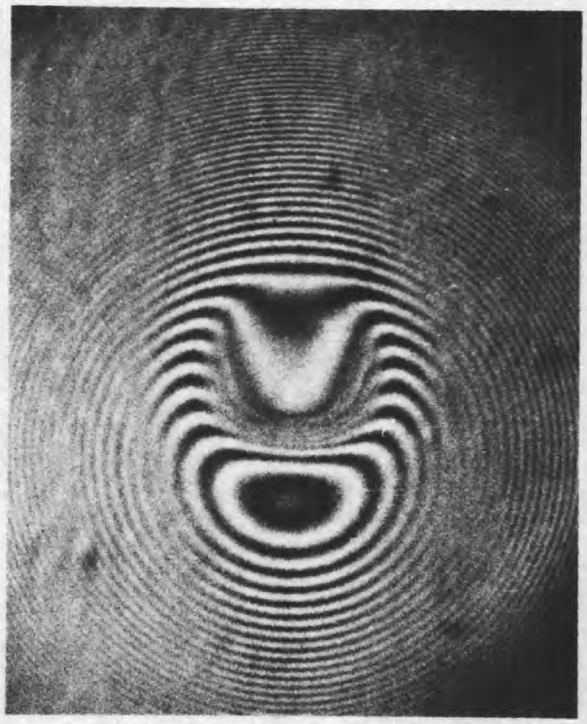
FIG 25 ROLLING CONTACTS LUBRICATED WITH 5-PHENYL-4-ETHER



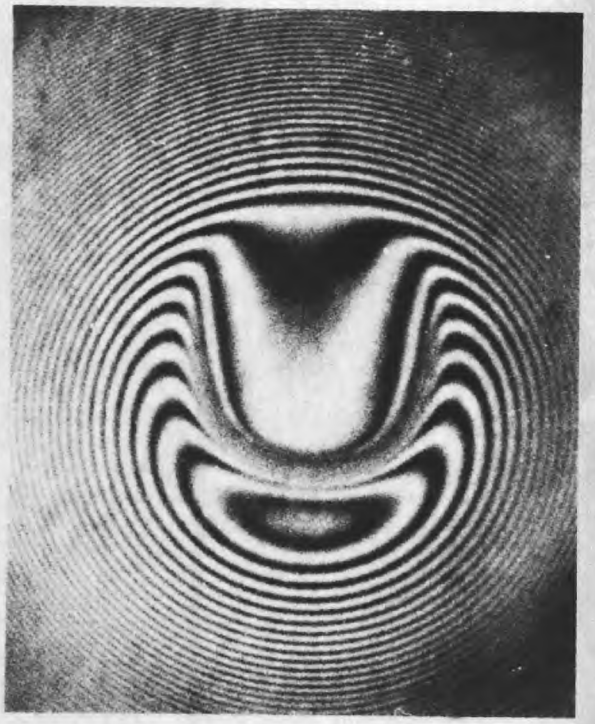
e) 5LB 20TH BLACK



f) 10LB 20TH BLACK



g) 5LB 30TH BLACK



h) 10LB 30TH BLACK

FIG 25 (cont)

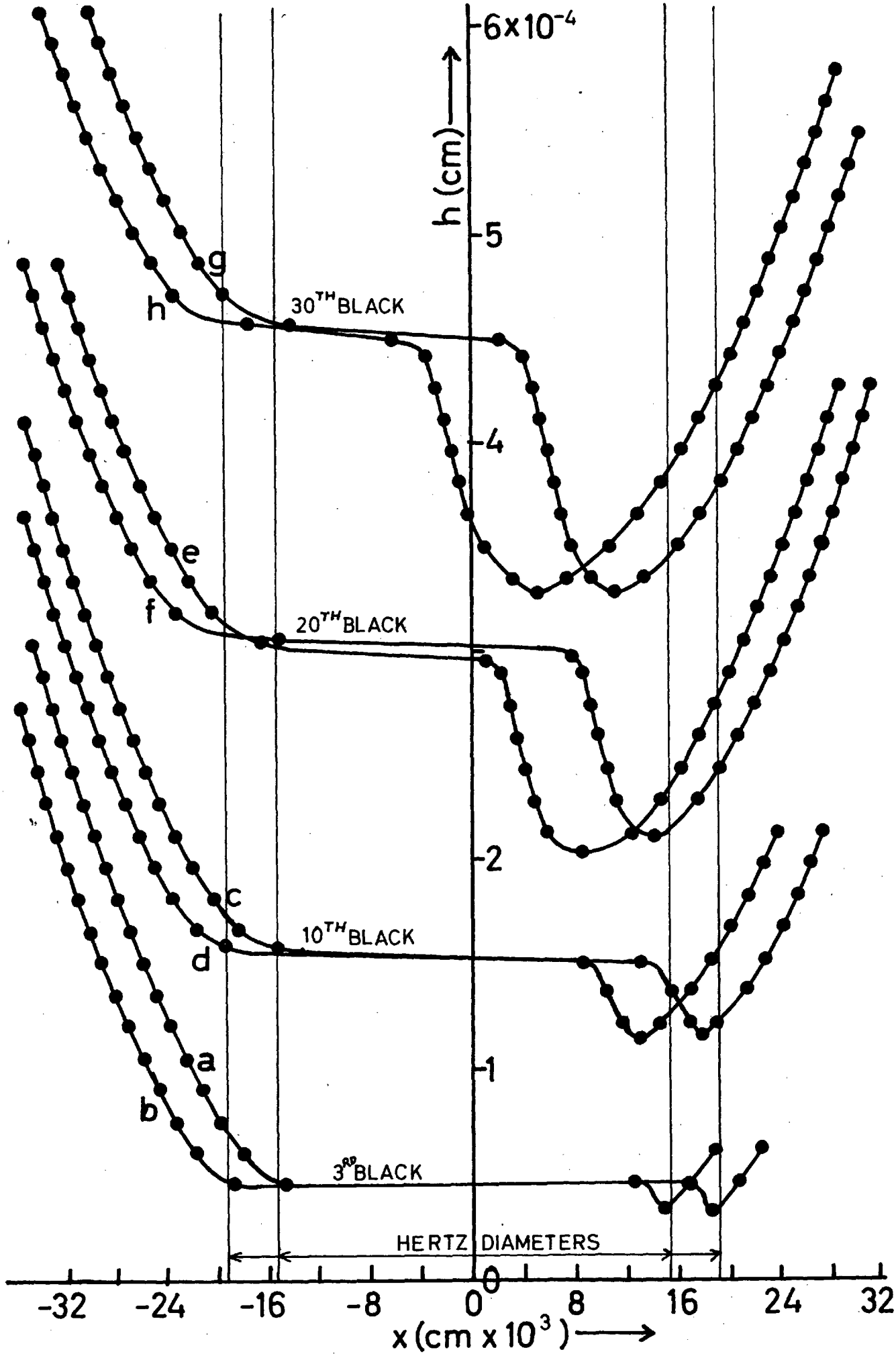



Fig. 26 Profiles in rolling (cf Fig. 25)

a straight line at about the 20th fringe point although no appreciable temperature rise was noted until after the 30th fringe. This deviation may be due to viscoelastic behaviour, or due to a temperature rise in the contact region which cannot be measured in the present apparatus, and might be significant in view of the very strong dependance of viscosity on temperature for this lubricant at room temperature. As, in all other tests deviation from a straight line has been associated with a change in temperature which can be detected, the author suspects that non-Newtonian behaviour may be significant in this case. The castor oil curve starts to deviate slightly from the straight line around 7th black and curves much more rapidly after 9th black when the temperature rises appreciably.

The photographs Fig. 25 show the film shapes at 5 and 10 lbs loads at the 3rd, 10th, 20th, and 30th black points, which are marked on Fig. 24. They show that at constant load the point of minimum film thickness moves from the side lobes to the back as speed increases; with a 5 lb load this occurs at the 15th black fringe and with a 10 lb load at the 21st black fringe. Profiles in the direction of rolling ( x co-ordinate) are plotted in Fig. 26 for the conditions of Fig. 25. Because of the difficulty of estimating the pressure distribution and therefore the refractive index change in the thicker film cases, all the profiles of Fig. 26 are plotted using the refractive index at atmospheric pressure. The increase in density of this fluid at the maximum Hertz pressure of 66,000 p.s.i. is 16% which gives a refractive index increase of 10%. As the density increase of most fluids, except silicones and fluorocarbons, levels off at about this value at high pressures (60), it is unlikely that refractive index change will be greater than 10% even in the region of any pressure spike. After making full allowance for this change the constriction at the back of the

contact is always greater than 20% of the film thickness. The viscious constriction must impose very severe stresses on the material, which implies that beyond a certain value an increase in film thickness may do more harm than good.

7.4 Sliding and Friction

The results of the sliding tests in which the disc is held stationary against the rotating ball are given in Fig. 24. The thicknesses at the same dimensionless speed parameter are considerably lower than rolling values, being even lower in the 10 lb than the 5 lb case. These results are almost certainly due to viscous heating in the inlet sweep; this heating made it much more difficult to obtain repeatable results in sliding than in rolling. The results of the angled drive 16% slide : roll tests show only a slightly thinner film than pure rolling because the viscous heating effect is relatively small. Repeatable results are easier to obtain than in the 100% sliding case, partly because there is less heating but also because the rotation of the disc means that the contact is always fed entirely with fresh cool oil, whereas when the disc is stationary the contact receives a mixture of warm oil from the disc and fresh oil from the ball.

The photographs in Fig. 27 and profiles in Fig. 28 show the shape of the oil films in 100% sliding. The main difference is that in sliding the entry to the Hertzian flat is more gently curved than the rolling case. The constrictions are almost identical in the two cases.

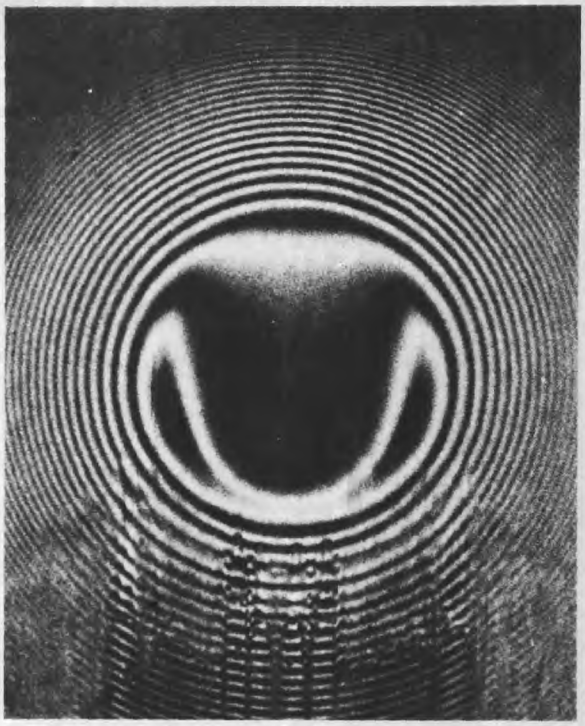
In pure rolling it is assumed that the individual deformations of the ball and disc are in the ratio of their reduced Young's modulii (ie. glass being deformed 2.73 times as much as steel) but in sliding the surface shear stress, which must integrate up to give a traction of about 10% of the normal load, acts in opposite directions on the two bodies which means that each must be deformed differently.

The photograph Fig. 30 is of the 16% slide roll angled contact. The ruled black line shows the direction of the rolling vector. An investigation using the original negative shows that the inlet zone of the contact is symmetrical about this vector but the rear constriction is displaced to one side. This displacement is in the direction in which the sliding vector acts on the glass, and shows that glass is deformed more than the steel, which is as expected.

The coefficients of friction in 100% sliding are plotted against speed and load in Fig. 29 a and b. The values of about 0.1 are higher than those usually expected for sliding point contact, but is probably because of the very high viscosity and pressure-viscosity coefficient $\alpha_r$ of the 5-phenyl-4-ether lubricant. The temperature in the contact which is a very important factor in friction determination (37) could not be measured accurately which means that any detailed discussion of the curves in Fig. 29 would be pointless, however they do show that the coefficient of friction decreases with speed which is as expected because increasing the speed causes an increase in temperature which reduces the viscosity of the oil in the film. The coefficient also starts to increase with increasing load but then falls off. A simple isothermal analysis predicts an increasing coefficient with increasing load but as the load increases temperature effects which act to reduce the coefficient become dominant. Another point is that the rolling component of friction which acts in opposition to the sliding and is generally small, will be more significant at low loads.

## 7.5 Film Rupture

The last point on each curve of Figs. 26 and 28 indicates the approximate position of film rupture and commencement of the wake except for the 20th and 30th fringe rolling cases where no wake occurs. The reason for the point of rupture moving further downstream as thickness increases must be



a) 5LB 3RD BLACK



b) 10LB 3RD BLACK

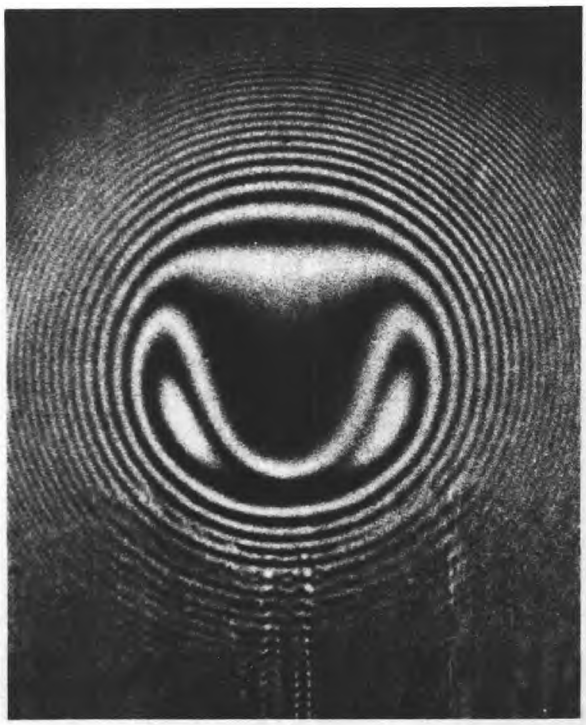


c) 5LB 4TH BLACK



d) 10LB 4TH BLACK

FIG 27 SLIDING CONTACTS LUBRICATED WITH 5-PHENYL-4-ETHER



e) 5LB 5$^{TH}$BLACK



f) 10LB 5$^{TH}$BLACK



g) 5LB 6$^{TH}$BLACK

FIG 27 (cont.)

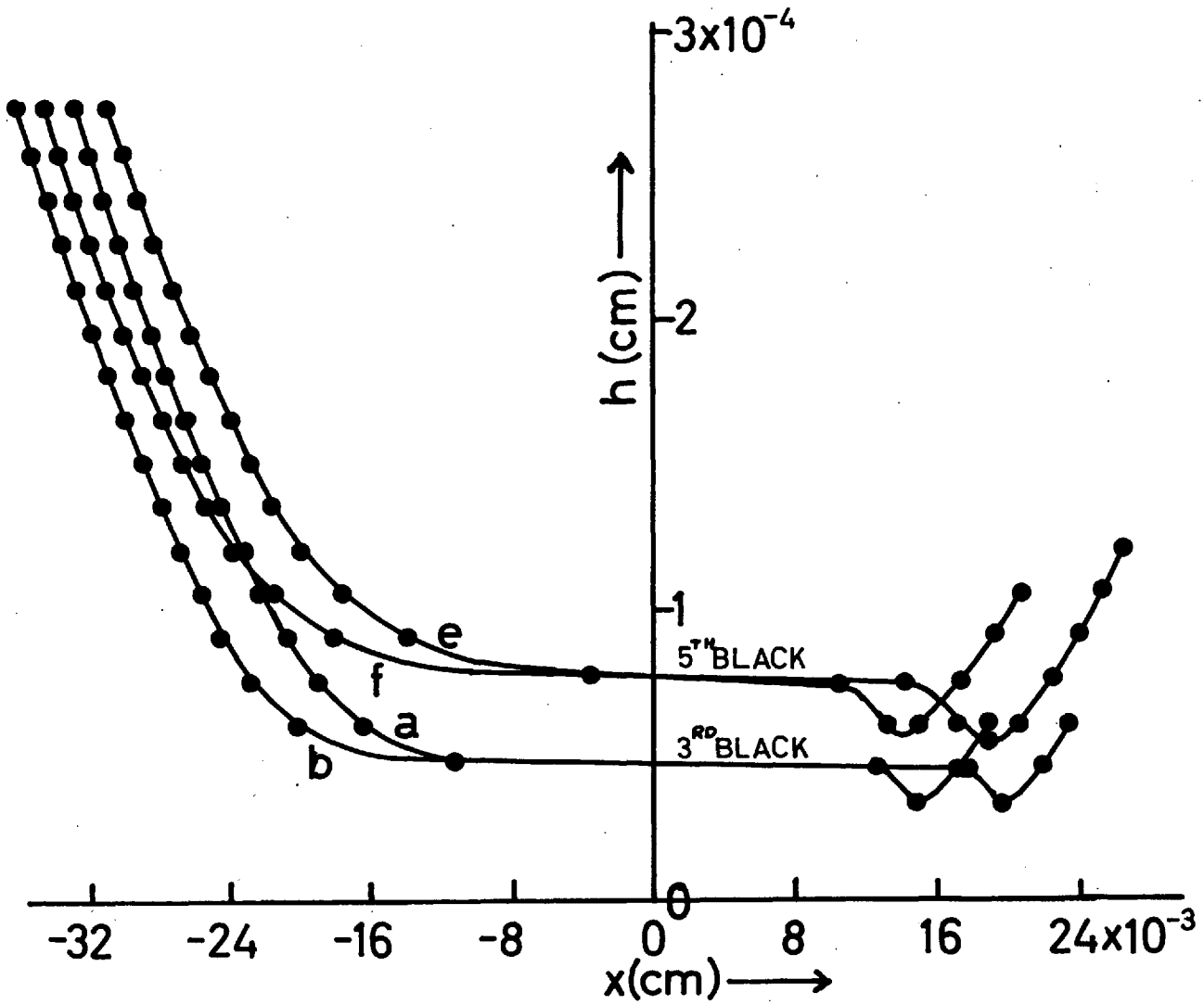



Fig. 28 Profiles in sliding (cf Fig. 27)

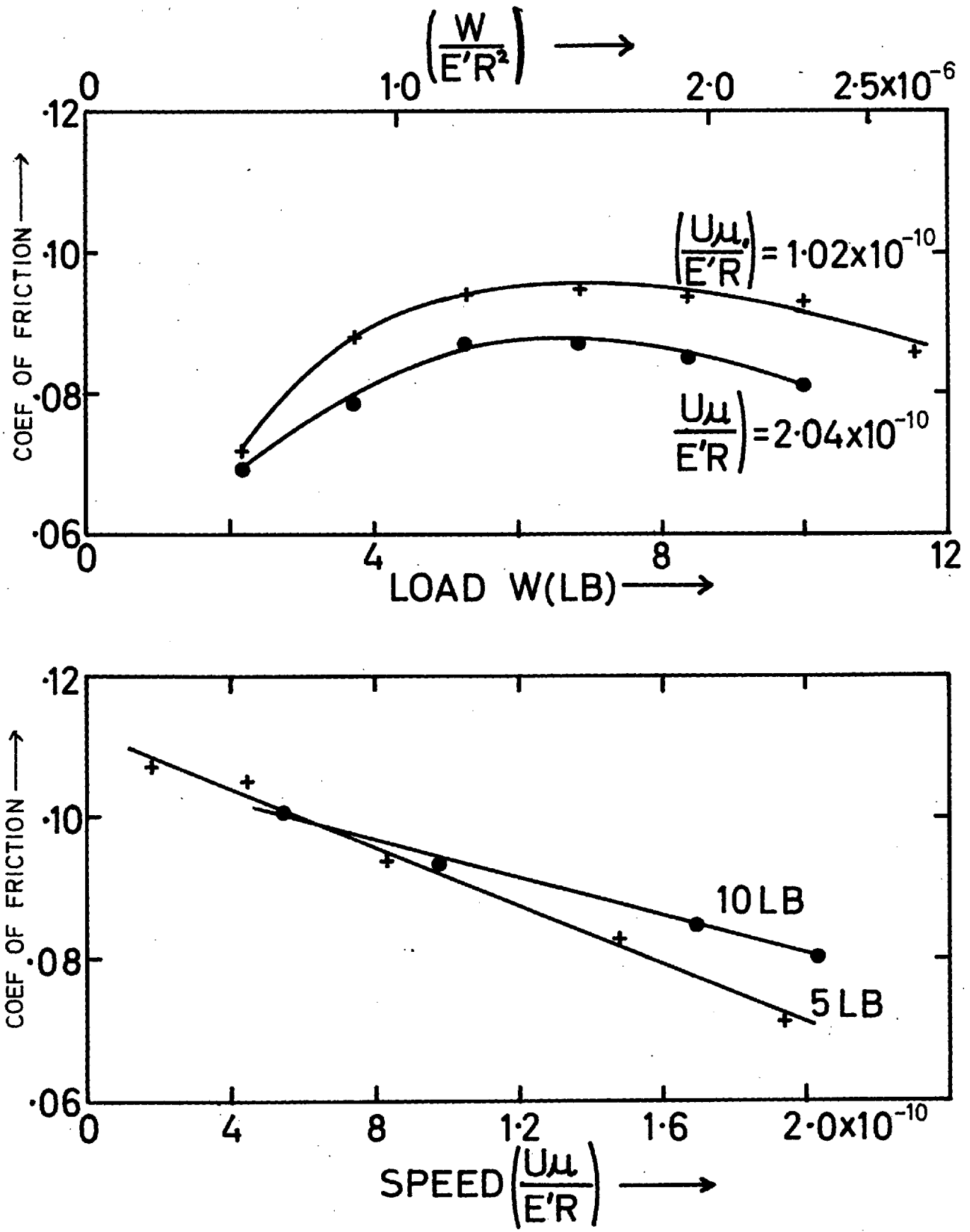



Fig. 29 Friction behaviour of 5-phenyl-4-ether in 100% sliding



Fig. 30 Angled drive

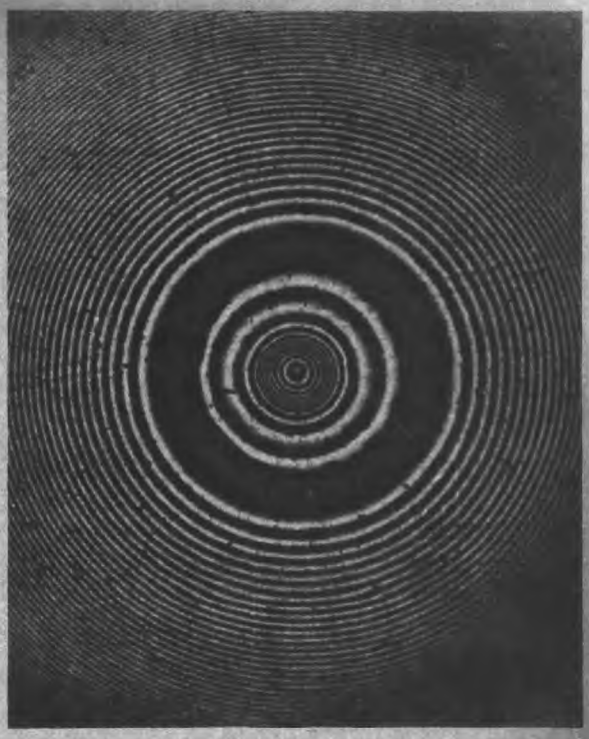


Fig. 31 Squeeze film

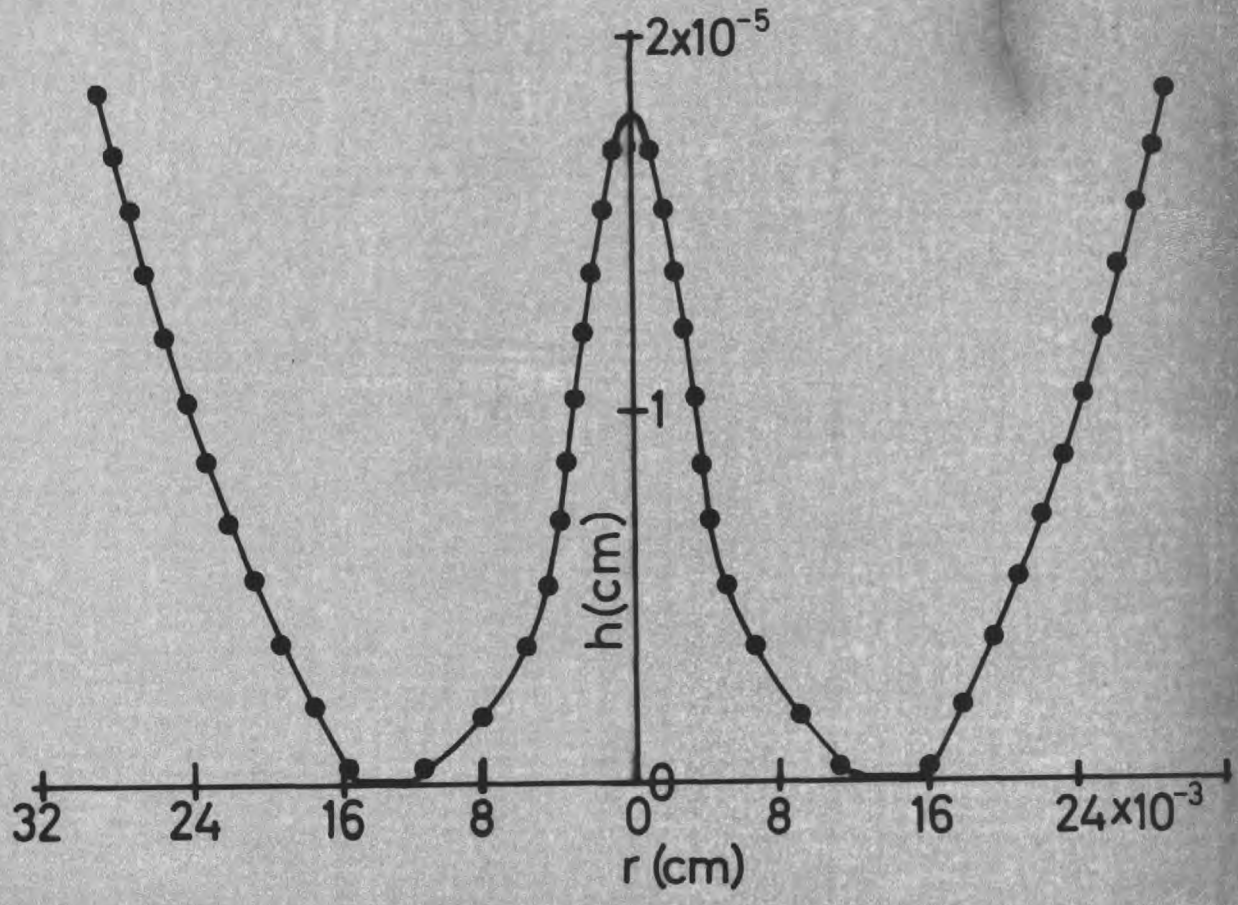



Fig. 32 Cross section of squeeze film

that $\frac{1}{h^3} \frac{\partial h}{\partial x}$ which is a major term in the Reynolds' pressure equation, becomes smaller with increasing $h_o$ thus allowing the pressure to decrease more slowly, and therefore reach the subatmospheric value required to cause rupture at a later point.

The film rupture at the end of the contact is often called cavitation which though a convenient term is best reserved for the phenomenon in which bubbles of air or vapour at sub-atmospheric pressure are generated within the fluid. The bubbles subsequently collapse causing damage. In the film rupture the oil film breaks into streamers, the voids between the streamers being in communication with the atmosphere. There is no question of damage from the film rupture, except that in a ball-race each ball will be rolling in the wake left by the previous one and may be left short of lubricant, especially if the oil is one with poor wetting characteristics.

An area of lubricant starvation can be seen in the inlet of Fig. 20 J which is of an 8 centipoise fluid at 4000 RPM. If the lubricant shortage becomes more acute the starvation area extends into the contact and the film breaks down causing scratching.

Cavitation in the more rigidly defined sense may occur but the movement of the bubbles would be so rapid as to make them invisible under these conditions. A number of so called lubrication-failures in high pressure hydraulic control valves have been found in fact to be due to cavitation errosion which can be cured by suitable modifications to the hydraulic fluid.

## 7.6 Squeeze Film

The photograph Fig. 31 and cross section Fig. 32 show a squeeze film dimple achieved by loading the ball suddenly against the disc which was coated with 5-phenyl-4-ether lubricant, oil 31. This lubricant produces a bigger and more persistant dimple than others of similar viscosity, this may be because of its very high pressure viscosity coefficient $\alpha_r$, but its high surface tension and poor wetting characteristics on steel and

chromium may also play a part, because after loading, some of the fluid can be observed to flow outwards from the parallel film and some into the dimple. The parallel annulus has an identical appearance in white light interference to a dry contact, which suggests that any fluid film present is extremely thin and certainly less than 200 Å, further evidence of this is that the dimple will remain virtually unchanged for 9 hrs. The air supply used for loading is not available at night which prevents a longer test at present. Most lubricants leak out of the dimple after a few hours. A more detailed study of this phenomenon has been carried out by Dowson (82).

## CHAPTER 8 INTERPRETATION OF FLUID TESTS

### 8.1 High Shear Rate High Pressure Viscometry

The full theory for oil film formation in line contact gives:

$$\left(\frac{h_o}{R}\right) \propto \left(\frac{\mu_o U}{E'R}\right)^{a} \left(\frac{W}{E'RL}\right)^{b} \quad (\propto E')^{c}$$

where a = 0.7, b = -0.13 and c = 0.6.

In Fig. 22 the dimensionless film thickness $\frac{h_o}{R}$ at constant load is plotted against $(\mu_o U/E'R)$ for a few fluids; similar graphs were plotted for all the fluids and the information obtained is specified in Table 1 by giving 'a' the slope of the line, and $\left(\frac{h_o}{R}\right)_4$ which is the value of $\left(\frac{h_o}{R}\right)$ at $(\mu_o U/E'R) = 4 \times 10^{-11}$. This value of $(\mu_o U/E'R)$ is chosen as a reference because it lies conveniently within the test range of all the fluids. The separation between the lines (difference in $\left(\frac{h_o}{R}\right)_4$) can to a first order be ascribed to difference in $\alpha$. If this was the entire reason, then all the lines would have the same slope 'a', and their separations would be proportional to $(\alpha E')^c$. The points of Figs. 19 and 22 which show a scatter typical for most tests, define the slope to within 0.01, but in the case of thin fluids, such as No. 17, the error may be 0.02 because their low viscosities (under 10 centipoise) limit the test range. Most of the slopes are about 0.67, but for some of the thick fluids the value is 0.7 and for the thin fluids it is as low as 0.55. These differences are much greater than the experimental error.

The greatest slope 0.7 is the one most likely to agree with the full Newtonian EHL theory of point contact when obtained, and is the same as 'a' for line contact theory. This suggests that 'c', the index of $(\alpha E')$, will

also be nearly the same in the two cases, and if 'c' is assumed to be 0.6, it is possible to work out the relative pressure-viscosity coefficients of all the fluids tested, provided that differences in slope are neglected.

If one fluid is considered a standard, and the value of $(\mu_o U/E'R)$ equal to $4 \times 10^{-11}$ taken as the reference for comparison,

$$\frac{\left[\left(\frac{h_o}{R}\right)_4\right]_T}{\left[\left(\frac{h_o}{R}\right)_4\right]_S} = \frac{(\alpha E')_T}{(\alpha E')_S}^{0.6}$$

and

$$\alpha_T = \alpha_S \frac{\left[\left(\frac{h_o}{R}\right)_4\right]_T}{\left[\left(\frac{h_o}{R}\right)_4\right]_S}^{5/3},$$

where T signifies the test fluid and S the standard. The standard chosen is the oil D used by Dyson, Naylor and Wilson (41), a low viscosity-index mineral oil which is predominantly aromatic and napthenic. This oil was chosen because napthenic oils generally follow the exponential pressure-viscosity law (56), and also because its pressure-viscosity coefficient has been measured at temperatures of 100 C, 60 C and 30 C, so that extrapolation to the test temperature 25 C is fairly safe. The extrapolated value at 25 C is $3.63 \times 10^{-9}$ $cm^2$/dyne which is $2.50 \times 10^{-4}$ $(p.s.i.)^{-1}$. The relative coefficients $\alpha_r$ based on this standard are listed in Table 1. The coefficient $\alpha_r$ should be considered as a parameter relating the viscosity at high pressure and high shear to that at low pressure and low shear, and is valuable in that it indicates the relative effectiveness of different fluid types in promoting elastohydrodynamic films.

8.2 Comparison of $\alpha_r$ with other estimates of $\alpha$

To gain an insight into the other factors besides pressure viscosity which affect film thickness, it is necessary to have values of the pressure viscosity coefficients obtained by a technique such as capillary flow which is

independent of film thickness measurement. Unfortunately, few pressure-viscosity coefficients at 77 F and pressure up to 60,000 p.s.i. are available for comparison with the pressure-viscosity coefficients of Table 1. In the absence of such data the pressure and viscosity coefficient $\alpha_e$ at 100 F and 10,000 p.s.i. has been estimated by the method of Fresco (59) (which is based on ASTM slope and is limited to fluids with slopes between 0.6 and 1.07) for all those fluids for which the method is applicable. These values of $\alpha_e$ together with some measured values are listed in Table 2.

Inspection of Table 2 shows that the values of $\alpha_r$ and $\alpha_e$ for most of the fluids agree closely (within 30%). This close agreement tends to confirm the method used for calculating $\alpha_r$ and suggests that the effect of such factors as shear rate in lowering the pressure-viscosity coefficient is minor for most of the fluids in Table 1. The main exceptions are the polymer solutions which are discussed in section 8.5, a silicone (fluid 44), which is known to exhibit strong non-Newtonian behaviour, a synthetic paraffin (fluid 1), a fluorocarbon (fluid 40), and two aromatic compounds (fluids 26 and 29).

Other methods of predicting the pressure viscosity coefficient are those of Chu and Cameron (56) who give a chart for predicting C in their equation

$$\mu = \mu_o \quad (1 + Cp)^{16}$$

and Roelands (58) who defines a very complicated pressure viscosity index

$$Z = 0.74 + \left(\frac{800}{230 - C_r} - 4.40\right)(H_o - 0.1400)$$

where $H_o = \log(\log \mu_o + 1.200)$ with $\mu_o$ in centipoise, and $C_r$ is the percentage of a carbon in rings.

The Chu and Cameron (56) method is derived from measurements on

Table 2

Pressure-viscosity coefficients $\alpha_e$ estimated by Fresco's (59) method

| Fluid | $\alpha_r$ $(psi)^{-1}$ | $\alpha_e$ $(psi)^{-1}$ |
|---|---|---|
| 1 | $0.92 \times 10^{-4}$ | $1.27 \times 10^{-4}$ |
| 3 | 0.73 | 0.81 |
| 4 | 0.98 | 1.12 |
| 5 | 1.83 | 1.46 |
| 6 | 1.46 | 1.77 |
| 7 | 1.43 | 1.43 |
| 11 | 1.48 | 1.76+ |
| 12 | 1.48 | 1.43 |
| 13 | 1.47 | 1.49 |
| 14 | 1.41 | 1.51 |
| 15 | 1.22 | 1.55 |
| 16 | 1.24 | 1.56 |
| 17 | 1.25 | 1.61 |
| 18 | 1.04 | 1.15 |
| 19 | 2.18 | 1.91 |
| 20 | 1.47 | 1.75 |
| 21 | 0.81 | 1.59 |
| 22 | 0.48 | 1.43 |
| 23 | 0.88 | 0.78 |
| 24 | 1.09 | 1.12 |
| 25** | 2.50 | 2.20 |
| 26 | 0.64 | 1.17 |
| 27 | 2.22 | 2.19 |
| 28 | 1.78 | 1.71 |
| 29 | 0.98 | 1.45 |
| 30 | 1.85 | 1.70* |
| 31 | 4.02 | 1.94* |
| 32 | 0.88 | 1.15 |
| 36 | 1.25 | 1.12 |
| 37 | 0.73 | 1.10 |
| 40 | 1.99 | 2.42* |
| 41 | 0.78 | 1.20* |
| 43 | 1.18 | 0.97 |
| 45 | 1.09 | 1.06+ |

* These are measured values at 100 F for similar fluids given in (59)

** Fluid 25 is the reference oil and the values given are interpolated from the measured ones in (41)

+ Values measured at 77 F

paraffinic petroleum derivatives and is therefore not applicable to most of the fluids tested. The relation between $\alpha$ and C is $\alpha = (n - 1)C$, in general n = 16 therefore $\alpha = 15C$ where C and $\alpha$ have the same units.

Roelands' method is also derived from measurements on petroleum fractions but takes the percentage of carbon in rings ($C_r$) into account, with the restriction that $C_r$ lies between 25% and 75%. This excludes most fluids tested and where applied to pure fluids with $C_r = 0$ or 100% the results are unrealistic. The viscosity relation is:

$$\log(\log \mu + 1.200) = Z \log\left(1 + \frac{p}{28,440}\right) + \log(\log \mu_o + 1.200)$$

where p is in p.s.i. To get the equivalent pressure viscosity coefficient from this equation involves pages of algebra, but the final result is:

$$\alpha = \frac{Z \ln(15.85 \mu_o)}{28,440} \text{ (p.s.i.)}^{-1}$$

8.3 Non-Newtonian Behaviour

So far it has been assumed that the fluids obey Newton's viscosity law, which implies that the viscosity of the fluid is independent of shear rate. Most fluids under usual flow conditions are Newtonian, but at high rates of shear and therefore high shear stresses, certain fluids show a reduction in their viscosities. This reduction is well known in the case of polymer thickened oils. It is caused by the long polymer chains, which are randomly orientated under normal conditions, becoming aligned by the high shear stress in such a way that they can slide over one another more easily. When the stress is removed the fluid recovers its former viscosity; the phenomenon is therefore known as temporary viscosity loss. If conditions are too severe the long chains can be broken, this leads to permanent viscosity loss.

In addition to viscous deformation fluids also deform elastically. The elastic term is usually small but can become significant at high

stresses. Fluids in which both modes of deformation are significant are said to be viscoelastic. Early workers used an inadequate model of viscoelasticity, but Dyson (67) has since solved the lubrication problem using a more satisfactory one. A full interpretation of the results in terms of viscoelasticity requires values of viscoelastic parameters which are not available. The qualitative effect on film thickness can however be predicted on physical grounds, because if the fluid deforms by an elastic in addition to a viscous mechanism the total resistance to deformation, and therefore the film thickness generated, will be lower than in the purely viscous case. As the effect becomes more significant as shear rate and therefore speed is increased, the reduction in film thickness will be greater at high speed, and consequently the slope of the thickness versus speed line 'a' will be reduced.

8.4 Estimation of Shear Rate

To assess possible non Newtonian behaviour it is useful to have some idea of the shear rates involved. Dyson (42) has shown that for line contact, in pure rolling with a Newtonian lubricant, the maximum shear rate $\Gamma_{max}$ occurs in the inlet region where $h = 2h_o$, where $h_o$ is the film thickness in the centre, and that $\Gamma_{max} = (3U/4h_o)$. With point contact, as investigated here, the shear must vary much more over the contact zone than it does with line contact, but the maximum value is likely to be similar. Values of shear rate for all the fluids have been calculated for $(\mu_o U/E'R) = 4 \times 10^{-11}$, and are listed in Table 1. These values are in the range $0.5 \text{ —— } 40 \times 10^6$ reciprocal seconds, which is one or two orders of magnitude higher than that achieved by conventional viscometry operating at atmospheric pressure. It is also higher than that at which most film thickness measurements have been made; one reason for this is the use of thinner fluids. Shear rate can be shown to be

more highly dependent on viscosity than speed as follows:

$$\Gamma_{max} \propto \left(\frac{U}{h_o}\right) \quad \text{and} \quad h_o \propto (U\mu_o)^{0.7} \ ,$$

$$\text{therefore} \qquad \text{max} \quad \frac{U^{0.3}}{\mu_o{}^{0.7}} \ .$$

The same formula has been used to calculate the shear rate for the fluids which are non-Newtonian, and will give low values in these cases; for polymer thickened fluids the shear rate for the base fluid would be nearer the true value.

8.5 Viscosity Loss of Fluids Containing Long Chain Molecules

Evidence of temporary viscosity loss is provided by two series of fluids which are thickened with a polymethacrylate VI improver. The values of $\left(\frac{h_o}{R}\right)_4$ show a steady reduction with increasing polymer content. This could be interpreted as a reduction in pressure-viscosity coefficient, but the cause is almost certainly a reduction in effective viscosity at high shear rate. If in the absence of independently measured values, the pressure viscosity coefficients are assumed to equal those of the base fluids and all the reduction in thickness attributed to temporary viscosity loss, an equivalent viscosity $\mu_e$ can be determined. This equivalent viscosity is the value which will make the result for the polymer solution lie on the same dimensionless line as its base fluid. Using this value of $\mu_e$ the temporary viscosity loss, $S = (\mu_{blend} - \mu_e) / \mu_{blend}$, and the loss of viscosity improvement, $\psi = (\mu_{blend} - \mu_e) / (\mu_{blend} - \mu_{base})$, can be evaluated, where $\mu_{blend}$ and $\mu_{base}$ are the conventional viscosities of the polymer blended oil and its base fluid respectively, from Table 1. Values of $\mu_e$, S and $\psi$ are listed in Table 3. The loss of viscosity improvement $\psi$ is the most valuable comparison, because as shown in Fig. 33 the polymer

Table 3

High Shear Viscosity Loss of Polymer Blended Fluids

| Fluid No. | Polymer Content % | Viscosity $\mu_o$ cP | Effective Viscosity $\mu_e$ cP | Temporary Viscosity Loss S % | Loss of Viscosity Improvement $\Psi$ % |
|---|---|---|---|---|---|
| Base fluid - Polyisobutylene oil | | | | | |
| 5 | 0 | 58.9 | 58.9 | 0 | 0 |
| 6 | 5 | 82.4 | 66.6 | 19 | 67 |
| Base fluid - Bitetramethyloctyl | | | | | |
| 7 | 0 | 40.4 | 40.4 | 0 | 0 |
| 8 | 1 | 51.7 | 43.7 | 15 | 71 |
| 9 | 3 | 87.2 | 50.1 | 43 | 79 |
| 10 | 8 | 264.6 | 72.7 | 72 | 86 |
| Base fluid - Hydrogenated polyphenyls | | | | | |
| 19 | 0 | 76.2 | 76.2 | 0 | 0 |
| 20 | 1 | 119 | 80 | 33 | 91 |
| 21 | 3 | 229 | 92.3 | 60 | 90 |
| 22 | 8 | 631 | 134 | 79 | 90 |
| Base fluid - Pentaerithritol tetravalerate | | | | | |
| 37 | 0 | 27.1 | 27.1 | 0 | 0 |
| 38 | 5 | 74.4 | 37.2 | 50 | 79 |

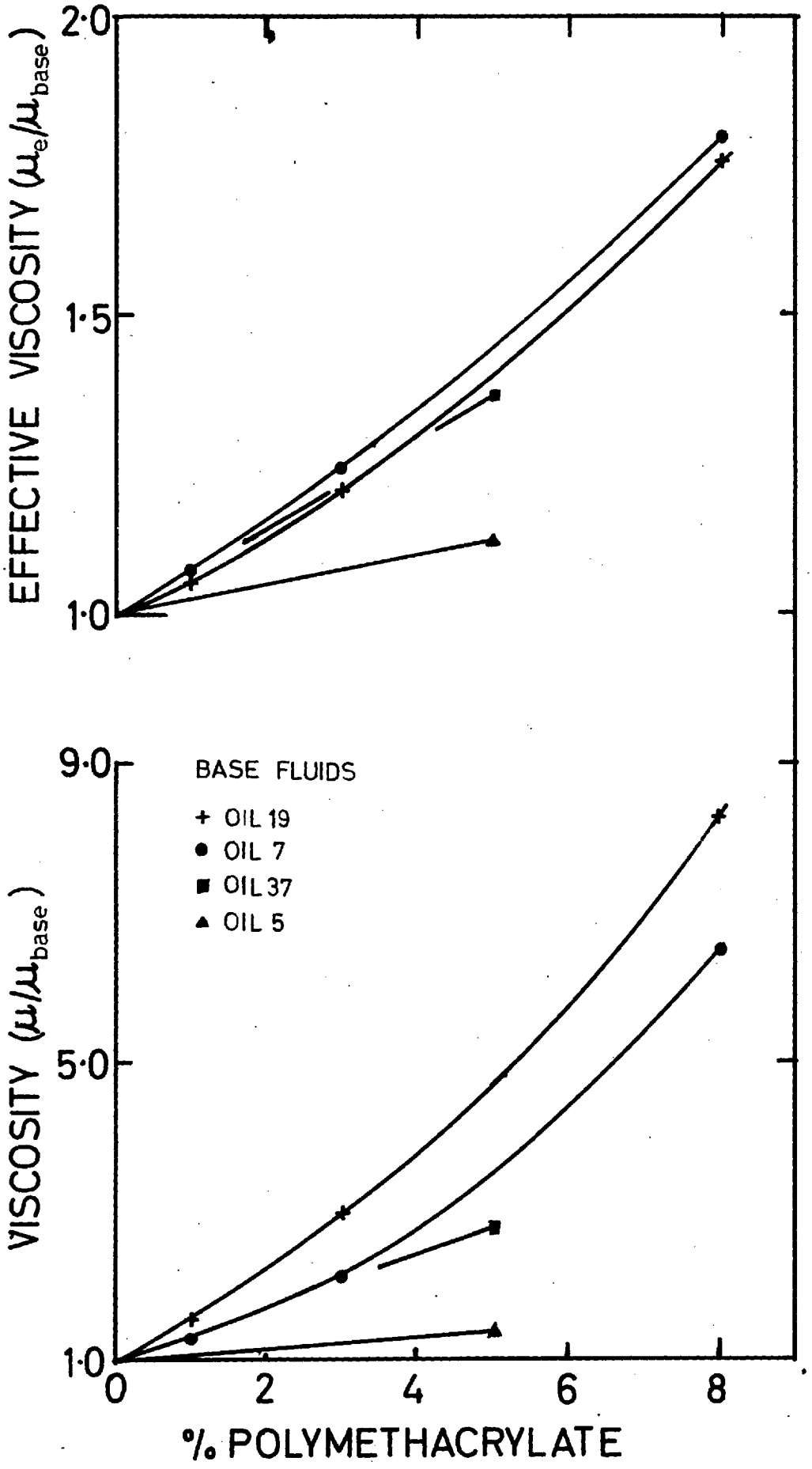



Fig. 33 Effect of polymethacrylate VI improver

has different thickening properties in different base fluids.

In addition to the polymer blended oils, two other sets of thickened oils were tested; one in which a modified polyphenyl ether (fluid 32) is thickened by the addition of 6P5E polyphenyl ether (viscosity 1,916cS at 100 F), and the other in which a highly refined napthenic oil (fluid 12) is thickened by the addition of a super refined heavy paraffinic resin (viscosity 4,454cS at 100 F). Fluid 16 is of particular interest as it is thickened with 14% of medium resin and has the same viscosity as fluid 15, which is thickened with 8.75% of heavy resin. These resins are referred to in (90).

The graph Fig. 34 and the values in Table 1 show that the properties of the polyphenyl ether mixtures are a simple blend of the properties of the two components, there being no viscosity loss effect. The resin thickened napthenic oil on the other hand shows an unusual effect, the viscosity loss increases with resin content, except that fluid 15 (8.75% heavy resin) shows an unexpectedly high loss, this fluid also shows an unexpectedly high viscosity in the graph Fig. 34. The reason for this behaviour is not known, but it is thought that the resin must show some VI improver effect that peaks around 9% concentration. Fluid 16 which contains 14% of medium resin gives a thicker film than fluid 15. This is presumably because the molecules of the medium resin are shorter and therefore less subject to orientation effects than the heavy resin.

The polymer thickened oils are expected to have viscosity versus shear rate graphs of the form shown in Fig. 35, the scales being different for different fluids; this is similar to the graph shown by Philippoff (68) for API-103, a polyisobutylene thickened oil, in which $\Gamma_1 = 2 \times 10^2$ (sec)$^{-1}$ and $\Gamma_2 = 10^6$ (sec)$^{-1}$. In region 1 the blend is Newtonian and the slope 'a' will be near 0.7, in region 2 the polymer additive is gradually losing

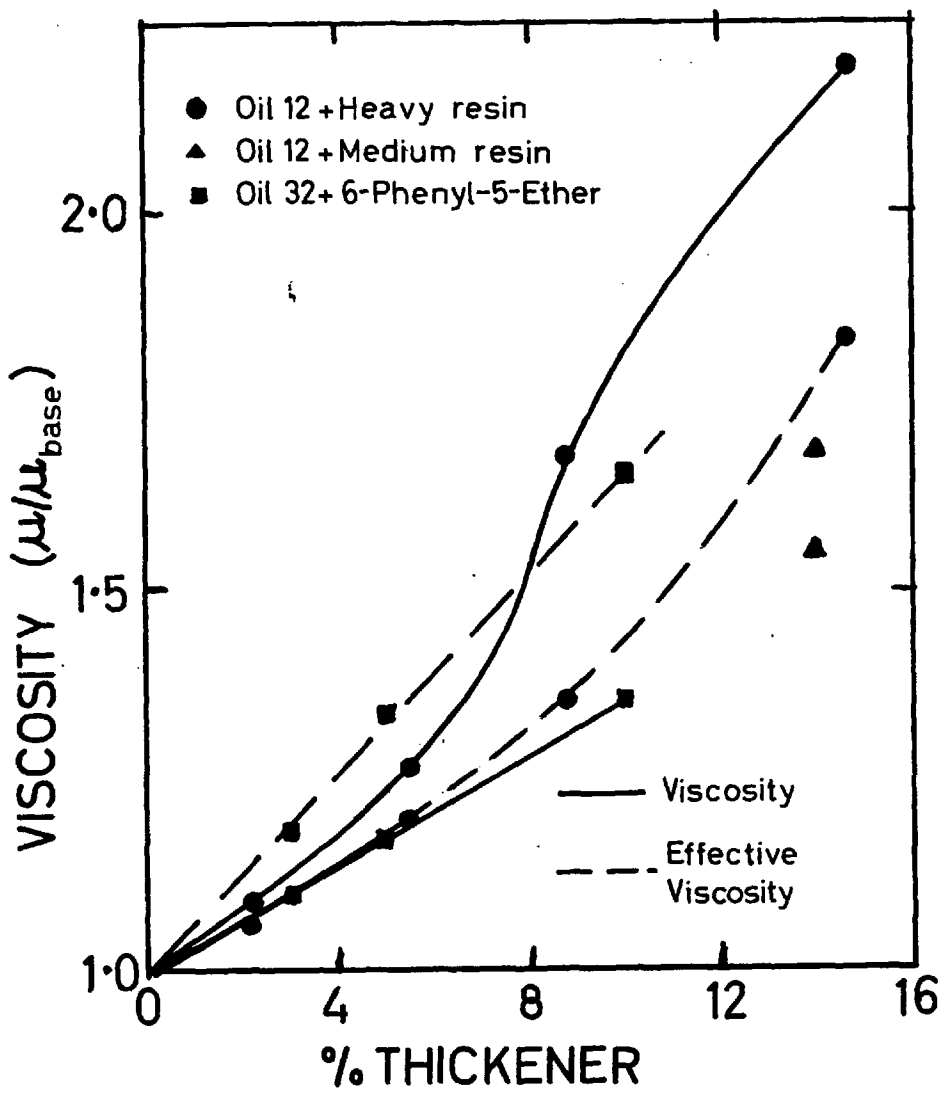



Fig. 34 Effect of thickeners

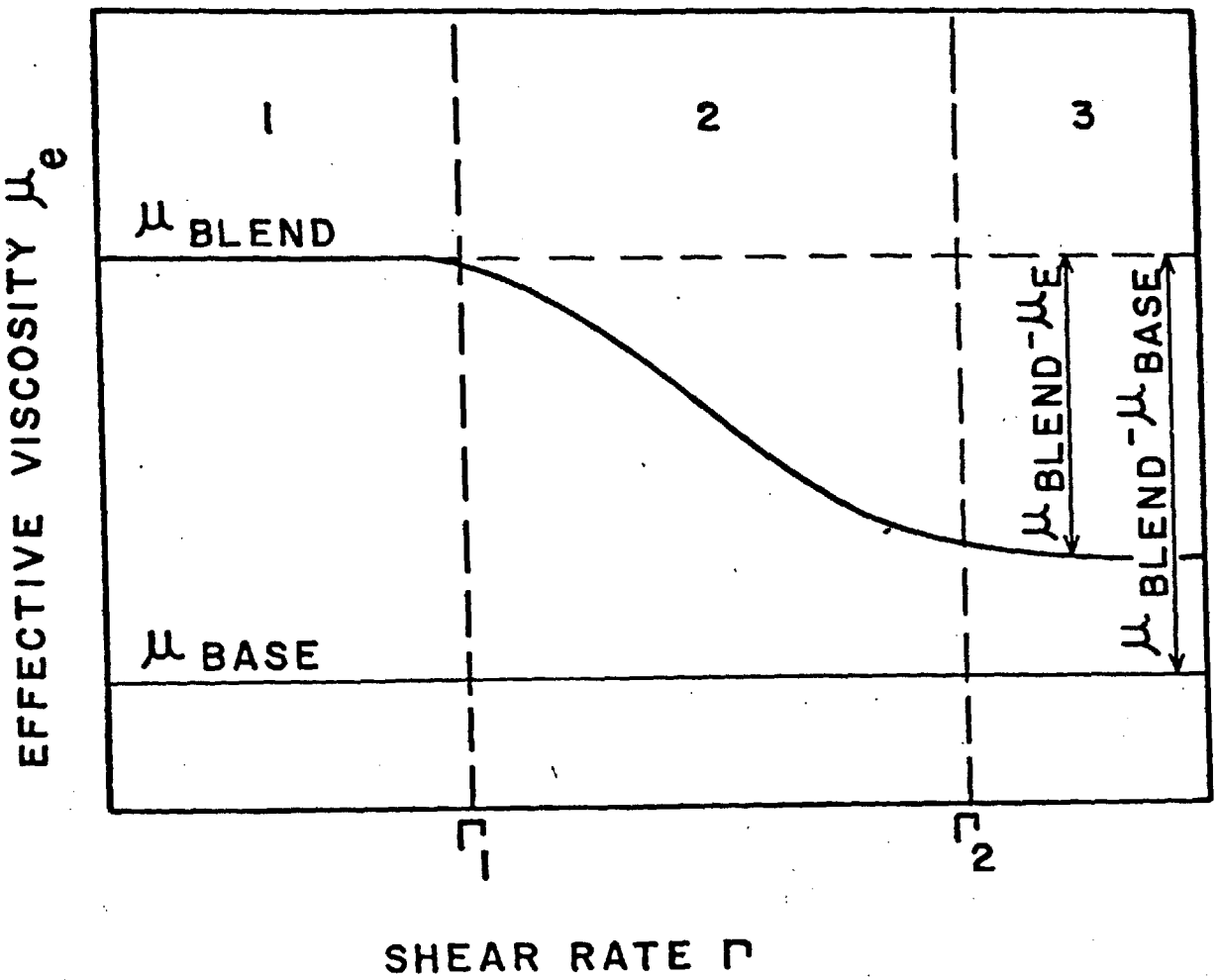



Fig.35. Viscosity versus Shear Rate for a non-Newtonian Fluid.

its effect so that the slope 'a' will be considerably less than 0.7, and in region 3 the behaviour is governed by the base fluid so that the slope 'a' will again be near 0.7. The fact that the slopes of all the polymethacrylate thickened fluids are the same as those of their pure fluid bases, suggests that these test results are in region 3 where the polymer has lost its effect.

A possible explanation for the heavy paraffins (Oils 1 and 11) giving a thinner film than expected, is that being viscous they contain some long chain molecules which orientate to produce temporary viscosity loss. This may also be the reason for the fluorocarbon (fluid 40) having a lower $\alpha_r$ than its measured pressure-viscosity coefficient would suggest, especially as the thinner fluorocarbon (fluid 39, which is a similar polymer but with shorter chain lengths) gives a very high $\alpha_r$.

8.6 Evidence of Non-Newtonian Behaviour in Pure Fluids

The presence of long chain molecules, can not account for the lower values of $\alpha_r$ in Table 2 for the two aromatic compounds (fluids 26 and 29), which were purified by distillation and are free of any higher molecular weight compounds. In this case the fluid molecules themselves may orientate under the high rates of shear, as suggested by Bondi (74), to give pressure-viscosity coefficients lower than expected from static pressure-viscosity measurements. This type of orientation and consequent viscoelastic behaviour may explain the differences in slope. This is born out qualitatively in the results listed in Table 1, which show that it is the thin fluids with the very high rates of shear that show the reduction in slope expected from viscoelastic fluids.

If it were possible to measure film thickness over a greater range of speed, one would expect the $\left(\frac{h_o}{R}\right)$ versus $(U\mu_o/E'R)$ line to start with a slope of 0.7 and gradually fall below it as speed increases. Unfortunately, the

speed range for most fluids is limited to a ratio of 10:1 which is a ratio of shear rates of 2:1, ($10^{0.3}$ :1); the minimum speed is set by the difficulty of measuring films thinner than about $10^{-5}$ cm, and the maximum by the impossibility of distinguishing between shear rate and temperature effects. The tests on 5 phenyl-4-ether (Oil 31), which is a very thick fluid that can be run over a much greater speed range before a measurable temperature rise occurs, shows this effect, (Fig. 24). The slope is constant at .66 for most of the range but deviates at $\left(\frac{\mu_o U}{E'R}\right) \approx 5 \times 10^{-10}$ whereas the temperature as measured, does not rise until $\left(\frac{\mu_o U}{E'R}\right) \approx 1.5 \times 10^{-9}$. The shape of the contacts are very different at such high speed however (Fig. 26), and it might be possible for Newtonian theory to predict a reduction in slope.

It could be argued that the temperature increase in the oil film due to adiabatic heating could affect the slope, but if this were the case the reduction in slope would be most marked with those fluids showing the greatest change of viscosity with temperature (indicated by ASTM slope in Table 1). If anything, the trend is in the opposite direction.

The fact that many of the thin fluids show a low slope 'a' suggests that these have a similar viscosity versus shear rate curves to polymer blend fluids (Fig 35), and that the tests are run in region 2, the difference being that $\Gamma_1$ is much greater for these fluids.

8.7 Effect of Fluid Structures on Film Thickness

A very wide range of fluid structures has been studied, but apart from the polymer solutions and the other fluids suspected of being highly non-Newtonian, no partucularly strong trends emerge except that the napthenic fluids tend to give a higher $\alpha_r$ than paraffinics or ethers at a similar shear rate. Many unsaturated hydrocarbons together with their hydrogenated analogues are included and here a strong trend does appear; in all cases

the hydrogenated analogue has a higher viscosity, gives a greater slope 'a' and a larger value of $\alpha_r$ than the unsaturated compounds. These pairs are squalene and squalane, isopropylbiphenyl and isopropylbicyclohexyl, polyphenyl eutectic and hydrogenated polyphenyls, and m-diphenoxybenzene and 1-3-dicyclohexyloxycyclohexane; the unsaturated compounds being given first. Further points to note are that the high molecular weight reactive additive in oil 2 has no effect on the film thickness, and that differences in density seem to play little part. Fluid 43, the silicone with a high fluorine content (judged by its high density and low refractive index), gives a thicker film than the other silicones, which is of interest in view of the thick films produced by the thin fluorocarbon.

8.8 Possible Effect of Inertia Terms

It was suggested by R. L. Johnson of the NASA research centre that the reason for some fluorinated fluids giving thick films might be inertia terms. These are ignored in traditional lubrication theory and may become significant when high density fluids are used. In (83) it is shown that convective inertia (the mechanism by which fluid boundary layers are formed) can be important in viscous-seal theory and a modified Reynolds' number $Re^* = \frac{u\rho c^2}{\mu L}$ where 'c' is a typical thickness and 'L' a typical length is defined. If 'c' is taken as the centre point film thickness 'L' the Hertz diameter and 'u' the mean rolling speed, $Re^* \approx 10^{-6}$ for the thin fluorocarbon. If 'c' is taken as the thickness in the inlet region at $r = 2a$ where pressure generation is at its most important $Re^* \approx 10^{-4}$. According to (83) inertia effects become significant if $Re^* \geqslant 10^{-2}$, this suggests convective inertia does not operate in this system and unusual values of $\alpha_r$ can not therefore be explained in terms of it. In the case of thin fluids however, where viscosities are a factor of 10 lower and speeds a factor on 10 higher for the same film thickness, $Re^* \approx 10^{-2}$ and inertia effects may be coming into play.

## CHAPTER 9 EHL THEORY OF POINT CONTACT

### 9.1 Introduction

Existing solutions for the point contact EHL problem either use a Grubin type analysis (33) or divide the contact into strips and use line contact theory with a side leakage factor (34). Neither of these approximate techniques can predict the minimum film thickness which occurs in the lobes of the contact, or the pressure spikes which must be associated with them. The full theory for point contact, even in the isothermal incompressible Newtonian case, is a formidable problem, but using the shapes measured in this thesis as a starting point it is possible to gain an insight into possible methods of solution.

### 9.2 Basic Equations

The co-ordinate system used is shown in Fig. 36.

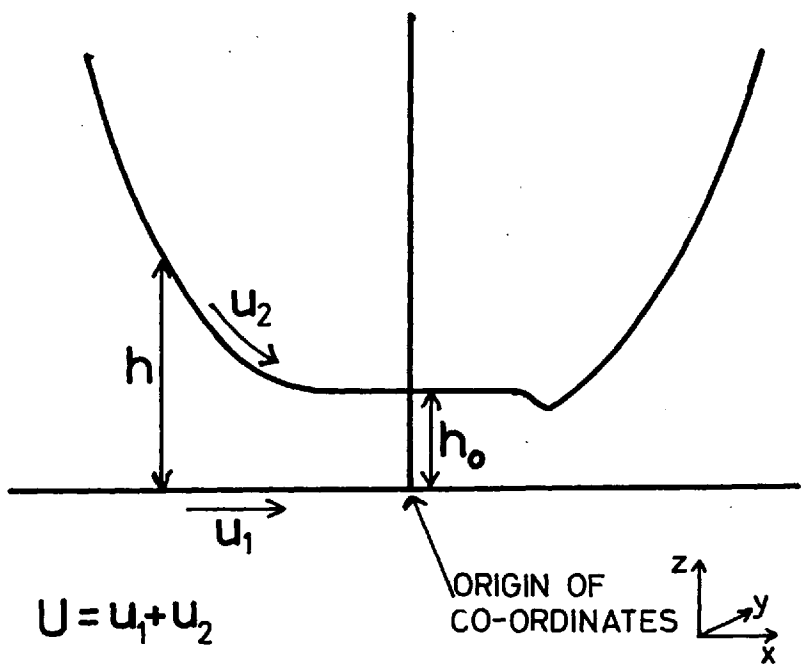



Fig. 36 Co-ordinate system

The equations governing elastohydrodynamics in point contact are:

1) Reynold's equation for pressure distribution in hydrodynamic lubricant films which in cartesian co-ordinates in the appropriate form is:

$$\frac{\partial}{\partial x}\left(\frac{h^3}{\mu}\frac{\partial p}{\partial x}\right) + \frac{\partial}{\partial y}\left(\frac{h^3}{\mu}\frac{\partial p}{\partial y}\right) = 6U\frac{\partial h}{\partial x} \qquad \ldots\ldots 1$$

2) An equation relating viscosity and pressure, the simplest of which is:

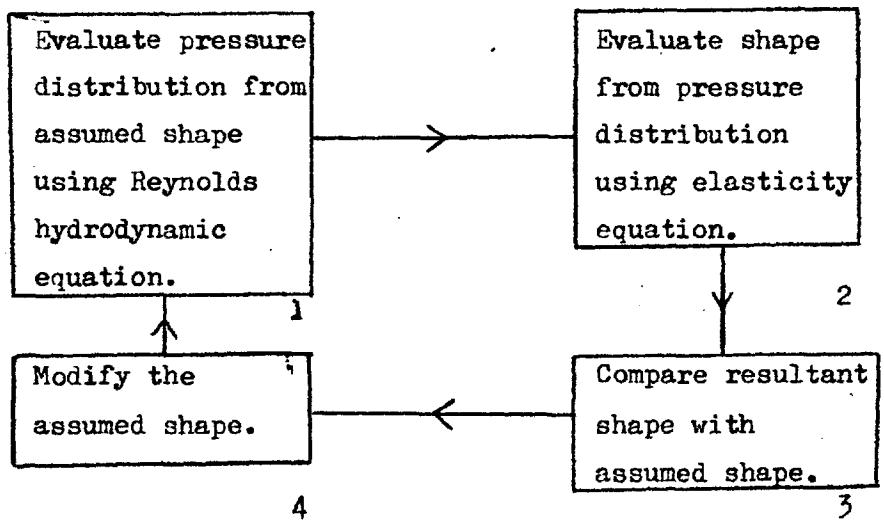
$$\mu = \mu_o e^{\alpha p} \qquad \ldots\ldots 2$$

3) The equation governing the sum of the elastic deformation of the two bodies is:

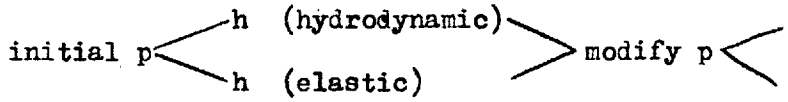
$$h(x,y) = \frac{x^2 + y^2}{2R'} + \gamma + \frac{2}{\pi E'}\iint_F \frac{p(x',y')}{\left[(x-x')^2 + (y-y')^2\right]^{\frac{1}{2}}}\,dx'dy' \qquad \ldots\ldots 3$$

Geometrical term — Deformation term

These three equation must be solved simultaneously to obtain a solution. The pressure viscosity equation can be incorporated into Reynold's equation by simple analysis, but there is no way as yet conceived of combining the resultant with the elasticity equation. A sequence of numerical routines must be developed. The sequence explored here is



The system found most satisfactory in the line contact case (28) is:




One reason for this, is that a small error in h causes a large error in p, and it is therefore more stable to use the inverse hydrodynamic equation to evaluate thickness from pressure. The inverse hydrodynamic equation is relatively simple in one dimension, but in two dimensions it would be necessary to solve 10,000 simultaneous cubic equations (for a 100 x 100 mesh) to obtain h, by finite difference techniques. Another reason for starting with an assumed shape in point contact is that the optical measurements provide an excellent initial shape.

The first stage in attempting a solution is to put the equations in their most convenient form and develop routines for solving each individually.

9.3 Reynolds' Equation

Reynolds' equation 1 can be simplified if p is replaced by a reduced pressure p* which has the property:

$$\frac{dp}{dp^*} = \frac{\mu}{\alpha \mu_o}$$

in which case

$$\frac{\partial}{\partial x}\left(h^3 \frac{\partial p^*}{\partial x}\right) + \frac{\partial}{\partial y}\left(h^3 \frac{\partial p}{\partial y}\right) = 6U\alpha\mu_o \frac{\partial h}{\partial x} \qquad \ldots\ldots 4$$

A suitable reduced pressure is $p^* = 1 - e^{-\alpha p}$ which is a dimensionless parameter varying between zero at low pressure and unity when p is large (greater than 20,000 psi). Previous workers (28) have used $p^* = \frac{1}{\alpha}(1 - e^{-\alpha p})$, which has the dimensions of pressure and varies between 0 and $\frac{1}{\alpha}$. There seems to be little point in unnecessarily defining a dimensioned quantity in one line and making it dimensionless in the next. A disadvantage of

of these parameters is that for example if $\alpha$ = 2 x $10^{-4}$ $in^2/lb$ and p = 50,000 $lb/in^2$, p* = 0.99995 whereas if p is doubled to 100,000 $lb/in^2$, p* = .999999998, which is a change of 1 part in 20,000. As the computer only works with 8 significant figures the last few of which will be affected by the truncation and rounding errors involved in numerical work, it is impossible to get valid results in the high pressure region within the contact. This disadvantage has been overcome to some extent by using $p^* = e^{-\alpha p}$ in which case although the change is still in the fifth decimal place, it is the first and not the sixth significant figure. The only difference to equation 4 is a change in sign of the RHS.

To solve equation 4 it is necessary to put all the differentials into finite differences, read in the matrix of values of h at the mesh points, and use a relaxation technique to find the values of p at the mesh points. An inspection of the contours in Figs. 20,25 show that h and consequently p change repidly in the radial direction but quite slowly in the circumferential direction. This makes it possible to represent the shape and pressures adequately with fewer points if polar co-ordinates r and $\theta$ are used. The step length in the r direction must be fine whereas that in the $\theta$ direction can be relatively coarse.

Reynolds' equation is converted into polars by Cameron (72) and in the appropriate form is:

$$\frac{1}{r}\frac{\partial}{\partial r}\left(r h^3 \frac{\partial p^*}{\partial r}\right) + \frac{1}{r^2}\frac{\partial}{\partial \theta}\left(h^3 \frac{\partial p^*}{\partial \theta}\right)$$

$$= 6U\alpha\mu_o\left(\cos\theta \frac{\partial h}{\partial r} - \frac{\sin\theta}{r}\frac{\partial h}{\partial \theta}\right) \qquad \ldots\ldots 5$$

It is more convenient to handle if made dimensionless and fully differentiated. The most suitable dimensionless parameters to use are $H = \frac{h}{a}$ and $R = \frac{r}{a}$; p* is already dimensionless. In dimensionless fully differentiated form

Reynolds' equation becomes:

$$RH^3 \frac{\partial^2 p^*}{\partial R^2} + \left(H^3 + 3RH^2\right)\frac{\partial H}{\partial R}\frac{\partial p^*}{\partial R} + \frac{H^3}{R}\frac{\partial^2 p^*}{\partial \theta^2} + \frac{3H^2}{R}\frac{\partial H}{\partial \theta}\frac{\partial p^*}{\partial \theta}$$

$$= 6\left(\frac{U\alpha\mu_o}{a}\right)\left(R\cos\theta\frac{\partial H}{\partial R} - \sin\theta\frac{\partial H}{\partial \theta}\right) \qquad \ldots\ldots 6$$

In terms of the dimensionless groups already defined in Chapter 3

$$\left(\frac{U\alpha\mu_o}{a}\right) = \left(\frac{U\mu_o}{E'R'}\right)(\propto E')\left(\frac{a}{R'}\right)^{-1} \quad \text{and} \quad \left(\frac{a}{R}\right) = \left(\frac{3}{2}\frac{W}{E'R'^2}\right)^{\frac{1}{3}}$$

Equations 5 and 6 are correct for $p^* = 1 - e^{-\alpha p}$ and a co-ordinate system in which $\theta = 0$ on the positive x-axis. For computational reasons it is easier to have $\theta = 0$ on the negative x-axis, this in effect changes the sign of U, but as previously discussed, the change from $p^* = 1 - e^{-\alpha p}$ to $p^* = e^{-\alpha p}$ also changes a sign. These changes cancel each other leaving equations 5 and 6 correct.

9.4 Finite difference approximation to Reynolds' Equation

The computation mesh is shown in Fig. 37 and a molecule in Fig. 38. The suffix I denotes position in the R direction and J position in the $\theta$ direction. Negative or zero subscripts are not allowed in the Fortran language which means that $\theta = 0$ must be denoted by $J = 1$, and in general $\theta = (J - 1)\,\delta\theta$. The point at $R = 0$ is a special case being the co-ordinate origin, and is specially denoted, this means that $I = 1$ corresponds to $R = \delta R$ and in general $R = I\,\delta R$. The differentials in equation 6 at a point I,J are replaced by finite differences as follows:

$$\frac{\partial p^*}{\partial r} = \frac{p^*_{I+1,J} - p^*_{I-1,J}}{2\delta R} \qquad \frac{\partial p^*}{\partial \theta} = \frac{p^*_{I,J+1} - p^*_{I,J-1}}{2\delta\theta}$$

$$\frac{\partial^2 p^*}{\partial r^2} = \frac{p^*_{I+1,J} + p^*_{I-1,J} - 2p^*_{I,J}}{\delta R^2} \qquad \frac{\partial^2 p^*}{\partial \theta^2} = \frac{p^*_{I,J+1} + p^*_{I,J-1} - 2p^*_{I,J}}{\delta\theta^2}$$

and similarly for $\frac{\partial H}{\partial R}$ and $\frac{\partial H}{\partial \theta}$.

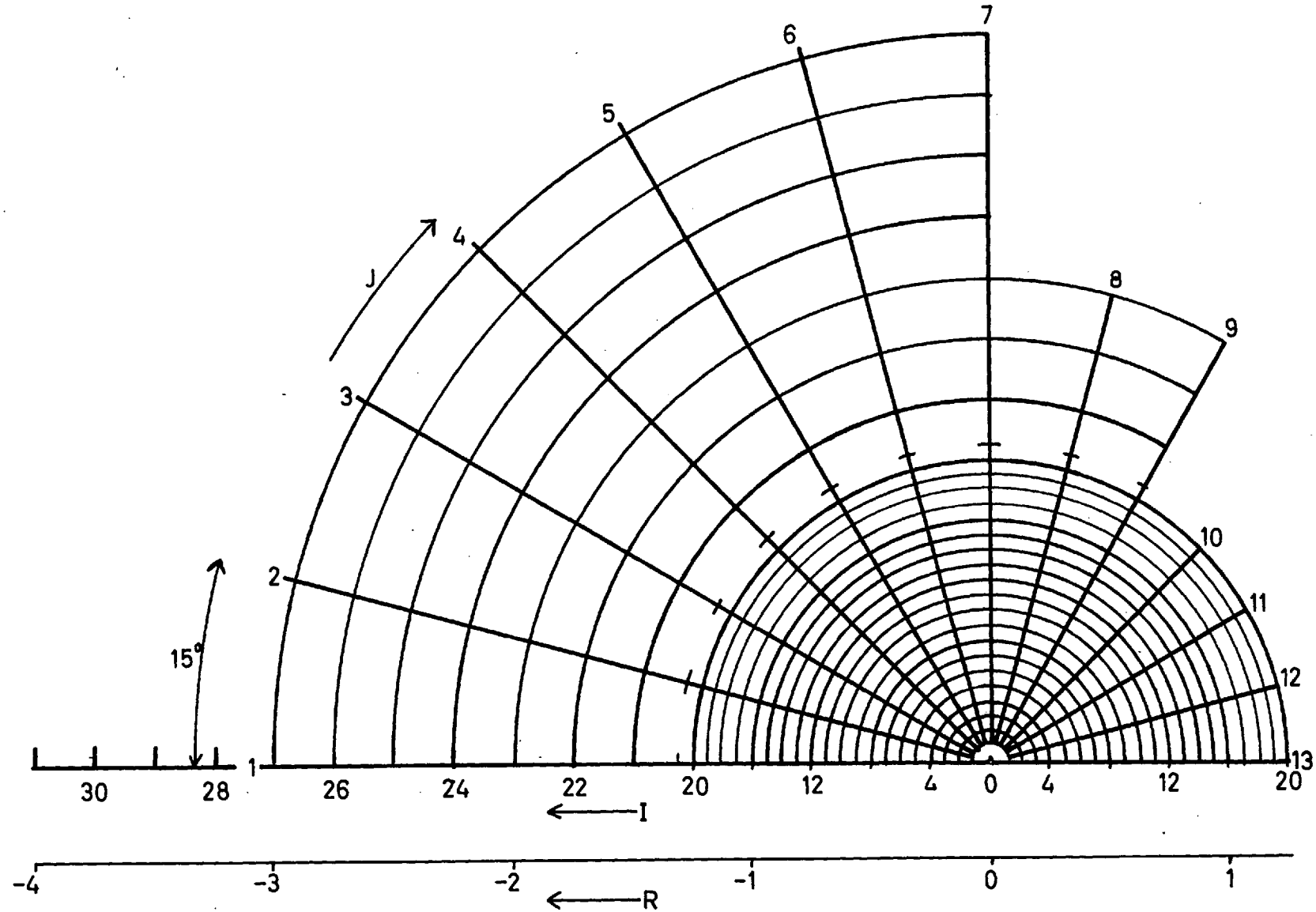



Fig. 37 Computation mesh

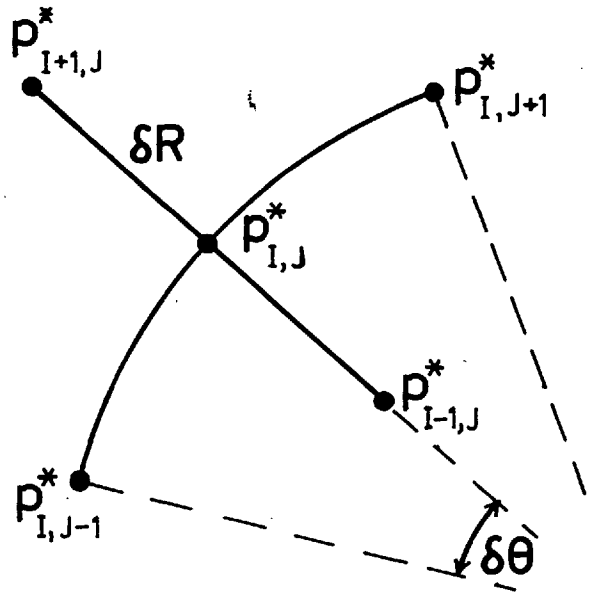



Fig. 38 Relaxation molecule

On simplifying, the finite difference Reynolds' equation becomes:

$$(1 - B)p^*_{I-1,J} - 2(1 + C)p^*_{I,J} + (1 + B)p^*_{I+1,J} + (C - D)p^*_{I,J-1}$$

$$+ (C + D)p^*_{I,J+1} = E_{I,J} \qquad \text{.....7}$$

where $B = \frac{1}{2I} + \frac{3}{4} HI$

$$C = \frac{1}{I^2 \delta\theta^2}$$

$$D = \frac{3C}{4} HJ$$

$$E = 6\left(\frac{U \alpha \mu_o}{a^*}\right)\left(\frac{\delta R \cos\theta}{2} \frac{HI}{H^2_{I,J}} - \frac{\delta R \sin\theta}{2I\ \delta\theta} \frac{HJ}{H^2_{I,J}}\right)$$

$$HI = \frac{H_{I+1,J} - H_{I-1,J}}{H_{I,J}} \quad \text{and} \quad HJ = \frac{H_{I,J+1} - H_{I,J-1}}{H_{I,J}}$$

A relaxation problem such as this one is solved in less computer time if the coefficients are evaluated for each point in the mesh, and stored.

Five coefficients would have to be stored for each point in the mesh. By writing equation 7 in the present form only three easily evaluated coefficients for each point in the mesh, and one coefficient for each value of I need be stored, thus reducing the storage to approximately 62% of the normal requirement. As storage space will be the principal limitation when extending the program to a finer mesh, any saving of space is valuable; and the increase in time would certainly be less than that caused by the use of magnetic tape as a backing store.

Equation 7 and the expressions for coefficients apply only to a typical point in the middle of a field of constant mesh size. As shown by the mesh Fig. 37 the symmetry of the contact about the $\theta = 0$, $\theta = \pi$ line is utilized. This is done by noting that for points on the line of symmetry, $H_{I,J-1} = H_{I,J+1}$ and $p^*_{I,J-1} = p^*_{I,J+1}$ and modifying the equations appropriately. The point at the origin poses special problems because equation 6 is singular when $R = 0$. The problem can be skirted by excluding the point $p^*_{0,J}$ from the iteration scheme. Where it occurs as a $p^*_{I-1,J}$ term, $p^*_{0,J}$ is replaced by $p^*_c$ which is interpolated from the values round it. Where $H_{0,J}$ would occur it is replaced by the measured thickness $H_c$. The interpolation for $p^*_c$ is carried out by fitting a quartic to the two points on each side of the origin on the $\theta = \frac{\pi}{2}$, $\theta = \frac{3\pi}{2}$ line, and gives the result $p^*_c = \frac{1}{3}(4p^*_{1,J} - p^*_{2,J})$ where J is the value representing $\theta = \frac{\pi}{2}$. The expression is so simple because $p^*_{1,J} = p^*_{-1,J}$ and $p^*_{2,J} = p^*_{-2,J}$ by symmetry.

A further point of difficulty is the change of step length. Because I represents a length as well as a point number, an equivalent I which accounts for the local step length not persisting all the way to the origin, must be defined. It is also necessary to evaluate some extra points as in Fig. 37 to enable derivatives on the line of junction (I = 20) to be found.

These points are found by extrapolation from the fine mesh side using a cubic equation.

9.5 Relaxation Solution

The first step in solving the finite difference equations represented by equation 7 is to evaluate the coefficients of p*, and $E_{I,J}$ for every point, and store them in a suitable form. Direct matrix methods of solving for p* are not possible. The coarse mesh used so far, contains over 400 points, and even the largest computers can not handle a 400 x 400 matrix, so some form of iterative solution must be used. The simplest to program is the Gauss-Seidel iteration which can easily be improved to give successive over relaxation. These methods are discussed in (84). For equation 7, a general step in the Gauss-Seidel iteration can be written as:

$$p^*_{I,J} = \Big[- E_{I,J} + (1-B)p^*_{I-1,J} + (1+B)p^*_{I+1,J} + (C-D)p^*_{I,J-1} + (C+D)p^*_{I,J+1}\Big] \Big/ 2(1+C) \qquad \ldots\ldots\ldots 8$$

This equation is applied to all values of (I,J) in sequence, the process being repeated until the required convergence has been achieved. Convergence can be accelerated by introducing an over relaxation factor $\omega$ which magnifies each change in value of $p^*_{I,J}$. Equation 8 becomes:

$$p^*_{I,J} = p^*_{I,J} + \omega \left\{\Big[-E_{I,J} + (1-B)p^*_{I-1,J} + (1+B)p^*_{I+1,J} + (C-D)p^*_{I,J-1} + (C+D)p^*_{I,J+1}\Big] \Big/ 2(1+C) - p^*_{I,J}\right\} \qquad \ldots\ldots\ldots 9$$

If $\omega = 1$, equation 9 reduces to the Gauss-Seidel but if $\omega > 1$ the process is known as successive over relaxation. The number of iterations can be cut by a factor of five or even 10 by careful choice of the factor $\omega$. No theory exists for determining the optimum $\omega$ in the general case, but it is often between 1.5 and 1.9 and can be found by trial and error.

A number of special cases in which equation 9 has to be modified slightly have been mentioned in section 9.4, but in addition to these there are the physical boundary conditions of the problem. The front and side boundaries are far enough from the centre for p to be zero on them. The rear part of the boundary where p must also be zero, is allowed to float and its position determined by imposing the condition that the film ruptures if the pressure goes below zero. This is easily programmed into the iteration by saying, "if $p^* > 1$ put $p^* = 1$," (ie. if $p < 0$ put $p = 0$).

The program together with a listing of the input shape and output pressure is in Appendix 2.

## 9.6 The Elasticity Equation

The normal displacement w at a point (x,y) on the surface of a semi-infinite body, acted on by a distributed pressure p(x',y'), is:

$$w = \frac{1-\sigma^2}{\pi E} \iint_F \frac{p(x',y')}{\left[(x-x')^2 + (y-y')^2\right]^{\frac{1}{2}}} \, dx'dy' \qquad \ldots\ldots\ldots 10$$

where F is the field of integration and covers the area where p is significant.

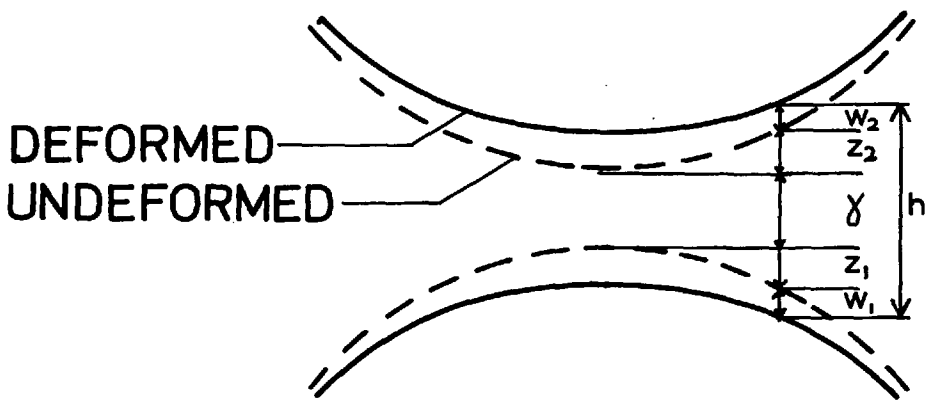



Fig. 39 Geometry of contact zone

The geometry of a deformed contact is shown in Fig. 39 and gives the result:

$$h = z_1 + z_2 + \gamma + w_1 + w_2 \qquad \ldots\ldots\ldots 11$$

where $z_1$ and $z_2$ represent the geometry of the undeformed surfaces, $\delta$ their separation, and $w_1$ and $w_2$ are the elastic displacements due to the pressure field. If bodies 1 and 2 are spherical, and the reduced radius R' and Young's modulus E' are introduced, equation 11 becomes:

$$h(x,y) = \frac{x^2 + y^2}{2R'} + \delta + \frac{2}{\pi E'} \iint_F \frac{p(x',y')}{\left[(x-x')^2 + (y-y')^2\right]^{\frac{1}{2}}} \, dx'dy' \qquad \ldots\ldots\ldots 12$$

which can be made dimensionless by putting $X = \frac{x}{a}$, $Y = \frac{y}{a}$, $G = \frac{\delta}{a}$, $H = \frac{h}{a}$, $X' = \frac{x'}{a}$, $Y' = \frac{y'}{a}$ and $P = \frac{p}{p_o}$ and becomes:

$$H(X,Y) = \left(\frac{a}{R'}\right) \frac{(X^2 + Y^2)}{2} + G + \frac{2p_o}{\pi E'} \iint_F \frac{P(X',Y')}{\left[(X-X')^2 + (Y-Y')^2\right]^{\frac{1}{2}}} \, dX'dY' \qquad \ldots\ldots\ldots 13$$

The main difficulty in evaluating equation 13, is the double integral term which contains a singularity when X = X' and Y = Y'. If P is an analytical function of (X',Y') the integral can often be integrated analytically as it was in classical solution of the Hertz problem (85), but in a direct numerical solution an infinite value occurs in the integrand.

## 9.7 Techniques of Integration

To test possible methods of integration, a program was set up to find the shape of a Hertzian contact. The numerical result could be compared with the analytical solution and the numerical method assessed.

The numerical method involves dividing the pressure field into a mesh in which points are numbered $P_{I',J'}$, and the displacement field into an indentical mesh in which points are numbered $H_{I,J}$. To find the displacement at a single point (I,J) Fig. 40 it is necessary to perform a numerical integration which takes in the terms $\frac{P_{I',J'}}{s}$ for every point in the mesh. s is the distance between (I',J') and (I,J). As the lubrication problem is symmetrical about the X-axis the number of points in the integration

can be reduced by letting $F_{I'J'} = P_{I'J'}\left(\frac{1}{s} + \frac{1}{s'}\right)$. When the point (I,J) is outside the pressure field the singularity does not arrise, and the points $F_{I'J'}$ form a smooth surface which can be integrated using Simpson's rule. If the Hertz pressure is divided into a 32 x 32 mesh 5-figure agreement with the analytical solution is achieved.

Inside the pressure zone (which in a practical lubrication problem includes the whole field) the singularity when (I'J') = (I,J) can be avoided by replacing P in the centre by $\frac{P}{4}$ at a distance $\frac{\hat{\varepsilon}}{4}$ out from the centre on each mesh line, Fig. 41. This in effect makes $\frac{P_{I',J'}}{s} = \frac{4P_{I'J'}}{\delta}$, $P_{I'J'}$ can be distributed in other ways but this has been found the most satisfactory. Although the singularity has been removed the surface for $F_{I',J'}$ still has a fairly sharp spike in it, which means that Simpson's rule will give a wavy displacement field because some spikes will be multiplied by a weighting factor of 16 and others by 8 or 4. The trapezoidal (84) rule in which all points except the edges and corners are multiplied by 1 gives a much better result and is easier to program. The values of the film thickness obtained by this method along the X-axis from X = 0 to X = 1 are listed below.

| X | 0 | .125 | .25 | .375 | .5 | .625 | .75 | .875 | 1.00 |
|---|---|---|---|---|---|---|---|---|---|
| H | 7.9 x10$^{-6}$ | 7.7 | 7.3 | 6.4 | 4.9 | 2.3 | -2.3 | -13.4 | -68.6 |

As the table corresponds to the area of Hertzian contact the values of H should be zero. Values of H at X = 1.125 and 1.25 are $6.13 \times 10^{-4}$ and $17.77 \times 10^{-4}$ so the values of H in the table are a good approximation to zero. The reason for the area around X = 1 being less accurate, is that a circular boundary is approximated to by a rectangular mesh.

The accuracy of this technique is adequate with a reasonable step

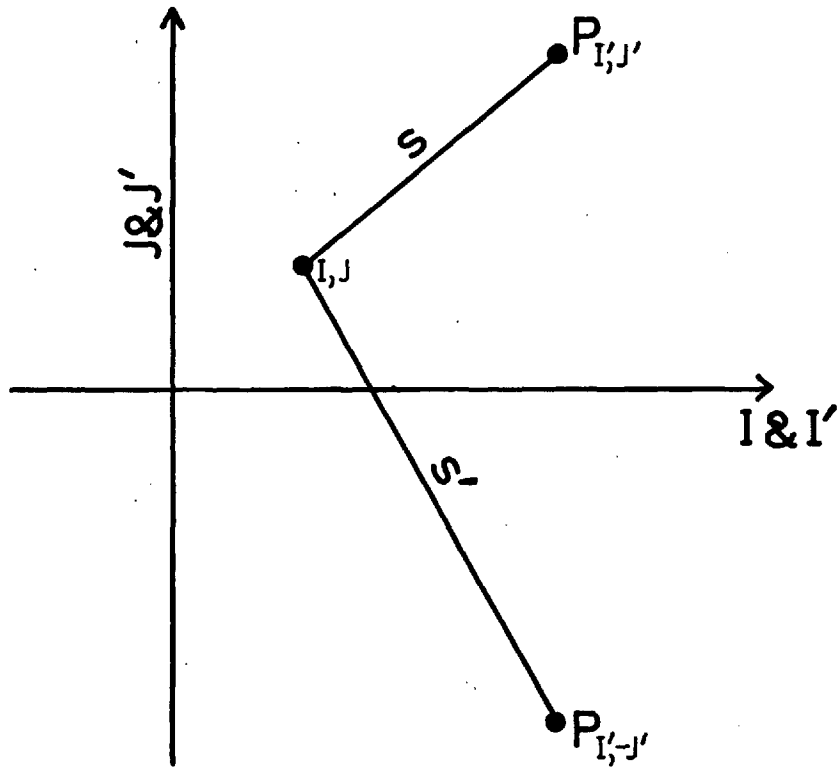



Fig. 40 Displacement at a point

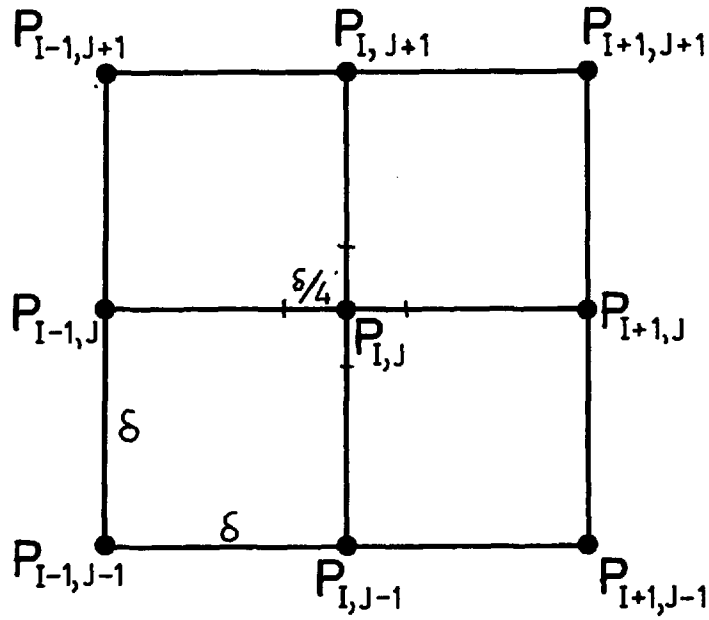



Fig. 41 Singularity point

length, the main disadvantage however is that it takes far too much computer time. The present program which was designed for a variable step length with economy of running time in mind, would take about 30 minutes on an IBM 7090 to evaluate the displacement at every point in the 1,500 point mesh. It is unlikely that the time could be cut to less than 15 minutes even with the help of a computing specialist. The problem is that the integration of over 1,500 points, has to be performed 1500 times.

Dowson and Higginson (23) avoid the singularity in the line contact case by dividing the pressure curve into parabolic sections and integrating analytically. This has been done for the point contact case by integrating a parabolic surface. The resulting integral is so complicated that computation would take considerably longer than the present method. The analytical integral has been applied however, to the area round the singularity (Fig. 41) and gives the displacement due to this pressure area as:

$$w' = .7652(P_{I-1,J} + P_{I+1,J} + P_{I,J-1} + P_{I,J+1}) + 3.9902\ P_{I,J} \qquad \ldots\ldots\ldots 14$$

This displacement is added to that obtained by integrating the values of $F_{I,J}$ over the rest of the field. Equation 14 can be used to find an equivalent value of $F_{I,J}$ for the centre point; instead of $F_{I,J} = 4\ \frac{P_{I,J}}{\delta}$ it becomes:

$$F_{I,J} = \frac{1}{\delta}\left(3.9902\ P_{I,J} + .265196\ \sum_{1}^{4} P_s - .176777\ \sum_{1}^{4} P_c \right. \qquad \ldots\ldots\ldots 15$$

where $\sum_{1}^{4} P_c$ is the sum of the pressures at the corners, and $\sum_{1}^{4} P_s$ the sum of the pressures at the mid points of the sides in Fig. 41. The results obtained by using this technique are no better than those using the simple method, so there is no possibility of being able to increase the mesh size

and thereby reduce computation time.

9.8 Polar Co-ordinates

As Reynolds' equation has been developed for a polar mesh, it is desireable to develop an elasticity program to work on the same mesh. Using the polar mesh however, only 2 figure accuracy has been achieved. This may be because the half Hertzian zone is represented by 200 instead of the 400 points in the cartesian case, or because of a bug in the program which has remained undetected.

The polar equivalent to equation 10 is:

$$w = \frac{1-\sigma^2}{\pi E} \iint_F \frac{p(r'\theta')}{\left[1 + \left(\frac{r}{r'}\right)^2 - 2\left(\frac{r}{r'}\right) \cos(\theta - \theta')\right]^{\frac{1}{2}}} dr'd\theta' \quad \ldots\ldots\ldots\ldots 16$$

and is integrated in a similar way to the cartesian equation. The polar equation is often written as:

$$w = \frac{1-\sigma^2}{\pi E} \iint_F p(r'\theta') \; dr'd\theta'$$

but this only applies at r = 0, and in the present case it is not possible to move the co-ordinate origin to made r = 0 at every point.

# CHAPTER 10 FURTHER DEVELOPMENTS

## 10.1 Evaluation of Lubricants

Considerable interest has been shown by commercial enterprises in the optical technique for evaluating lubricants. In particular they are interested in the development of a rig to run at a high temperature (500-600 F) in a controlled atmosphere and at a higher maximum Hertz stress of 200,000 psi. These conditions are likely to apply in the bearings of the supersonic transport aircraft, and lubricants to stand up to these conditions may have unusual chemical structures with unknown lubricating ability. Using the optical EHL technique it will be possible to measure the relative effectiveness of these lubricants in producing films under realistic conditions.

To meet the load and temperature specifications it will be necessary to use a synthetic sapphire disc instead of the glass. The high Young's modulus of sapphire ($46 \times 10^6$ psi) means that a given load will produce almost twice the maximum Hertz stress of a steel-glass contact. In addition the thermal conductivity of sapphire is similar to that of ferritic steel; consequently the heat flow will be similar to that in a bearing contact. The lubricants will have a very low viscosity under these conditions and very high speeds will be necessary to achieve measurable film thickness, alternatively the film thickness measurement technique must be refined to enable thinner films to be measured, Westlake and Cameron (87) report a promising development in this line.

To gain the full benefit from rigs operating at the high temperatures and pressures it will be necessary to develop techniques of measuring refractive index of lubricants under these conditions.

## 10.2 Design of an Improved Air Bearing

To overcome the disadvantages of the present air bearing (Chapter 5) and to meet the additional specification for the high temperature bearing

a number of design studies have been made. Two designs are being pursued, one for a room temperature rig in which the main emphasis is on convenience and speed of use, and the other for meeting the most exacting specifications.

The room temperature rig (which will in fact be arranged to run at a controlled temperature of 100 F) obviates the disc swashing problem by letting the air jets act directly on the flat underside of the glass disc (Fig. 42). The top load and radial location are provided by the spherical air bearing. The spherical cup can be raised and swung aside to enable the disc to be removed for cleaning. The ball loading system is similar to the existing one but is smaller, works at a higher pressure, and has air jets around the piston so that it can move perfectly freely.

The high temperature rig consists of a 4" diameter sapphire disc which is held in an air bearing by its circumference. It is not possible to have the air acting directly on the sapphire because exhaust bearing air would contaminate the controlled atmosphere. Care has been taken to limit the heat flow from the disc area to the bearing, and also to keep the bearing components symmetrical in order to minimise distortion on heating. The ball loading system is similar to the low pressure rig, but provision for the PTFE cup to be replaced by a hydrostatic bearing (Fig. 43) using the test fluid, is made. The problem with the hydrostatic bearing will be supplying high pressure oil at carefully oontrolled temperatures up to 600 F. The sort of controlled atmospheres envisaged, do not include high vacuum or toxic gases; the requirement is to simulate the nitrogen atmosphere that may be required to reduce lubricant oxidation or fire risk in the engines of supersonic transport aircraft (89). Labyrinth seals should be adequate for this purpose.

More sophisticated methods of temperature measurement will be needed. It will probably be impossible to keep the inlet temperature constant so a device which records the inlet temperature when a thickness is observed,

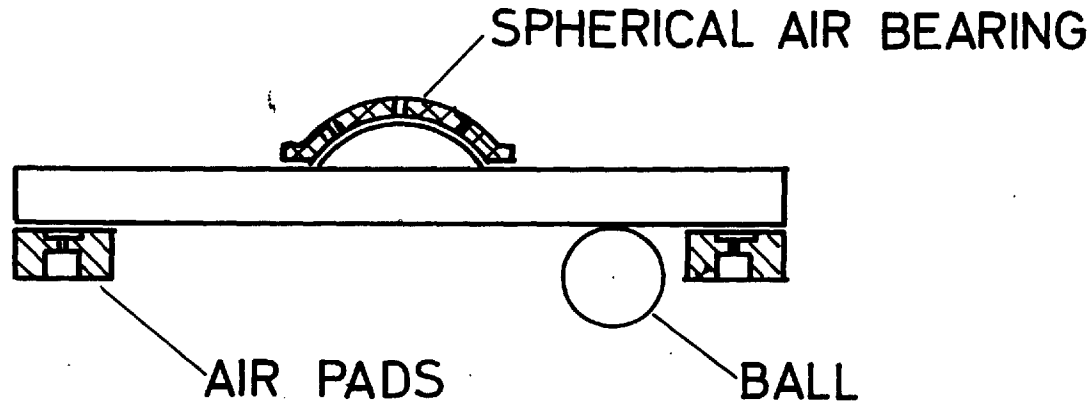



Fig. 42 New air bearing

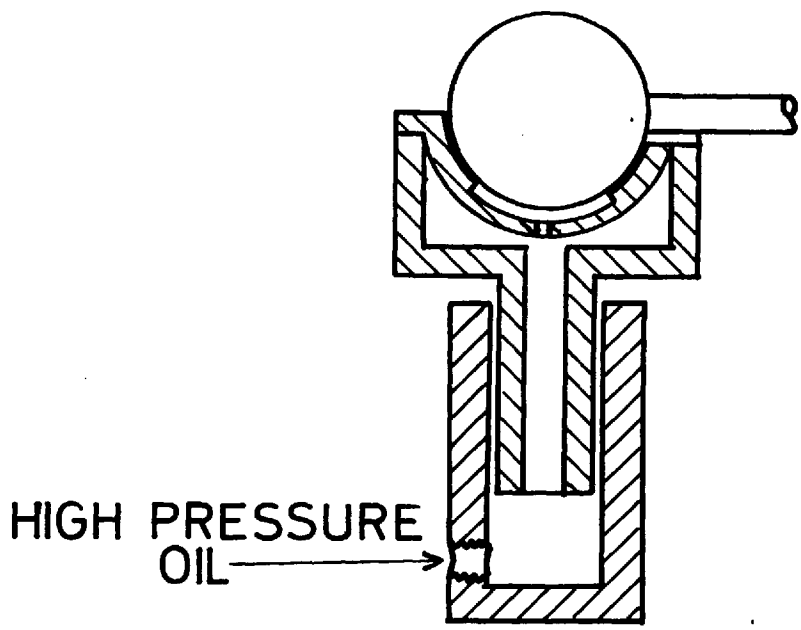



Fig. 43 Hydrostatic loader

will be helpful. It is fortunate that at high temperatures the viscosities of lubricants are less sensitive to temperature change.

10.3 Developments to Theory

It is proposed to extend the hydrodynamic program to a finer mesh and to feed in a variety of speeds, loads, and shapes, to see how the pressure distributions vary. It should also be possible to feed in viscoelastic and compressible fluid models, but any attempt at including temperature effects would complicate matters a great deal. The main need however, is for someone to develop an accurate and economical method of handling the elasticity part of the problem, a fundamental investigation of the phenomenon of elasticity may be of more value than attempts at juggling with existing equations.

## APPENDIX 1 SOLUTION OF THE PRESSURE DISTRIBUTION EQUATION

The equation as developed in Chapter 2.4 is:

$$\frac{\partial P}{\partial T} = A.R^{-\frac{2}{3}} \exp(-DP)\left[\frac{\partial^2 P}{\partial R^2} + B\left(\frac{\partial P}{\partial R}\right)^2\right] = \phi \qquad \ldots\ldots\ldots 1$$

where A, D, and B are constants.

Before considering the method of solution in detail it is helpful to note some features of the solution. Two boundary functions are required for R and one for T (Fig. 44). For the boundary T = 0 (i.e. before

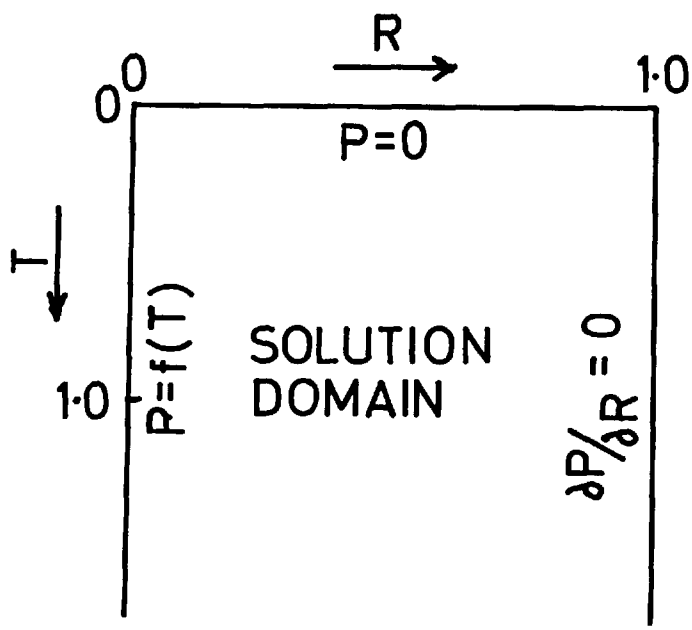



Fig. 44 Solution domain of the crack equation

the pressure pulse starts), P = 0 for all R; for the bondary R = 0 the mouth pressure $P_1 = f(T)$ is known, and for R = 1.0, $\frac{\partial P}{\partial R} = 0$ is the appropriate condition. The solution is marched out in the direction of increasing T from the known initial value at T = 0.

To apply finite difference approximations the solution domains must be divided into a mesh; for computation the range of R is divided into

10 (i.e. $\delta R = 0.1$), the nodal points being numbered I = 1, 2, ...11. The time variable is divided into increments of $\delta T$, the nodal points being numbered K = 1, 2, ...11. The pressure at any point in the mesh can be written as $P_{I,K}$.

Many methods could be tried for this equation, but the simple explicit finite difference methods are not stable with realistic values of A and acceptable step lengths. An implicit method similar to the Crank Nicolson process is evolved as being the most likely to succeed (84,86). This process converts the differential equation to a set of non linear algebraic simultaneous equations as follows:

at time K let $\left(\frac{\partial P}{\partial R}\right)_K = \left(\frac{P_{I+1} - P_{I-1}}{2\delta R}\right)_K$

and $\left(\frac{\partial^2 P}{\partial R^2}\right)_K = \left(\frac{P_{I+1} - 2P_I + 2P_{I-1}}{\delta R^2}\right)_K$

Substituting for $\frac{\partial P}{\partial R}$ and $\frac{\partial^2 P}{\partial R^2}$ in the right hand side of equation 1.

$$K = A\,\delta R^{-8/3}(I-1)^{-2/3}\ \exp(-DP_I)\left[P_{I+1} - 2P_I + P_{I-1} + \frac{B}{4}(P_{I+1} - P_{I-1})^2\right]_K \qquad \ldots\ldots\ldots 2$$

In the simple explicit method, for any K

$$\left(\frac{\partial P}{\partial T}\right)_K = \phi_K \qquad \ldots\ldots\ldots 3$$

$$\therefore\ P_{I,K+1} - P_{I,K} = \delta T(\phi_K) \qquad \ldots\ldots\ldots 4$$

and as P at times K is known, this is an explicit formula for calculating P at time K + 1, unfortunately it is unsuitable except for minute values of $A\frac{\delta T}{\delta R^{8/3}}$.

In the Crank Nicolson method equation 3 is modified to give

$$\left(\frac{\partial P}{\partial T}\right)_K = \tfrac{1}{2}(\phi_K + \phi_{K+1}) \qquad \ldots\ldots 6$$

$$\therefore \; P_{I,K+1} - P_{I,K} = \frac{\delta T}{2}(\phi_K + \phi_{K+1}) \qquad \ldots\ldots 7$$

This can be written as

$$P_{I,K+1} - \frac{\delta T}{2}\phi_{K+1} - P_{I,K} + \frac{\delta T}{2}\phi_K = 0 \qquad \ldots\ldots 8$$

which when applied for all values of I gives a set of non-linear simultaneous algebraic equations for P at time K + 1.

The algebraic equations are solved using the Newton-Raphson method. The initial guesses for P at K + 1 being obtained by extrapolation from those at K and K - 1, and the matrix of partial differentials involved is solved by Gauss-Seidel iteration.

## APPENDIX 2 THE HYDRODYNAMICS PROGRAM

The program is written in Fortran 1V language and was run on the IBM 7094 computer at Imperial College. The program consists of two decks. The main deck reads in the film thickness data and evaluates the coefficients, and subroutine ITER performs the relaxation and prints out the pressures. Comment cards are inserted to assist understanding of the program. The symbols used, tie up with those in Chapter 9 as far as possible, Some of the less obvious symbols are:

| | | |
|---|---|---|
| DLOAD | = | Dimensionless load |
| DSPEED | = | Dimensionless speed |
| EDASH | = | E' |
| R | = | Relative contact radius |
| AOR | = | $\frac{a}{R}$ |
| $M, M_1, M_2$ | = | Extents of mesh in the I direction |
| $N, N_1, N_2$ | = | Extents of mesh in the J direction |
| TH | = | $\theta$ |
| DELTH | = | $\delta\theta$ |
| DELRF | = | $\delta$R (fine) |
| DELRC | = | $\delta$R (coarse) |
| JDELR | = | DELRC/DELRF |

The program is listed in Fig. 45, the conditions being approximately those of Fig. 20 I. The input shape is listed in Fig. 46 and the output pressures in Fig. 47. These are plotted in Fig. 48.

The input shape which is measured by the interference technique is very similar to the Grubin shape but differs most between X = -1 and X = -1.5, which is the most important region for pressure generation.

The computed pressure curve is probably fairly accurate in the inlet region, but the shape is so close to the Grubin shape (Fig. 48) that the true pressure distribution must be nearly Hertzian in the parallel part of the film. One reason for the computed pressures being too low is that the co-ordinate mesh is much too coarse to accurately represent the shape in the region of the horse-shoe constriction. If the constriction is not adequately represented, its effect in containing the fluid necessary to build up pressure in the contact, will not be taken into account.

```
      DIMENSION  H(50,13), B(50,13), C(50),    D(50,13), E(50,13)
      COMMON H,B,C,D,E
C       ASSEMBLE DATA
      DATA DLOAD, DSPEED, ALPHA, EDASH, R / 1.15E-06, 5.1E-11,
     2 1.83E-04, 17.4E+06, 1.27 /
      AOR = (1.5*DLOAD)**.33333333
      A = 6.*DSPEED/AOR*ALPHA*EDASH
      DATA M,M1,M2,N,N1,N2, DELTH, DELRF, JDELR/ 31,23,20,13,7,9,
     2 .2617994, .0625, 4/
      READ(5,201)  HC, ((H(I,J), J = 1,N,2), I = 1,20)
      READ(5,206)      ((H(I,J), J = 1,N2,2), I = 21,23)
      READ(5,207)      ((H(I,J), J = 1,N1,2), I = 24,31)
      READ(5,202)      ((H(I,J), J = 2,12,2), I = 1,20)
      READ(5,203)      ((H(I,J), J = 2, 8,2), I = 21,23)
      READ(5,204)      ((H(I,J), J = 2, 6,2), I = 24,31)
      WRITE(6,101)  HC,  ((H(I,J),J = 1,N), I = 1,M)
      HC = HC/R/AOR
      WRITE(6,103) DLOAD,DSPEED,ALPHA,EDASH,R,AOR,A,HC
      DO 22    I = 1,M
      DO 22    J = 1,N
   22 H(I,J) = H(I,J)/R/AOR
      DELRC = FLOAT(JDELR)*DELRF
C       EVALUATE C(I)
      DO 21    I = 1,M2
      FI = I
   21 C(I) = 1./(FI*FI*DELTH*DELTH)
      M2D = M2+1
      DO 23    I = M2D,M
      FI = M2/JDELR+I-M2
   23 C(I) = 1./(FI*FI*DELTH*DELTH)
C       EVALUATE COEFS FOR J = 1 AND J = N
      J = 1
      SI = -1.
      MK = M-1
    2 CONTINUE
      DELR = DELRF
      DO 30  I = 1,MK
      FI = I
      IF(I.NE.1)   GO TO 3
      HI = (H(2,J)-HC)/H(1,J)
      GO TO 7
    3 IF(I-M2)   4,5,6
    5 HI = (.1*H(I+1,J)+1.5*H(I,J)-1.6*H(I-1,J))/H(I,J)
      GO TO 7
    6 FI = M2/JDELR+I-M2
      DELR = DELRC
    4 HI= (H(I+1,J)-H(I-1,J))/H(I,J)
    7 E(I,J) = SI*A*DELR/2.*HI/(H(I,J)*H(I,J))
   30 B(I,J) = .5/FI+.75*HI
      J = N
      SI = 1.
      MK = M2
      IF(I.GT.M2)   GO TO 2
```

Fig. 45 Hydrodynamics program listing

```
C         EVALUATE COEFS FOR GENERAL POINTS
          MJ = 2
          MK = M2-1
          DELR = DELRF
          NK = N-1
    8     DO 20    I = MJ,MK
          FI = I
          IF(I.GT.M2)    FI = M2/JDELR+I-M2
          DO 20    J = 2,NK
          HJ = (H(I,J+1)-H(I,J-1))/H(I,J)
          HI = (H(I+1,J)-H(I-1,J))/H(I,J)
          TH = FLOAT(J-1)*DELTH
          E(I,J) = A*DELR/2.*(SIN(TH)/(FI*DELTH)*HJ-COS(TH)*HI)/(H(I,J)
       2 *H(I,J))
          D(I,J) = .75*C(I)*HJ
   20     B(I,J) = .5/FI+.75*HI
          IF(I-M1)    11,9,10
   11     MJ = M2+1
          MK = M1
          DELR = DELRC
          NK = N2-1
          GO TO 8
    9     MJ = M1+1
          MK = M-1
          NK = N1-1
          GO TO 8
C         EVALUATE COEFS FOR I = 2 AND I = M2
   10     I = 1
   16     FI = I
          DELR = DELRF
          NK = N-1
          DO 15   J = 2,NK
          IF(I.NE.1)    GO TO 13
          HI = (H(2,J)-HC)/H(I,J)
          GO TO 14
   13     HI = (.1*H(I+1,J)+1.5*H(I,J)-1.6*H(I-1,J))/H(I,J)
   14     HJ = (H(I,J+1)-H(I,J-1))/H(I,J)
          TH = FLOAT(J-1)*DELTH
          E(I,J) = A*DELR/2.*(SIN(TH)/(FI*DELTH)*HJ-COS(TH)*HI)/(H(I,J)
       2 *H(I,J))
          D(I,J) = .75*C(I)*HJ
   15     B(I,J) = .5/FI+.75*HI
          IF(I.NE.1)    GO TO 17
          I = M2
          GO TO 16
   17     CONTINUE
          WRITE(6,102)    ((B(I,J), J = 1,N), I = 1,M)
          WRITE(6,102)    (C(I),  I = 1,M)
          WRITE(6,102)    ((D(I,J), J = 1,N), I = 1,M)
          WRITE(6,102)    ((E(I,J), J = 1,N), I = 1,M)
          CALL ITER (ALPHA,M,M1,M2,N,N1,N2)
  201     FORMAT(E10.4/(7E10.4))
  206     FORMAT(5E10.4)
  207     FORMAT(4E10.4)
  202     FORMAT(6E10.4)
  203     FORMAT(4E10.4)
  204     FORMAT(3E10.4)
  101     FORMAT(5PF 7.2/(13F 7.2))
  102     FORMAT(1P7E17.4/ 3X, 6E17.4)
  103     FORMAT(1P8E16.6)
          STOP
          END
```

Fig. 45 (cont.)

```
      SUBROUTINE ITER   (ALPHA,M,M1,M2,N,N1,N2)
      DIMENSION  P(50,13), B(50,13), C(50),    D(50,13), E(50,13)
      COMMON P,B,C,D,E
      DATA OM/1.85/
C       INSERT INITIAL GUESS
      DO 10    I = 1,M2
      DO 10    J = 1,N
   10 P(I,J) =0.
      DO 11    J = 1,N
      DO 11    I = M2,M
   11 P(I,J) = 1.
      NUM = 0
      ICOUNT = 0
      NN = (N+1)/2
      MK = M-1
    1 CONTINUE
C       SET VALUE OF I
      DO 21    II = 1,MK
      I = M-II
C       EVALUATE P FOR J = 1
      PM1 = P(I-1,1)
      PP1 = P(I+1,1)
      IF(I.EQ.M2)    PP1 = 1.5*P(I,1)-.6*P(I-1,1)+.1*P(I+1,1)
      IF(I.EQ.1)    PM1 = (4.*P(1,NN)-P(2,NN))/3.
      V = (+E(I,1)+(1.-B(I,1))*PM1+(1.+B(I,1))*PP1+2.*C(I)*P(I,2))/
     2 (2.*(1.+C(I)))-P(I,1)
      P(I,1) = P(I,1)+OM*V
C       EVALUATE P FOR GENERAL POINTS
      NK = N1-1
      IF(I-M2)    5,7,7
    5 NK = N-1
      GO TO 8
    7 IF(I.LT.M1)    NK = N2-1
    8 DO 20    J = 2,NK
      PM = P(I-1,J)
      PP = P(I+1,J)
      IF(I.EQ.1)     PM = (4.*P(1,NN)-P(2,NN))/3.
      IF(I.EQ.M2)    PP  = 1.5*P(I,J)-.6*P(I-1,J)+.1*P(I+1,J)
      V = (+E(I,J)+(1.-B(I,J))*PM +(1.+B(I,J))*PP+(C(I)-D(I,J))
     2  *P(I,J-1)+(C(I)+D(I,J))*P(I,J+1))/(2.*(1.+C(I)))-P(I,J)
      P(I,J) = P(I,J)+OM*V
C       END BOUNDARY AND ERROR TRAP
      IF(P(I,J).GT.1.)    P(I,J) = 1.
      IF(P(I,J).LT.0.)    P(I,J) = 1.E-8
   20 CONTINUE
      IF(NK.LT.N-1)    GO TO 21
C       EVALUATE P FOR J = N
      PMN = P(I-1,N)
```

Fig. 45 (cont.)

```
      PPN = P(I+1,N)
      IF(I.EQ.1)    PMN = (4.*P(1,NN)-P(2,NN))/3.
      V = (+E(I,N)+(1.-B(I,N))*PMN+(1.+B(I,N))*PPN+2.*C(I)*P(I,N-1))/
     2 (2.*(1.+C(I)))-P(I,N)
      P(I,N) = P(I,N)+OM*V
      IF(P(I,N).GT.1.)    P(I,N) = 1.
      IF(P(I,N).LT.0.)    P(I,N) = 1.E-8
   21 CONTINUE
C       ITERATION COUNT
      NUM = NUM+1
      IF(NUM.EQ.50 )  GO TO 12
      GO TO 13
   12 WRITE(6,103)  PMN, ((P(I,J), J = 1,N), I = 1,M)
      ICOUNT = ICOUNT+NUM
      IF(ICOUNT.GE.400)    GO TO 24
      NUM = 0
   13 CONTINUE
C       TEST CONVERGENCE
      TST = (PMN-PT)*(PMN-PT)
      PT = PMN
      IF(TST.GT.1.E-17)    GO TO 1
      ICOUNT = ICOUNT+NUM
   24 WRITE(6,105) PMN,ICOUNT, ((P(I,J), J = 1,N), I = 1,M)
C       CONVERT TO REAL PRESSURE
      PMN = ALOG(1./(    PMN))/ALPHA
      DO 22    J = 1,N
      DO 22    I = 1,M
   22 P(I,J) = ALOG(1./(    P(I,J)))/ALPHA
      WRITE(6,104)  PMN, ((P(I,J), J = 1,N), I = 1,M)
  103 FORMAT(F10.7/(13F10.7))
  104 FORMAT(F 8.0/(13F 8.0))
  105 FORMAT(F10.7, I8/(13F10.7))
      RETURN
      END
```

Fig. 45 (cont.)

| R \ θ | 0 | | 30° | | 60° | | 90° | | 120° | | 150° | | 180° |
|---|---|---|---|---|---|---|---|---|---|---|---|---|---|
| 0 | 3.80 | | | | | | | | | | | | |
| | 3.80 | 3.80 | 3.80 | 3.80 | 3.80 | 3.80 | 3.80 | 3.80 | 3.80 | 3.80 | 3.80 | 3.80 | 3.80 |
| | 3.80 | 3.80 | 3.80 | 3.80 | 3.80 | 3.80 | 3.80 | 3.80 | 3.80 | 3.80 | 3.80 | 3.80 | 3.80 |
| | 3.80 | 3.80 | 3.80 | 3.80 | 3.80 | 3.80 | 3.80 | 3.80 | 3.80 | 3.80 | 3.80 | 3.80 | 3.80 |
| .25 | 3.80 | 3.80 | 3.80 | 3.80 | 3.80 | 3.80 | 3.80 | 3.80 | 3.80 | 3.80 | 3.80 | 3.80 | 3.80 |
| | 3.80 | 3.80 | 3.80 | 3.80 | 3.80 | 3.80 | 3.80 | 3.80 | 3.80 | 3.80 | 3.80 | 3.80 | 3.80 |
| | 3.80 | 3.80 | 3.80 | 3.80 | 3.80 | 3.80 | 3.80 | 3.80 | 3.80 | 3.80 | 3.80 | 3.80 | 3.80 |
| | 3.80 | 3.80 | 3.80 | 3.80 | 3.80 | 3.80 | 3.80 | 3.80 | 3.80 | 3.80 | 3.80 | 3.80 | 3.80 |
| .5 | 3.80 | 3.80 | 3.80 | 3.80 | 3.80 | 3.80 | 3.80 | 3.80 | 3.80 | 3.80 | 3.80 | 3.80 | 3.80 |
| | 3.80 | 3.80 | 3.80 | 3.80 | 3.80 | 3.80 | 3.75 | 3.80 | 3.80 | 3.80 | 3.80 | 3.80 | 3.80 |
| | 3.80 | 3.80 | 3.80 | 3.80 | 3.75 | 3.75 | 3.65 | 3.75 | 3.80 | 3.80 | 3.80 | 3.80 | 3.80 |
| | 3.80 | 3.80 | 3.80 | 3.80 | 3.70 | 3.55 | 3.45 | 3.55 | 3.75 | 3.80 | 3.80 | 3.80 | 3.80 |
| .75 | 3.80 | 3.80 | 3.80 | 3.80 | 3.65 | 3.30 | 3.10 | 3.10 | 3.55 | 3.75 | 3.75 | 3.75 | 3.75 |
| | 3.80 | 3.80 | 3.80 | 3.80 | 3.55 | 3.00 | 2.60 | 2.50 | 3.05 | 3.50 | 3.65 | 3.65 | 3.70 |
| | 3.85 | 3.82 | 3.80 | 3.80 | 3.40 | 2.60 | 2.30 | 1.90 | 2.20 | 2.60 | 3.30 | 3.40 | 3.50 |
| | 4.05 | 4.02 | 3.90 | 3.90 | 3.60 | 3.00 | 2.70 | 2.50 | 2.20 | 2.50 | 2.70 | 2.70 | 2.90 |
| 1.0 | 4.50 | 4.42 | 4.25 | 4.15 | 4.00 | 3.55 | 3.20 | 3.10 | 2.85 | 3.10 | 3.20 | 3.40 | 3.50 |
| | 5.00 | 4.92 | 4.85 | 4.65 | 4.50 | 4.10 | 3.70 | 3.70 | 3.50 | 3.70 | 3.90 | 4.20 | 4.40 |
| | 5.70 | 5.60 | 5.55 | 5.30 | 5.30 | 4.80 | 4.50 | 4.50 | 4.40 | 4.60 | 5.00 | 5.20 | 5.40 |
| | 6.40 | 6.40 | 6.40 | 6.20 | 6.00 | 5.80 | 5.50 | 5.60 | 5.70 | 5.65 | 6.00 | 6.20 | 6.30 |
| 1.25 | 7.30 | 7.30 | 7.30 | 7.10 | 6.90 | 6.80 | 6.55 | 6.60 | 6.60 | 6.85 | 6.90 | 7.10 | 7.20 |
| 1.5 | 11.60 | 11.60 | 11.60 | 11.60 | 11.50 | 11.50 | 11.40 | 11.40 | 11.50 | -0.00 | -0.00 | -0.00 | -0.00 |
| | 17.60 | 17.60 | 17.60 | 17.60 | 17.60 | 17.60 | 17.60 | 17.60 | 17.60 | -0.00 | -0.00 | -0.00 | -0.00 |
| 2.0 | 25.80 | 25.80 | 25.80 | 25.80 | 25.80 | 25.80 | 25.80 | 25.80 | 25.80 | -0.00 | -0.00 | -0.00 | -0.00 |
| | 35.20 | 35.20 | 35.20 | 35.20 | 35.20 | 35.20 | 35.20 | -0.00 | -0.00 | -0.00 | -0.00 | -0.00 | -0.00 |
| | 45.60 | 45.60 | 45.60 | 45.60 | 45.60 | 45.60 | 45.60 | -0.00 | -0.00 | -0.00 | -0.00 | -0.00 | -0.00 |
| | 57.40 | 57.40 | 57.40 | 57.40 | 57.40 | 57.40 | 57.40 | -0.00 | -0.00 | -0.00 | -0.00 | -0.00 | -0.00 |
| 3.0 | 70.30 | 70.30 | 70.30 | 70.30 | 70.30 | 70.30 | 70.30 | -0.00 | -0.00 | -0.00 | -0.00 | -0.00 | -0.00 |
| | 84.20 | 84.20 | 84.20 | 84.20 | 84.20 | 84.20 | 84.20 | -0.00 | -0.00 | -0.00 | -0.00 | -0.00 | -0.00 |
| | 99.40 | 99.40 | 99.40 | 99.40 | 99.40 | 99.40 | 99.40 | -0.00 | -0.00 | -0.00 | -0.00 | -0.00 | -0.00 |
| | 112.00 | 112.00 | 112.00 | 112.00 | 112.00 | 112.00 | 112.00 | -0.00 | -0.00 | -0.00 | -0.00 | -0.00 | -0.00 |
| 4.0 | 131.00 | 131.00 | 131.00 | 131.00 | 131.00 | 131.00 | 131.00 | -0.00 | -0.00 | -0.00 | -0.00 | -0.00 | -0.00 |

Fig. 46 Input film shape (h x $10^5$cm) for DLOAD = 1.15 x $10^{-6}$ and DSPEED = 5.1 x $10^{-11}$

| R \ θ | 0 | | 30° | | 60° | | 90° | | 120° | | 150° | | 180° |
|---|---|---|---|---|---|---|---|---|---|---|---|---|---|
| 0 | 7983. | | | | | | | | | | | | |
| | 8230. | 8221. | 8195. | 8155. | 8103. | 8044. | 7982. | 7921. | 7865. | 7817. | 7780. | 7758. | 7750. |
| | 8492. | 8472. | 8416. | 8329. | 8221. | 8101. | 7978. | 7859. | 7751. | 7658. | 7587. | 7542. | 7526. |
| | 8775. | 8741. | 8647. | 8506. | 8336. | 8153. | 7971. | 7799. | 7644. | 7509. | 7402. | 7332. | 7308. |
| .25 | 9084. | 9032. | 8890. | 8684. | 8445. | 8197. | 7959. | 7741. | 7545. | 7370. | 7225. | 7127. | 7093. |
| | 9425. | 9349. | 9145. | 8863. | 8547. | 8232. | 7941. | 7685. | 7458. | 7245. | 7057. | 6925. | 6876. |
| | 9806. | 9697. | 9413. | 9041. | 8640. | 8258. | 7916. | 7631. | 7384. | 7136. | 6896. | 6722. | 6656. |
| | 10240. | 10083. | 9693. | 9219. | 8724. | 8273. | 7880. | 7575. | 7328. | 7046. | 6743. | 6518. | 6428. |
| .5 | 10742. | 10515. | 9983. | 9396. | 8797. | 8280. | 7830. | 7516. | 7292. | 6979. | 6595. | 6313. | 6191. |
| | 11336. | 11007. | 10277. | 9573. | 8858. | 8280. | 7764. | 7447. | 7284. | 6941. | 6452. | 6106. | 5941. |
| | 12060. | 11573. | 10566. | 9756. | 8975. | 8257. | 7672. | 7378. | 7309. | 6938. | 6308. | 5900. | 5673. |
| | 12974. | 12242. | 10835. | 9890. | 9197. | 8300. | 7543. | 7259. | 7358. | 6978. | 6157. | 5699. | 5382. |
| .75 | 14188. | 13055. | 11068. | 9912. | 9358. | 8450. | 7345. | 6880. | 7353. | 7031. | 5916. | 5430. | 4986. |
| | 15936. | 14086. | 11252. | 9768. | 9322. | 8521. | 6724. | 5695. | 6927. | 6816. | 5426. | 4959. | 4418. |
| | 17996. | 15286. | 11386. | 9398. | 8997. | 8120. | 4955. | 2744. | 4532. | 4820. | 4277. | 4008. | 3496. |
| | 17157. | 14797. | 11087. | 8583. | 7652. | 6068. | 2863. | 644. | 705. | 946. | 1755. | 1567. | 1426. |
| 1.0 | 12854. | 11800. | 9607. | 7334. | 5916. | 4200. | 1725. | 122. | 0. | 0. | 0. | 0. | 0. |
| | 9366. | 8841. | 7505. | 5883. | 4449. | 2908. | 1036. | 0. | 0. | 0. | 0. | 0. | 0. |
| | 6938. | 6615. | 5717. | 4563. | 3321. | 2008. | 619. | 0. | 0. | 0. | 0. | 0. | 0. |
| | 5259. | 5020. | 4375. | 3519. | 2499. | 1397. | 379. | 0. | 0. | 0. | 0. | 0. | 0. |
| 1.25 | 4058. | 3877. | 3394. | 2733. | 1891. | 988. | 233. | 0. | 0. | 0. | 0. | 0. | 0. |
| 1.5 | 1650. | 1587. | 1407. | 1133. | 791. | 422. | 100. | 0. | 0. | 0. | 0. | 0. | 0. |
| | 811. | 782. | 697. | 564. | 396. | 210. | 36. | 0. | 0. | 0. | 0. | 0. | 0. |
| 2.0 | 451. | 436. | 389. | 316. | 223. | 116. | 0. | 0. | 0. | 0. | 0. | 0. | 0. |
| | 274. | 264. | 236. | 193. | 136. | 70. | 0. | 0. | 0. | 0. | 0. | 0. | 0. |
| | 174. | 168. | 150. | 122. | 86. | 45. | 0. | 0. | 0. | 0. | 0. | 0. | 0. |
| | 112. | 108. | 97. | 79. | 56. | 29. | 0. | 0. | 0. | 0. | 0. | 0. | 0. |
| 3.0 | 72. | 70. | 63. | 51. | 36. | 19. | 0. | 0. | 0. | 0. | 0. | 0. | 0. |
| | 45. | 43. | 39. | 32. | 22. | 12. | 0. | 0. | 0. | 0. | 0. | 0. | 0. |
| | 26. | 25. | 22. | 18. | 13. | 7. | 0. | 0. | 0. | 0. | 0. | 0. | 0. |
| | 11. | 11. | 10. | 8. | 6. | 3. | 0. | 0. | 0. | 0. | 0. | 0. | 0. |
| 4.0 | 0. | 0. | 0. | 0. | 0. | 0. | 0. | 0. | 0. | 0. | 0. | 0. | 0. |

Fig. 47 Computed pressure (psi) for DLOAD = $1.15 \times 10^{-6}$ and DSPEED = $5.1 \times 10^{-11}$

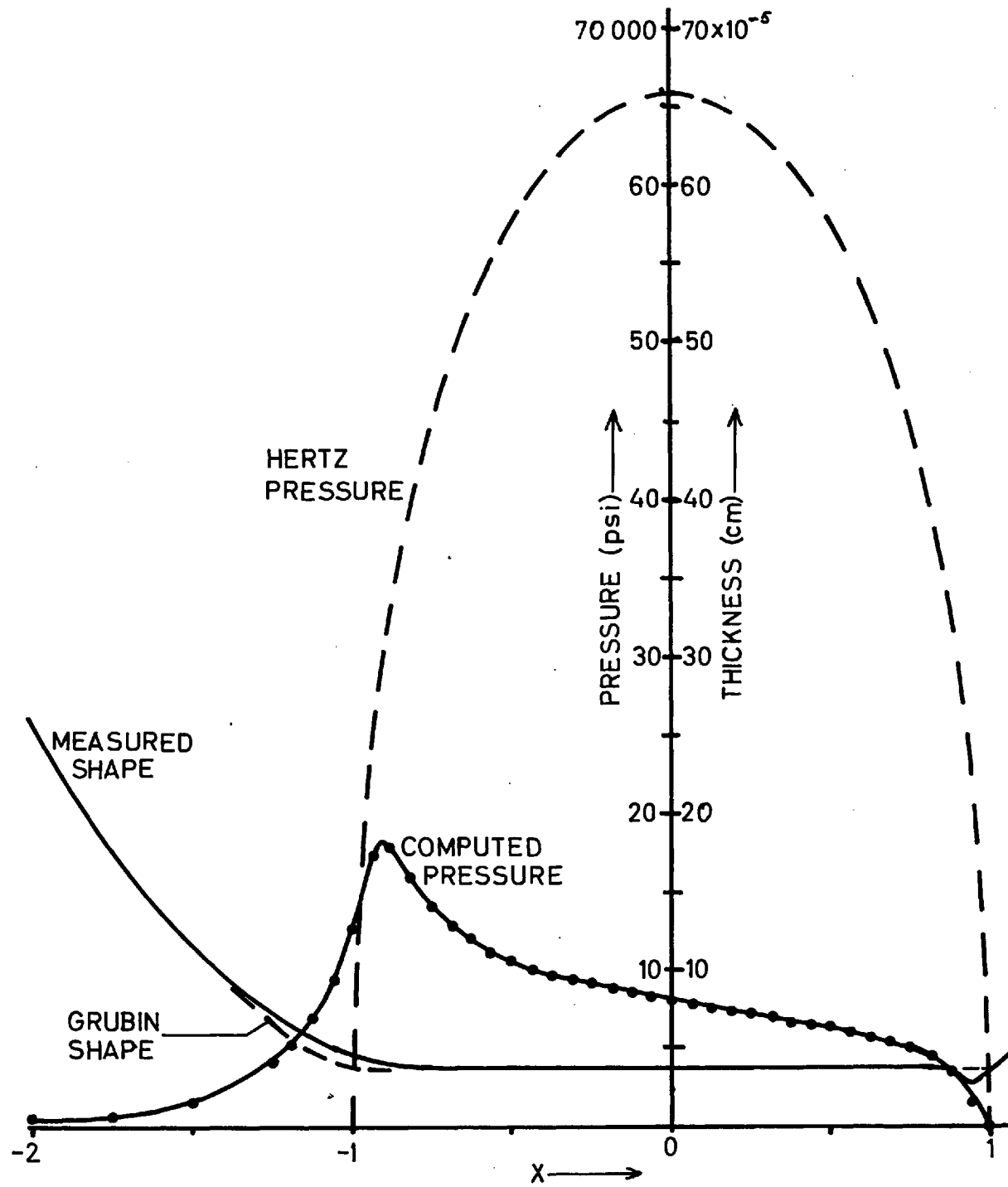



Fig. 48 Shape and pressure profiles

References

1. C.G.Hingley, PhD Thesis, Imperial College London 1964

2. S.Way, "Pitting due to rolling contact", Trans ASME 1935, 57, A49

3. P.H.Dawson, "The pitting of lubricated gear teeth and rollers", Power Transmission London 1961, 30, 208 - 217 and 286 - 290

4. G.Niemann, "Walzenfestigkeit und Grubehenbildung von Zahnrad und Walzlagerwerkstoffen", Zeit V.D.I. 1943, 87, 33/34, 521 - 3

5. A.Cameron, "Surface failure in gears", J.Inst.Pet. 1954, 40, 191 - 202

6. D.Scott, "Study of the effect of lubricant on pitting failure of balls", Proc.Lub. and Wear Conf. I.Mech.E. 1957

7. R.Beeching and W.Nicholls, "A theoretical discussion of pitting failures in gears", Proc.I.Mech.E. 1948, 158, 317

8. M.Ullricht, "Zur Frage der Grübchenbildung bei Zahnradern", Zeit. V.D.I. 1934, 28, No 2

9. P.H.Dawson, "Effect of metallic contact on the pitting of lubricated rolling surfaces", J.Mech.Eng.Sci. 1962, 4, 16

10. D.Dowson, G.R.Higginson and A.V.Whitaker, "Stress distribution in lubricated rolling contacts", I.Mech.E. Fatigue in Rolling Contact 1964 Paper 6

11. D.Dowson and G.R.Higginson, "Elasto-hydrodynamic lubrication", Pergamon Press, Oxford 1966

12. A.W.Crook, "Simulated gear tooth contact: Some experiments upon their lubrication and sub-surface deformations", Proc.I.Mech.E. 1957, 171, 187

13. G.M.Hamilton, "Plastic flow in rollers loaded above the yield point", Proc.I.Mech.E. 1963, 177, 667

14. J.E.Merwin and K.L.Johnson, "An analysis of plastic deformation in rolling contact", Proc.I.Mech.E. 1963, 177, 676

15. K.L.Johnson and J.A.Jefferis, "Plastic flow and residual stress in rolling and sliding contact", I.Mech.E. Fatigue and Rolling Contact 1964 Paper 5

16. C.C.Moore and P.Lewis, "Current development problems in high temperature aircraft roller bearings", Proc.Lub. and Wear Conf. I.Mech.E. 1957, Paper 34

17. J.B.Martin and A.Cameron, "Effect of oil on the pitting of rollers", J.Mech.Eng.Sci. 1961, 3, 148

18. H.V.Cordriano, E.P.Cochrane and R.J.Wolfe, "Effect of combustion-resistant hydraulic fluids on ball-bearing fatigue life", Trans. ASME 1956, 78, 989

19. T.L.Carter, "Effect of lubricant viscosity on rolling contact fatigue life", NACA, 1957, Tech.Note 401

20. D.Scott and J.Blackwell, "Study of the effects of elevated-temperature lubricants on materials for rolling elements", Lub. and Wear Conf. I.Mech.E. 1967, Paper 12

21. S.Hashimoto, "On the pitting of power transmitting spur gears", Bull. JSME 1963, 6, 148 - 159

22. A.N.Grubin, "Contact stresses in toothed gears and worm gears", Cent. Sci.Res.Inst. for Tech. and Mech. Eng. (Moscow)(1949), Book no. 30. DSIR Trans. no. 337

23. D.Dowson and G.R.Higginson, "A numerical solution to the elastohydrodynamic problem", J.Mech.Eng.Sci. 1959, 1, 6

24. D.Dowson and G.R.Higginson, "The effect of material properties on the lubrication of elastic rollers", J.Mech.Eng.Sci. 1960, 2, 188

25. D.Dowson and G.R.Higginson, "New roller-bearing lubrication formula", Engineering (London), 1961, 192, 158

26. D.Dowson, G.R.Higginson and A.V.Whitaker, "Elastohydrodynamic lubrication - a survey of isothermal solutions", J.Mech.Eng. Sci. 1962, 4, No 2, 121

27. D.Dowson and G.R.Higginson, "A theory of involute gear lubrication", Inst. Pet. Gear Lubrication Symposium 1964

28. D.Dowson and A.V.Whitaker, "The isothermal lubrication of cylinders", Trans. ASLE, 1965, 8, 224

29. D.Dowson and A.V.Whitaker, "A numerical procedure for the solution of the elastohydrodynamic problem of rolling and sliding contacts lubricated by a Newtonian fluid", I.Mech.E. 1965, Leeds EHL Symp. Paper 4

30. G.D.Archard, F.C.Gair and W.Hirst, "The elastohydrodynamic lubrication of rollers", Proc.Roy.Soc.A. 1961, 262, 51

31. H.S.Cheng and B.Sternlicht, "A numerical solution for the pressure temperature and film thickness between two infinitely long, lubricated rolling and sliding cylinders, under heavy loads", J.Basic.Eng. 1965, 87, 695 - 707

32. H.S.Cheng and F.K.Orcutt, "A correlation between the theoretical and experimental results on the elastohydrodynamic lubrication of rolling and sliding contacts", I.Mech.E. 1965, Leeds EHL Symp. Paper 13.

33. R.Gohar and A.Cameron, "Theoretical and experimental studies of the oil film in lubricated point contact", Proc.Roy.Soc.A. 1966, 291, 520

34. J.F.Archard and E.W.Cowking, "Elastohydrodynamic lubrication of point contacts", I.Mech.E. 1965, Leeds EHL Symp., Paper 3

35. A.W.Crook, "The lubrication of rollers", Phil.Trans. (A) 1958, 250, 387

36. A.W.Crook, "The lubrication of rollers II, Film thickness with relation to viscosity and speed", Phil.Trans. (A) 1962, 254, 223

37. A.W.Crook, "The lubrication of rollers III, A theoretical discussion of friction and the temperatures in the oil film", Phil.Trans. (A) 1962, 254, 237

38. A.W.Crook, "The lubrication of rollers IV, Measurements of friction and effective viscosity", Phil.Trans. (A), 1962, 255, 281

39. A.W.Crook, "Elasto-hydrodynamic lubrication of rollers", Nature 1961, 190, 1182

40. A.W.Crook, "Developments in elasto-hydrodynamic lubrication", J.Inst.Pet. 1963, 49, No 478, 295

41. A.Dyson, H.Naylor and A.R.Wilson, "The measurement of film thickness in Elastohydrodynamic contacts", I.Mech.E. 1965 Leeds EHL Symp.

42. A.Dyson and A.R.Wilson, "Film thickness in elastohydrodynamic lubrication by silicone fluids", I.Mech.E. 1966 Lub. and Wear Conv. Paper 3

43. L.B.Sibley and F.K.Orcutt, "Elasto-hydrodynamic lubrication of rolling contact surfaces", Trans. ASLE, 1961, 4, 234

44. J.W.Kannel, J.C.Bell and C.M.Allen, "Methods for determining pressure distribution in lubricated rolling contact", Trans. ASLE 1965, 8, 250

45. J.F.Archard and M.T.Kirk, "Lubrication at point contacts", Proc.Roy.Soc. A. 1961, 261, 532

46. J.F.Archard and M.T.Kirk, "Influence of elastic modulus on the lubrication of point contacts", I.Mech.E. 1963 Lub. and Wear Conv. Paper 181

47. J.F.Archard and M.T.Kirk, "Film thicknesses for a range of lubricants under severe stress", J.Mech.Eng.Sci. 1964, 6, 101

48. M.T.Kirk, "Hydrodynamic lubrication of perspex", Nature, 1962, 194, 965

49. R.Gohar and A.Cameron, "Optical measurement of oil film thickness under elastohydrodynamic lubrication", Nature, 1963, 200, 458

50. R.Gohar and A.Cameron, "The mapping of elastohydrodynamic contacts", ASLE/ASME Lub.Conf. Minneapolis 1966, Preprint 66LC-21

51. C.A.Foord, W.C.Hammann and A.Cameron, "Evaluation of lubricants using optical elastohydrodynamics", ASLE/ASME Lub.Conf.Chicago 1967. ASLE Paper 67LC-12

52. G.Niemann and F.Gartner, "Distribution of hydrodynamic pressure on counterformel line contacts", Trans. ASLE, 1965, 8, 235

53. J.W.Kannel, "Measurement of pressures in rolling contact", I.Mech.E.1965 Leeds EHL Symp.

54. J.W.Kannel, J.A.Walowit, J.C.Bell and C.M.Allen, "The determination of stresses in rolling contact elements", ASLE/ASME Conf. Oct.1966, Paper 66-Lub-16

55. ASME, "Viscosity and density of over 40 fluids at pressures to 150,000 psi and temperatures to 425 F", Research Committee on Lubrication, ASME 1953

56. P.S.Y.Chu and A.Cameron, "Pressure viscosity characteristics of lubricating oils", J.Inst.Pet. 1962, 48, 147-155

57. P.S.Y.Chu and A.Cameron, "Compressibility and thermal expansion of oils", J.Inst.Pet. 1963, 49, 140-145

58. C.J.Roelands, "Correlation aspects of the viscosity-temperature-pressure relationship of lubricating oils", Technological University of Delft, 1966, Thesis

59. G.P.Fresco, "Measurement and prediction of viscosity-pressure characteristics of liquids", MSc Thesis, Penn.State 1966

60. G.D.Galvin, H.Naylor and A.R.Wilson, "The effect of pressure and temperature on some properties of importance in elastohydrodynamic lubrication", I.Mech.E. 1964 Proc.Lub. and Wear Conv.

61. A.J.Barlow and J.Lamb, "The visco-elastic behaviour of lubricating oils and cyclic shearing stress", Proc.Roy.Soc.A. 1959, 253, 52

62. J.G.Oldroyd, "Non-Newtonian effects in steady motion of some idealized elasto-viscous liquids", Proc.Roy.Soc.A. 1958, 245, 278

63. A.A.Milne, "A theory of rheodynamic lubrication for a maxwell liquid", I.Mech.E. 1957 Proc.Conf.Lub. and Wear

64. R.A.Burton, "An analytical investigation of viscoelastic effects in the lubrication of rolling contact", Trans. ASLE 1960, 3, 1

65. R.I.Tanner, "Full film lubrication theory for a Maxwell liquid", Int.J.Mech.Sci. 1960, 1, 206

66. R.I.Tanner, "Some illustrative problems in the flow of viscoelastic non-Newtonian lubricants", Trans ASLE 1965, 8, 179

67. A.Dyson, "Flow properties of mineral oils in elastohydrodynamic lubrication", Phil.Trans.A. 1965, 258, 529

68. W.Philippoff, "Viscosity measurements on polymer modified oils", Trans. ASLE 1958, 1, 82

69. H.H.Horowitz and F.F.Steidler, "The calculated journal bearing performance of polymer thickened lubricants", Trans. ASLE 1960, 3, 124

70. G.M.Hamilton and W.G.Robertson, "Lubrication of rollers with oils containing polymers", I.Mech.E.Lub.and Wear Conv. 1967, Paper 3

71. T.S.Chow and E.Saibel, "The elastohydrodynamic problem with a viscoelastic fluid", ASLE/ASME Lub. Conf. Chicago 1967 ASME Paper 67 Lub - 23

72. A.Cameron, "Principles of lubrication", Longmans, London 1966

73. M.D.Hersey, "Theory and research in lubrication", Wiley, New York 1966

74. A.Bondi, "Physical chemistry of lubricating oils", Reinhold 1951

75. G.Niemann, "Maschinenelemente" Vol.1. Section 13.4, p 212. (Springer, Berlin 1955)

76. I.O.MacConchie and A.Cameron, "The measurement of oil film thickness in gear teeth", Trans, ASME. J.B.Eng.D. 1960, 82, 29

77. S.Tolansky, "An introduction to interferometry", Longmans, London 1962

78. S.Glasstone, "Physical Chemistry", Macmillan, London 1956

79. R.S.Fein and C.A.Foord, Discussion and authors closure to reference 51

80. R.Gohar, PhD Thesis, Imperial College London 1965

81. N.S.Grassam and J.W.Powell, "Gas lubricated bearings", Butterworth, London.

82. D.Dowson and D.A.Jones, "Lubricant entrapment between approaching elastic solids" Nature 1967,214,947

83. John Zuk, T.N.Strom, L.P.Ludwig, R.L.Johnson, "Convective inertia and gass ingestion effects on flow regimes of the viscoseal - theory and experiment", NASA TMX-52283, 1967. To be published in Trans. ASLE

84. National Physical Laboratory, "Modern computing methods", HMSO London 1961

85. J.Prescott, "Applied Elasticity", Longmans, 1925, Reprinted: Dover, New York, 1946

86. S.H.Crandall, "Engineering Analysis", McGraw-Hill, New York, 1956

87. F.J.Westlake and A.Cameron "Fluid film interferometry in lubrication studies", Nature 1967, 214, 633

88. A.Cameron, "Hydrodynamic theory in gear lubrication", J.Inst.Pet. 1952,38,614

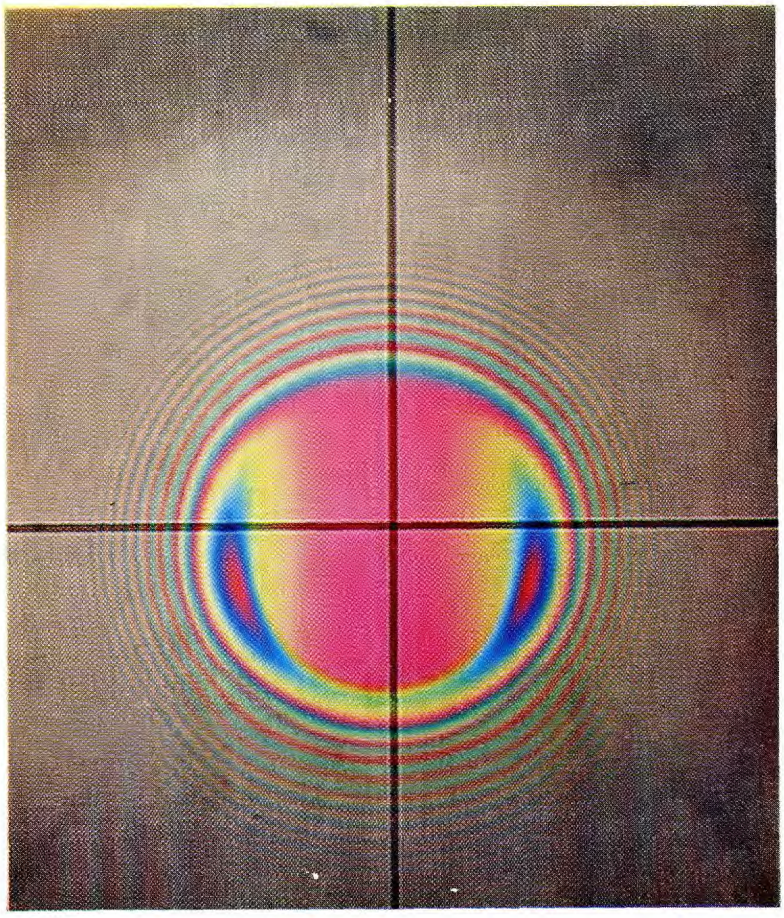
89. R.J.Parker, E.N.Bamberger, E.V.Zaretsky, "Evaluation of lubricants for high temperature ball bearing applications", ASME Preprint 67-Lub-21, present at the ASLE/ASME Lub. Conf. Chicago 1967

90. E.E.Klaus, R.E.Hersh and L.D.Dromgold, "Super refining of paraffinic resins", Am. Chem. Soc., Pet. Chem. Div., Chicago Conf. 1967

91. S.Wawzonek, H.J.Bluhm, B.Studnicka, R.E.Kallis and E.J.McKenna, "Coupling reactions of 1-Chloro-5,5,7,7-tetramethyloctene-2", J.Org.Chem., 30, 3029 (1965)

92. L.R.Stark and K.L.McHugh, "Properties of a new class of polyaromatics for use as high temperature lubricants and functional fluids", ASLE Trans., 9, 13 (1966)

93. W.H.Gumprecht, "PR-143 A new class of high-temperature fluids", ASLE Trans., 9, 24 (1966)



Interference colours at the contact of a lubricated steel ball rolling on a glass plate